

**Josephson Junction Devices: Model Quantum Mechanical Systems and
Medical Applications**

by

Josephine Chen

A.B. (Harvard University) 1997
M.A. (University of California, Berkeley) 2000

A dissertation submitted in partial satisfaction of the
requirements for the degree of
Doctor of Philosophy

in

Physics

in the

GRADUATE DIVISION
of the
UNIVERSITY OF CALIFORNIA, BERKELEY

Committee in charge:
Professor John Clarke, Chair
Professor Michael F. Crommie
Professor Theodore Van Duzer

Spring 2003

The dissertation of Josephine Chen is approved:

Chair	Date
-------	------

	Date
--	------

	Date
--	------

University of California, Berkeley

Spring 2003

**Josephson Junction Devices: Model Quantum Mechanical Systems and
Medical Applications**

Copyright 2003

by

Josephine Chen

Abstract

Josephson Junction Devices: Model Quantum Mechanical Systems and Medical
Applications

by

Josephine Chen

Doctor of Philosophy in Physics

University of California, Berkeley

Professor John Clarke, Chair

In this dissertation, three experiments using Josephson junction devices are described. In Part I, the effect of dissipation on tunneling between charge states in a superconducting single-electron transistor (sSET) was studied. The sSET was fabricated on top of a semiconductor heterostructure with a two-dimensional electron gas (2DEG) imbedded beneath the surface. The 2DEG acted as a dissipative ground plane. The sheet resistance of the 2DEG could be varied *in situ* by applying a large voltage to a gate on the back of the substrate. The zero-bias conductance of the sSET was observed to increase with increasing temperature and 2DEG resistance. Some qualitative but not quantitative agreement was found with theoretical calculations of the functional dependence of the conductance on temperature and 2DEG resistance .

Part II describes a series of experiments performed on magnesium diboride point-

contact junctions. The pressure between the MgB_2 tip and base pieces could be adjusted to form junctions with different characteristics. With light pressure applied between the two pieces, quasiparticle tunneling in superconductor-insulator-superconductor junctions was measured. From these data, a superconducting gap of approximately 2 meV and a critical temperature of 29 K were estimated. Increasing the pressure between the MgB_2 pieces formed junctions with superconductor-normal metal-superconductor characteristics. We used these junctions to form MgB_2 superconducting quantum interference devices (SQUIDs). Noise levels as low as 35 fT/Hz^{1/2} and 4 $\mu\Phi_0$ /Hz^{1/2} at 1 kHz were measured.

In Part III, we used a SQUID-based instrument to acquire magnetocardiograms (MCG), the magnetic field signal measured from the human heart. We measured 51 healthy volunteers and 11 cardiac patients both at rest and after treadmill exercise. We found age and sex related differences in the MCG of the healthy volunteers that suggest that these factors should be considered when evaluating the MCG for disease. We also defined a spatio-temporal MCG parameter, the repolarization stabilization interval, which successfully discriminated our patients from our healthy controls.

Professor John Clarke
Dissertation Committee Chair

Contents

List of Figures	iv
List of Tables	vi
1 Preface	1
1.1 Superconductivity	1
1.2 The Josephson junction	2
1.3 Josephson junction devices	6
 I The Effect of Dissipation on a Superconducting Single-Electron Transistor	 10
2 Introduction	11
2.1 Dissipation in macroscopic quantum mechanical systems	11
2.2 The superconducting single-electron transistor and Coulomb blockade . . .	13
2.3 The sSET with dissipation	15
3 Experimental Methods	19
3.1 Sample preparation	19
3.1.1 GaAs/AlGaAs heterostructure substrate	19
3.1.2 Microfabrication of the sSET	21
3.2 Sample characterization	25
3.2.1 The sSET	25
3.2.2 The dissipative ground plane	27
3.2.3 The leads	27
3.2.4 The effective impedance across the junction	30
3.3 Measurement techniques	32
4 Experimental Results	35
4.1 Qualitative observations	35
4.2 Comparison with theoretical calculations	39

5	Conclusion	48
II	MgB₂ Point-Contact Junctions and SQUIDs	50
6	Introduction	51
7	Experimental Methods	53
8	Estimating the Superconducting Gap in MgB₂ using SIS Tunnel Junctions	55
8.1	Quasiparticle tunneling	55
8.2	Suppression of the Josephson supercurrent	57
8.3	Data and results	58
9	MgB₂ SNS Junctions and SQUIDs	61
9.1	SNS junctions	61
9.2	RF-driven SNS junctions	63
9.3	MgB ₂ SQUIDs	65
9.4	Noise measurements	68
10	Conclusion	73
III	SQUID-based Magnetocardiography for the Detection of Heart Disease	75
11	Introduction	76
11.1	Biological and medical applications of SQUIDs	76
11.2	Bioelectromagnetism and the heart	77
11.3	Comparing magnetocardiography and electrocardiography	80
11.4	Magnetocardiography for the detection of ischemia	81
12	Experimental Methods	84
12.1	MCG system and measurement	84
12.2	Subjects	87
12.2.1	Normal subjects	87
12.2.2	Ischemic patients	87
12.3	Study protocol	88
13	Data Analysis and Results	91
13.1	Signal processing	91
13.2	MCG data analysis	93
13.2.1	MCG contour map parameters	93
13.2.2	MCG waveform morphology parameters	97
13.3	Results	99

13.3.1	Variation of MCG in healthy subjects	99
13.3.2	Differences between ischemic patients and older healthy controls . .	101
13.3.3	Comparison of different MCG parameters	107
14	Discussion and Conclusion	111
14.1	Discussion	111
14.2	Conclusion	114
15	Concluding Remarks	116
A	Transport Calculation for the sSET	120
	Bibliography	124

List of Figures

1.1	Resistively and capacitively shunted junction model	5
1.2	Ideal current-voltage behavior of an underdamped Josephson junction . . .	6
2.1	Circuit diagram of ideal sSET without dissipation	13
2.2	Gate voltage dependence of zero-bias conductance	16
3.1	GaAs/AlGaAs heterostructure	20
3.2	Shadow mask fabrication	22
3.3	Two-angle shadow evaporation of the sSET	23
3.4	Scanning electron microscopy image of an sSET	24
3.5	Diagram of the sSET coupled to a 2DEG	26
3.6	Van der Pauw measurement configuration	28
3.7	2DEG resistance as a function of the back-gate voltage	28
3.8	Diagram of the leads to the sSET	29
3.9	Equivalent impedance across one of the junctions in the sSET	31
3.10	Measurement configuration for the sSET	34
4.1	Current-voltage characteristic of the sSET	36
4.2	Zero-bias conductance as a function of gate voltage at four different temperatures	37
4.3	Zero-bias conductance as a function of gate voltage for two different values of 2DEG resistance	38
4.4	Minimum zero-bias conductance versus temperature for different values of 2DEG resistance	40
4.5	Minimum zero-bias conductance versus 2DEG resistance at different temperatures	41
4.6	Determining the effect of the back-gate voltage on the gate capacitance . .	43
4.7	Log-log plot of minimum zero-bias conductance versus temperature	45
4.8	Log-log plot of minimum zero-bias conductance versus environmental conductance	46
8.1	Current and conductance versus voltage for SIS-like junctions	59
8.2	Superconducting gap as a function of temperature	60

9.1	Current versus voltage for SNS-like junction	62
9.2	Shapiro steps	64
9.3	SQUID configuration	66
9.4	Current-voltage characteristic and voltage modulation as a function of applied flux for a dc SQUID	67
9.5	Circuit diagram for the flux-locked loop with flux modulation	69
9.6	Flux modulation	69
9.7	Noise spectra for dc SQUIDs	71
11.1	Diagram of the heart	78
11.2	Typical electrocardiogram	79
12.1	Diagram of second-order gradiometer	85
12.2	Photograph of the MCG system	86
12.3	Locations of the measurement channels relative to the subject	89
13.1	Definition of MCG intervals and waveform parameters	92
13.2	Magnetic field contour maps from a healthy control and an ischemic patient during repolarization	95
13.3	Definition of MCG map orientations	96
13.4	Averaged MCG time traces from a healthy volunteer	98
13.5	ROC curves for various MCG parameters	106

List of Tables

13.1 Comparison of male and female healthy volunteers	100
13.2 Comparison of older and younger healthy males	102
13.3 Comparison of older and younger healthy females	103
13.4 Comparison of ischemic patients with a subset of older healthy controls . .	105
13.5 Correlation between MCG map and waveform morphology parameters. Rest, post-exercise, and the exercise-induced change compared separately. .	109
13.6 Correlation between waveform parameters in channels located over the lower and left upper thorax. Rest, post-exercise, and the exercise-induced change compared separately.	110

Acknowledgments

I thank my advisor, John Clarke, for his encouragement and guidance. Without his unfailing belief in me, I would never have completed my doctorate. In his group I was able to work on a variety of experiments and was able to pursue my growing interest in medical devices. Few groups in Physics could have provided me with the same breadth of opportunities and experiences.

While in graduate school, I worked with many great researchers who have answered my questions, helped me in the lab, and taught me valuable skills. I thank Jan Kycia for taking me under his wing during my first years in the group working on single-electron transistors. Jan was a fabulous mentor and taught me an incredible amount about experimental physics. He was also a wonderful, good-natured person with whom to work. I thank Frank Wilhelm for many helpful discussions. I also thank Roy Therrien for his assistance and guidance during that time. During the magnesium diboride experiment, I had the opportunity to work with Yi Zhang and Darin Kinion. Besides being one of the most vibrant individuals I've ever met, Yi Zhang taught me a great deal about SQUID electronics. I also thank Darin Kinion for his endless willingness to help in the lab and to answer my questions. While working on magnetocardiography, I received assistance from many people. I thank Pate Thomson and Vickie Nolan for their helpful advice and guidance during the study. I heavily depended on their knowledge of cardiology and medicine. From them I learned much about clinical research and medical practice. I thank Alex Braginski, Nikolai Korsun, and Alexander Bakharev at CardioMag Imaging for their assistance with the project. Without their support and the support from many others at

CMI, the MCG project would not have been possible.

I also thank all the many members of the Clarke group, past and present, that I have been fortunate to meet. As members have noted in the past, the Clarke group is continually blessed with a great group of graduate students, post-docs, and visiting scholars. The atmosphere in the group is open and congenial, and I thank the members of the group for the uncountable times they have helped me during my five years in the group. A special thanks goes to Helene Grossman and Sherry (Hsiao-Mei) Cho for their support and friendship.

I also thank the staff at UC Berkeley and LBNL. Members of the administrative staff, including the Clarke group assistant, Barbara Salisbury, as well as Anne Takizawa and Donna Sakima, have been very helpful throughout the years. I also thank the members of the electronics shop, the student shop, and the machine shop for their assistance and guidance.

Finally, I thank my parents, Yi-Hsiang and Yu-Hsi, and my sisters, Jennie and Jackie, for their love and support throughout my life. I also thank the many friends who have supported me during these years, including my classmates at UC Berkeley with whom I shared the graduate school experience.

Chapter 1

Preface

1.1 Superconductivity

One of the most spectacular manifestations of quantum mechanics on a large scale is superconductivity. Below a critical temperature T_c and a critical magnetic field H_{c1} , superconductors exhibit perfect conductivity characterized by zero electrical resistance and perfect diamagnetism characterized by the expulsion of magnetic fields. In 1957 Bardeen, Cooper, and Schrieffer produced a microscopic explanation for this phenomenon [1]. In the superconducting state, electrons spontaneously form pairs, called Cooper pairs, under the influence of a phonon-mediated attractive force. The superconducting ground state is the product of many Cooper pair states in which each pair state has a probability amplitude of being occupied and an amplitude of being vacant. The magnitudes of the pair occupancy and vacancy amplitudes depend on the momentum of the constituent electrons, but the relative phase of the probability amplitudes is common for all states. This phase, θ , is a macroscopic quantum mechanical variable. At non-zero temperatures,

there exist excitations, called quasiparticles, that consist of unpaired electrons. According to the BCS theory, the quasiparticle energy is given by the expression

$$E_k(T) = \sqrt{\epsilon_k^2 + \Delta^2(T)} \quad (1.1)$$

where ϵ_k is the energy of an electron in a normal metal referred to the Fermi energy. The quasiparticle states are elevated in energy from the superconducting ground state by $\Delta(T)$, called the superconducting energy gap. The superconducting gap at $T = 0$ K, $\Delta(0)$, is a property of the material. The temperature dependence of the gap follows a universal curve that has been derived in the limit of low phonon-electron coupling. Additionally, in the low-coupling limit, the critical temperature and the superconducting gap at $T = 0$ K are related by the expression

$$2\Delta(0) = 3.52k_B T_c. \quad (1.2)$$

The BCS theory successfully explains the behavior of a class of superconductors, generally called low- T_c superconductors, for which the superconducting mechanism depends on a phonon-mediated attraction between electrons. In 1986, a class of copper-oxide materials was discovered with much higher critical temperatures on order of 100 K. Scientists continue to strive for a complete understanding of these high- T_c superconductors.

1.2 The Josephson junction

In 1962, B. D. Josephson made several astonishing predictions on the behavior of two superconductors separated by a thin insulating barrier[2]. These predictions are valid for any junction composed of two superconductors connected by a weak link, the so-called

Josephson junction. Josephson's first prediction was the existence of a supercurrent I_s that flows across the junction with zero applied voltage given by

$$I_s = I_c \sin \phi \quad (1.3)$$

where I_c is the critical current of the junction and $\phi \equiv \theta_2 - \theta_1$ is the phase difference across the junction. Josephson's second prediction related the time evolution of the phase difference with the bias voltage V :

$$\frac{d\phi}{dt} = 2eV/\hbar. \quad (1.4)$$

Equations 1.3 and 1.4 imply that a dc bias voltage produces an oscillating current across the junction. These relations also imply that energy is stored in the junction of the form

$$-E_J \cos \phi \quad (1.5)$$

where

$$E_J \equiv \hbar I_c / 2e \quad (1.6)$$

is the Josephson energy (see Sec. 6.1 in Ref. [3]). The critical current of a junction depends on the superconducting material and the physical dimensions of the insulating barrier. The product of the critical current and the normal state resistance of the junction, R_n , is independent of junction geometry and can be expressed as [4]

$$\begin{aligned} I_c R_n &= \frac{\pi \Delta(T)}{2e} \tanh \left(\frac{\Delta(T)}{2k_B T} \right) \\ &\approx \frac{\pi \Delta(0)}{2e} \quad \text{for } T \ll T_c. \end{aligned} \quad (1.7)$$

Using Eqs. 1.6 and 1.7, one can rewrite the Josephson energy as

$$E_J = \frac{\hbar \pi \Delta(T)}{4e^2 R_n} \tanh \left(\frac{\Delta(T)}{2k_B T} \right)$$

$$\approx \frac{\hbar\pi\Delta(0)}{4e^2R_n} \quad \text{for } T \ll T_c. \quad (1.8)$$

The Josephson relations describe the behavior of an ideal Josephson junction. A basic model of a more physical Josephson junction is the resistively and capacitively shunted junction (RCSJ) model. As depicted in Fig. 1.1(a), an ideal Josephson junction, symbolized by a cross, is shunted by the junction capacitance and a resistor representing quasiparticles flowing through the junction. Summing the current through the three current paths yields

$$I = I_c \sin \phi + \frac{V}{R} + C \frac{dV}{dt}. \quad (1.9)$$

Replacing V using Eq. 1.4 and I_c using Eq. 1.6, we can rewrite the above equation as

$$\left(\frac{\hbar}{2e}\right)^2 C \ddot{\phi} = \left[-E_J \sin \phi + \frac{\hbar I}{2e}\right] - \left(\frac{\hbar}{2e}\right)^2 \frac{1}{R} \dot{\phi}. \quad (1.10)$$

This equation of motion for ϕ is equivalent to that of a particle in a tilted washboard potential, as illustrated in Fig. 1.1(b), where the particle mass is proportional to the capacitance, the damping is inversely proportional to R , and the tilt of the washboard is proportional to the bias current. To find the current-voltage behavior of the junction, Eq. 1.10 can be solved for $\dot{\phi}$ which is related to the voltage using the second Josephson relation, Eq. 1.4. Depending on the parameters C and R , Eq. 1.10 can produce different current-voltage characteristics.

One regime is obtained if we assume that the damping term is small relative to the capacitive term, or that $\beta_c \equiv 4\pi e I_c R^2 C / \hbar \gg 1$. In this limit, the underdamped limit, at zero applied bias current the phase will oscillate about a minimum of the potential well

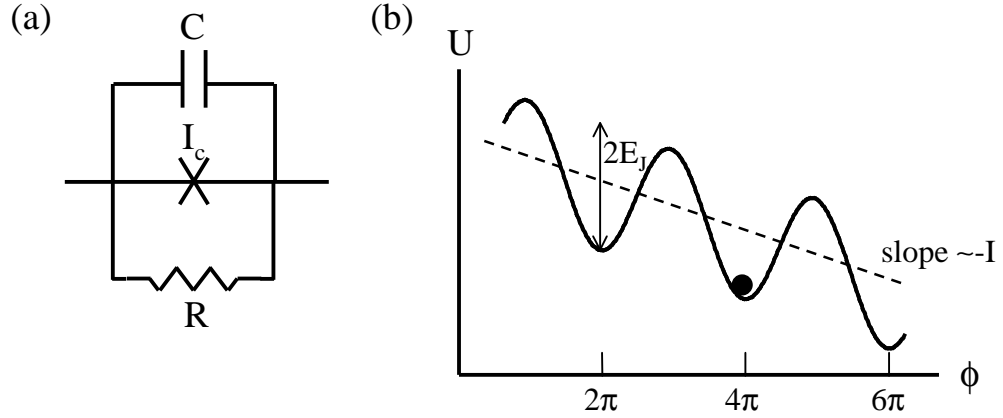


Figure 1.1: Resistively and capacitively shunted junction (RCSJ) model. (a) Circuit diagram. (b) Tilted washboard potential.

at the plasma frequency

$$\omega_p \equiv \sqrt{\frac{2eI_c}{\hbar C}}. \quad (1.11)$$

Applying a small bias current tilts the potential. The phase remains trapped in the well, and the voltage across the junction, proportional to $\dot{\phi}$, remains zero. When I reaches I_c , the potential minimum disappears and the phase slides down the slope. At this stage Cooper pairs begin to break and correspondingly the voltage jumps to $2\Delta/e$. As more current is applied, the junction behaves as if it were in the normal state. If we now decrease the current, the tilted washboard begins to level. The phase continues to slide down the potential until it retraps at the minimum of a well. For low damping, this does not occur until the current approaches zero. Thus the current-voltage curve is hysteretic as shown in Fig. 1.2.

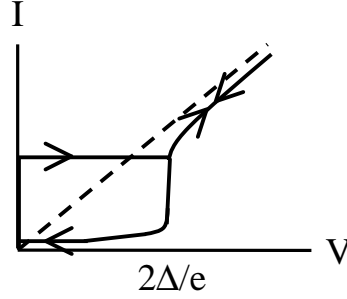


Figure 1.2: Ideal current-voltage behavior of an underdamped Josephson junction at $T = 0$ K

1.3 Josephson junction devices

Over the past decades, researchers have developed many devices exploiting the remarkable properties of the Josephson junction. These devices are widely used in fundamental physics research. For example, Josephson junction devices can act as model systems whose parameters can be more easily controlled experimentally than their physical analogs. Researchers have used these model systems to study the Kondo effect, the interaction of the electronic states of an impurity atom with those of a metal [5], and to study quantum mechanical phase transitions [6]. Josephson junction devices are also macroscopic quantum mechanical systems. The phase difference across a Josephson junction is a quantum mechanical variable which determines a macroscopic quantity, the current through the junction. Using various Josephson junction devices, scientists have observed the tunneling of a macroscopic variable [7], the superposition of two macroscopically distinct states [8, 9, 10], as well as the coherent oscillations between two states [11].

Josephson junction devices are also providing technological advancements for many commercial applications. For example, devices are being developed as sensitive detectors of microwave electromagnetic radiation and as low-noise amplifiers [12]. The

most widely used Josephson junction device, the superconducting quantum interference device (SQUID), consists of a superconducting loop interrupted by either one or two Josephson junctions. It is the most sensitive detector of magnetic flux and is employed in a variety of applications [13]. The SQUID is used to measure magnetic susceptibility and is being developed to nondestructively detect structural features in materials such as steel. SQUIDs are also sensitive enough to measure magnetic signals produced by the body. Magnetoencephalography (MEG), measurement of the magnetic field from the brain, is one of the few techniques that provides high time-resolved information on the activity of the brain. There is also great interest in using SQUIDs for magnetocardiography (MCG), measurement of the magnetic fields from the heart.

The vast potential of SQUIDs and other Josephson junction devices, however, is tempered by the cost of cooling them. It can also be quite costly to shield SQUID-based instruments from external magnetic field noise. There is continual interest in decreasing these costs to increase the practicality of the devices. High- T_c superconducting devices are less expensive to cool but have inferior noise properties compared with low- T_c devices. Closed-cycle refrigeration units, called cryocoolers, are being developed to decrease the cost of cooling low- T_c devices. Additionally, there have been great advancements in techniques to decrease the effect of external magnetic field noise on SQUID instruments. These include the development of gradiometers which are less sensitive to the more uniform magnetic fields produced by distant noise sources.

In this dissertation I will describe three experiments using Josephson junction devices that touch on many of their various uses. Part I describes an experiment using a

Josephson junction device as a macroscopic quantum mechanical system. The device is a superconducting single-electron transistor (sSET) which consists of a small superconducting island connected by Josephson junctions to superconducting leads. Using the sSET coupled capacitively to a resistive ground plane, we studied the effect of dissipation on tunneling between charge states. The ground plane was provided by a two-dimensional electron gas (2DEG) imbedded in a semiconductor substrate. By depleting the 2DEG, we were able to change the resistance of the ground plane, and thus vary the amount of dissipation coupled to the system. In this manner, we quantitatively mapped out the effect of dissipation for comparison with theoretical calculations.

Part II describes an experiment on point-contact junctions using magnesium diboride, a material that was discovered just two years ago to be a superconductor at the relatively high temperature of 39 K. This discovery generated intense interest in uncovering the superconducting mechanism in this material and in exploring its application potential. To form point contacts, we mounted a MgB_2 tip on a movable rod whose distance from a base piece could be adjusted. In this manner we formed junctions with a variety of characteristics and performed a series of experiments using this technique. First we measured the tunneling of quasiparticles across the junctions to investigate the superconducting gap of the material. We also measured SQUIDs made from the material with low-noise properties.

Part III involves one of the medical applications of Josephson junction devices mentioned above, magnetocardiography (MCG). Using one of the first commercial systems designed to work in an unshielded environment, we performed a clinical MCG study at

the Alta Bates Summit Medical Center in Oakland and Berkeley in collaboration with a cardiologist, Pate Thomson. We measured over 50 healthy volunteers to determine the variations in the normal MCG. We also measured a small number of cardiac patients to investigate the possible signatures of disease in the MCG.

Part I

The Effect of Dissipation on a Superconducting Single-Electron Transistor

Chapter 2

Introduction

2.1 Dissipation in macroscopic quantum mechanical systems

The field of quantum mechanics traditionally has focused on small physical systems. These systems can be weakly coupled to other environmental variables and in some limit can be considered isolated. Increasingly, scientists are interested in studying macroscopic quantum mechanical systems, systems containing large numbers of constituents that nonetheless can be described by a small number of macroscopic quantum mechanical variables. It is more difficult to isolate these large systems, and, on a microscopic level, the interaction of these systems with the environment is extremely complicated. The net loss of energy from the system to the many unseen environmental degrees of freedom is called dissipation. The effect of dissipation on a system can be described phenomenologically by damping or friction coefficients, but the actual nature of the microscopic interactions may not be known.

In the early 1980's, an important theoretical technique to incorporate dissipation

into quantum mechanical calculations was developed [14, 15]. This technique was then used to calculate the effect of dissipation on tunneling of macroscopic quantum mechanical variables. The idea proposed by Caldeira and Leggett was to construct terms in the Lagrangian for the environment and the interaction of the environment with the system that do not depend on the actual microscopic details of the interaction. The environment was represented as an infinite number of microscopic variables, all of which are only weakly disturbed by the system. Because each environmental variable interacts only weakly with the system, we can model the environmental variable as a harmonic oscillator that is linearly forced by the system. The masses, natural frequencies, and coupling coefficients for the infinite bath of harmonic oscillators are constrained by the phenomenological friction parameters but are otherwise undetermined. Miraculously, however, calculations of the tunneling rate depend only on the phenomenological coefficients and not on the choice of harmonic oscillator parameters.

Josephson junction devices provide ideal quantum mechanical systems in which to study the effect of dissipation. Many experiments have been performed to study the tunneling of the phase difference across the Josephson junction coupled to a dissipative shunting resistor [16]. Experiments were also performed in which the dissipation coupled into the system could be varied *in situ* [17]. The results of these experiments are in good agreement with the theoretical calculations. Fewer experiments have focused on tunneling in systems where charge is a good quantum mechanical variable [18]. In this experiment, we studied tunneling between charge states in a system coupled to a tunably dissipative environment [19].

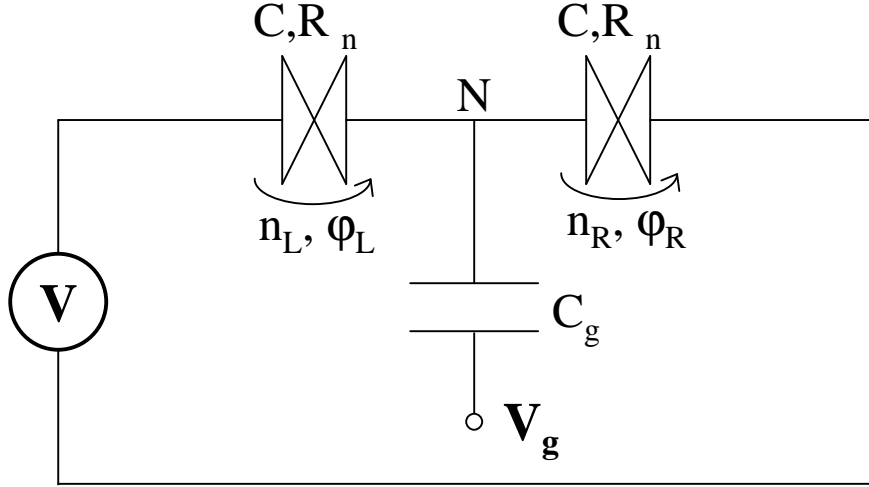


Figure 2.1: Circuit diagram of an ideal sSET without dissipation. Parameters: C = junction capacitance; R_n = normal state resistance, C_g = gate capacitance. Control parameters: V = bias voltage; V_g = gate voltage. Variables: n_L and n_R = number of Cooper pairs that have crossed each junction respectively; ϕ_L and ϕ_R = phase difference across each junction. $N = n_L - n_R$ = number of Cooper pairs on the island.

2.2 The superconducting single-electron transistor and Coulomb blockade

A superconducting single-electron transistor (sSET) consists of a superconducting island connected to superconducting leads by Josephson junctions. Figure 2.1 contains the circuit diagram of an ideal sSET, ignoring the dissipative aspects of the environment. Each junction has a capacitance, C , and a normal state resistance, R_n . The island is capacitively coupled to a gate with capacitance C_g . The parameters that can be controlled in the experiment are the applied bias voltage V and the applied voltage on the gate V_g . The phase differences across the Josephson junctions, ϕ_L and ϕ_R , are macroscopic quantum mechanical variables. The number of Cooper pairs that have been transferred across the junctions, n_L and n_R , are also quantum mechanical variables. The number and phase

variables for each junction are conjugates and obey the uncertainty relation [20]

$$\Delta n \Delta \phi \geq 1/2. \quad (2.1)$$

At $T = 0$ K and for zero applied bias voltage, the Hamiltonian for this ideal system consists of the electrostatic energy of the island and the Josephson energies of the two junctions:

$$\begin{aligned} H &= \frac{(2eN - C_g V_g)^2}{2C_\Sigma} - E_J \cos \phi_L - E_J \cos \phi_R \\ &= 4E_c (N - C_g V_g / 2e)^2 - E_J \cos \phi_L - E_J \cos \phi_R. \end{aligned} \quad (2.2)$$

where $N = n_L - n_R$ is the number of Cooper pairs on the island and $C_\Sigma = 2C + C_g$ is the total capacitance of the island. The charging energy,

$$E_c \equiv \frac{e^2}{2C_\Sigma}, \quad (2.3)$$

is the energy required to add or remove a single electron from the island. In terms of charge states, the Josephson terms in the Hamiltonian can be reexpressed as [20]

$$\begin{aligned} -E_J \cos \phi_L - E_J \cos \phi_R &= -\frac{E_J}{2} (e^{i\phi_L} + e^{-i\phi_L}) - \frac{E_J}{2} (e^{i\phi_R} + e^{-i\phi_R}) \\ &= -\frac{E_J}{2} (|n_L + 1\rangle \langle n_L| + |n_L - 1\rangle \langle n_L|) \\ &\quad -\frac{E_J}{2} (|n_R + 1\rangle \langle n_R| + |n_R - 1\rangle \langle n_R|). \end{aligned} \quad (2.4)$$

The electrostatic term in the Hamiltonian creates a barrier for Cooper pairs to flow across the junctions; it requires energy $4E_c$ to change the island charge by one Cooper pair. For temperatures $k_B T < 4E_c$ and for $E_J < 4E_c$, charge states are well-defined and transport properties of the device are influenced by ‘‘Coulomb blockade’’ effects. In this case we can

consider the Josephson coupling to be a perturbation leading to the incoherent tunneling of Cooper pairs.

The charging energy barrier to tunneling and therefore the transport properties of the sSET depend on the gate voltage. As depicted in Fig. 2.2, the energies of different charge states form parabolas as functions of the gate voltage. The charging barrier at any particular gate voltage is the difference in energy between the charge state with the lowest energy and the state with the next lowest energy. As the gate voltage is swept, transport properties such as the zero-bias conductance, G_0 , should be modulated with period $2e/C_g$. Quasiparticles in the system, however, can poison this $2e$ periodicity [21, 22]. Quasiparticles can be thermally excited at non-zero temperatures and can also exist in defect states in the material. Although Cooper pair tunneling provides the majority of the charge transport through the sSET, quasiparticle movement on and off the island or gate can effectively shift the gate voltage by e/C_g and thus decrease the effective charging barrier. As depicted in Fig. 2.2, transport properties of the sSET become $1e$ periodic with gate voltage and modulate less strongly with gate voltage.

2.3 The sSET with dissipation

The ideal sSET model can now be coupled to a dissipative environment. The full microscopic details of the environment and its interaction with the system are complicated but the net effect can be summarized by a single parameter, the effective complex impedance $Z_{eff}(\omega)$ across each of the junctions. The effective impedance across the junctions can be estimated from the details of the sample structure. In this experiment, the

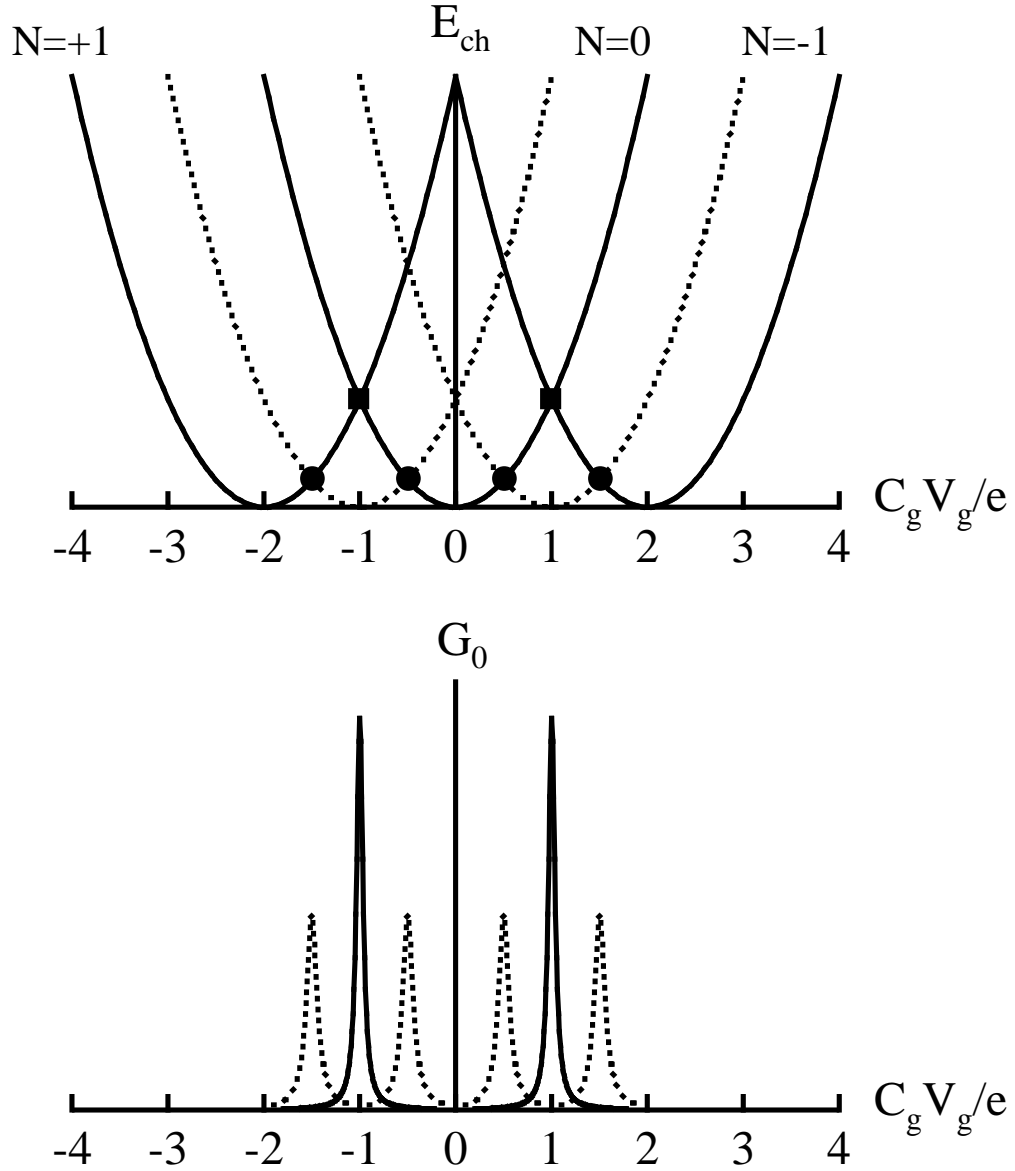


Figure 2.2: Top: Energy levels of charge states of the sSET as a function of gate voltage. Squares label charge state degeneracy points. Circles label degeneracy points of charge states including those shifted by $1e$. N = number of Cooper pairs on the island; C_g and V_g = gate capacitance and voltage; $E_{ch} = (2eN - C_g V_g)^2 / 2C_\Sigma$ is the charging energy where C_Σ = the total capacitance of the island. Bottom: Zero-bias conductance, G_0 , of the sSET as a function of gate voltage. Solid lines: without poisoning by quasiparticles, Dashed lines: with poisoning by quasiparticles.

effective impedance can also be varied *in situ*.

The effect of the dissipative environment is to produce voltage fluctuations across the junctions. We can relate the voltage fluctuations to $Z_{eff}(\omega)$ using the generalized Johnson-Nyquist theorem [23]. The Fourier transform of the voltage correlation function, $\langle \delta V(0) \delta V(t) \rangle$ where $\langle \rangle$ denotes an ensemble average, is given by

$$\frac{1}{2\pi} \text{Re} [Z_{eff}(\omega)] \hbar \omega \coth \left(\frac{\hbar \omega}{k_B T} \right). \quad (2.5)$$

These voltage fluctuations can be related to phase fluctuations $\delta \phi(t)$ using the second Josephson relation, Eq. 1.4. The Josephson coupling terms of the Hamiltonian then become

$$-E_J \cos \phi \rightarrow -E_J \cos (\phi + \delta \phi) = -\frac{E_J}{2} \left[e^{i(\phi + \delta \phi)} + e^{-i(\phi + \delta \phi)} \right]. \quad (2.6)$$

The factors involving $e^{\pm i \delta \phi}$ create transitions in the environment during the tunneling process. According to Caldeira and Leggett [14, 15], the environment can be modeled theoretically as an infinite bath of harmonic oscillators,

$$H_{bath} = \sum_{\alpha} \left[\frac{p_{\alpha}^2}{2m_{\alpha}} + \frac{m_{\alpha} \omega_{\alpha}^2}{2} x_{\alpha}^2 \right]. \quad (2.7)$$

The fluctuating voltage is produced by a linear coupling with the bath,

$$\delta V(t) = \sum_{\alpha} \lambda_{\alpha} x_{\alpha}(t). \quad (2.8)$$

The appropriate choice of the bath parameters m_{α} , ω_{α} , and λ_{α} will reproduce the voltage fluctuations in Eq. 2.5. However, as Appendix A details, the tunneling calculations do not require a particular set of bath parameters to be chosen. Only the parameter $Z_{eff}(\omega)$ is necessary to determine the effect of the dissipative environment. For this experiment, the

dependence of the zero-bias conductance on temperature and dissipation are compared with calculations based on this technique.

Chapter 3

Experimental Methods

3.1 Sample preparation

3.1.1 GaAs/AlGaAs heterostructure substrate

To make samples with controllable environmental dissipation, we fabricated the sSET device on top of a GaAs/AlGaAs heterostructure with an imbedded two-dimensional electron gas (2DEG) located 110 nm below the top surface of the substrate. The 2DEG acts as a dissipative ground plane for the device. This dissipative environment can be controlled *in situ* by applying large voltages to a metallic gate on the back of the substrate, depleting the electrons from the 2DEG and thus changing its surface resistance. This technique was pioneered several years ago by Alex Rimberg and Çağlıyan Kurdak as postdoctoral researchers in the Clarke group.

The heterostructures we used were manufactured by K. L. Campman and A. C. Gossard at the University of California, Santa Barbara. The substrates were grown

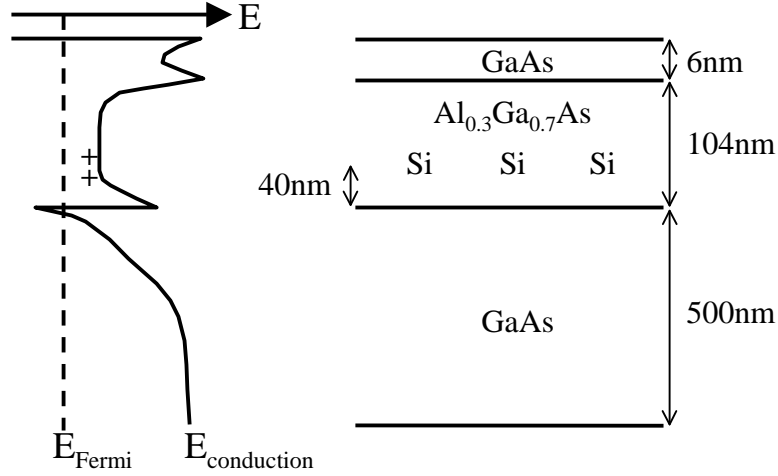


Figure 3.1: Physical structure and conduction band structure of GaAs/AlGaAs heterostructure with imbedded two-dimensional electron gas.

on a GaAs substrate using molecular beam epitaxy and consisted of the following layers from bottom to top: 500 nm of GaAs, 104 nm of Al_{0.3}Ga_{0.7}As, and 6 nm of GaAs. The Al_{0.3}Ga_{0.7}As was selectively doped with Si donors located 40 nm above the lower GaAs/AlGaAs interface. As Fig. 3.1 depicts, the conduction band structure of the substrate has a triangle shaped potential well that dips below the Fermi energy at the lower interface between the GaAs and the Al_{0.3}Ga_{0.7}As. Electrons supplied by the donors collect in this well forming the 2DEG.

To prepare the substrate for our samples, the back of the heterostructure was thinned using a hand lapping tool until the total thickness of the substrate was 251 μm . We then cleaved the substrate into 2 mm x 2 mm squares. Ohmic electrical contacts to the 2DEG were formed by alloying InSn at the corners of the substrate. After the sSET was fabricated on the top surface, as will be described in the next section, the substrate and sample were mounted on a copper back gate on the sample stage of a dilution refrigerator unit.

3.1.2 Microfabrication of the sSET

The dynamics of the sSET depend on two energy scales, the charging barrier to tunneling, $4E_C$, and the Josephson coupling energy, E_J . To observe the quantum mechanical behavior of the sSET, $4E_C/k_B$ and E_J/k_B must be greater than the temperature T . We can achieve temperatures down to 20 mK by cooling our samples using a dilution refrigerator. According to Eq. 1.8, fabricating low-resistance insulating barriers increases the E_J of our samples. To increase E_C , it is necessary to fabricate small capacitance junctions and island in accordance with Eq. 2.3. Making small capacitance junctions with correspondingly small areas requires special microfabrication techniques: electron beam lithography and two-angle shadow evaporation [24].

Electron beam lithography refers to the creation of a mask using an electron beam to define its features. A resist is spun onto the substrate and then a pattern is drawn out on the resist-coated substrate using an electron beam. Exposure to the electron beam changes the solubility of the resist. Positive resists become more soluble while negative resists become less soluble when exposed. Development of the exposed substrate in a solution bath produces the mask. To create a shadow mask, we applied two layers of positive resist to the substrate. The lower layer is more sensitive to the electron beam than the upper layer. When the substrate is exposed to the electron beam and then developed in solution, the mask will be undercut as depicted in Fig. 3.2.

Figure 3.3(a) depicts the central region of the sSET mask showing the critical features. The island is sandwiched by wide leads on each side. Attached to the leads and the island are short narrow arms that will form the junctions. There is a gap between

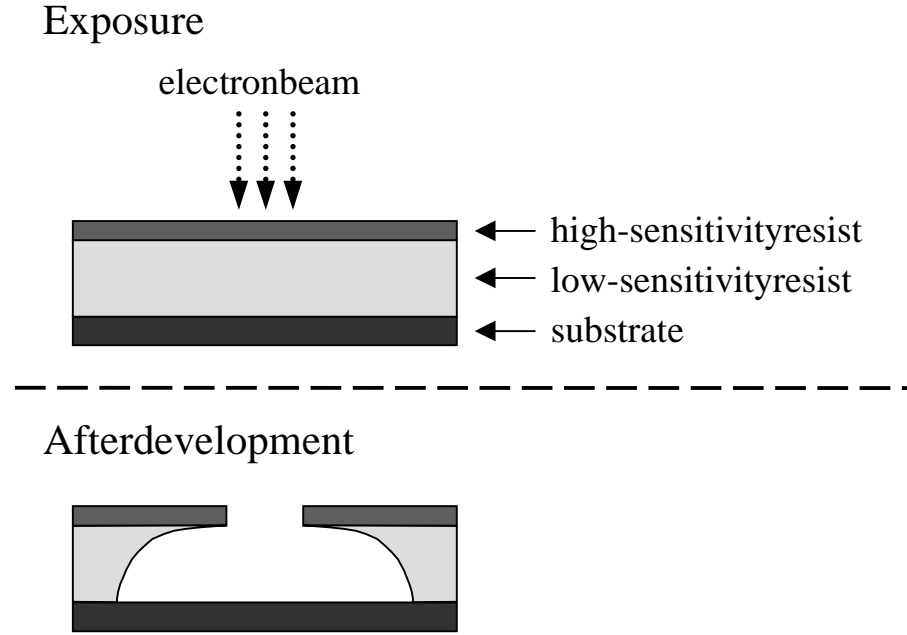


Figure 3.2: Shadow mask fabrication

the arm from the lead and the arm from the island in the top portion of the mask, but, as depicted in Fig. 3.3(b), the region below the gap is completely undercut. Evaporating aluminum onto the mask from two different angles causes the vertical arm from the top layer to overlap with the horizontal arm from the bottom layer. Introducing oxygen gas into the evaporation chamber between the two depositions oxidizes the surface of the bottom layer of aluminum creating a thin insulating barrier of aluminum oxide. To control the resistance of the junctions, we varied the pressure of the oxygen gas as well as the oxidizing time. Figure 3.3(c) depicts the side view of the junction structure showing the two superconducting layers separated by the insulating barrier.

Figure 3.4 is a scanning electron microscope (SEM) image of one of our sSET samples. The dual shifted images are the two layers of aluminum deposited from opposing

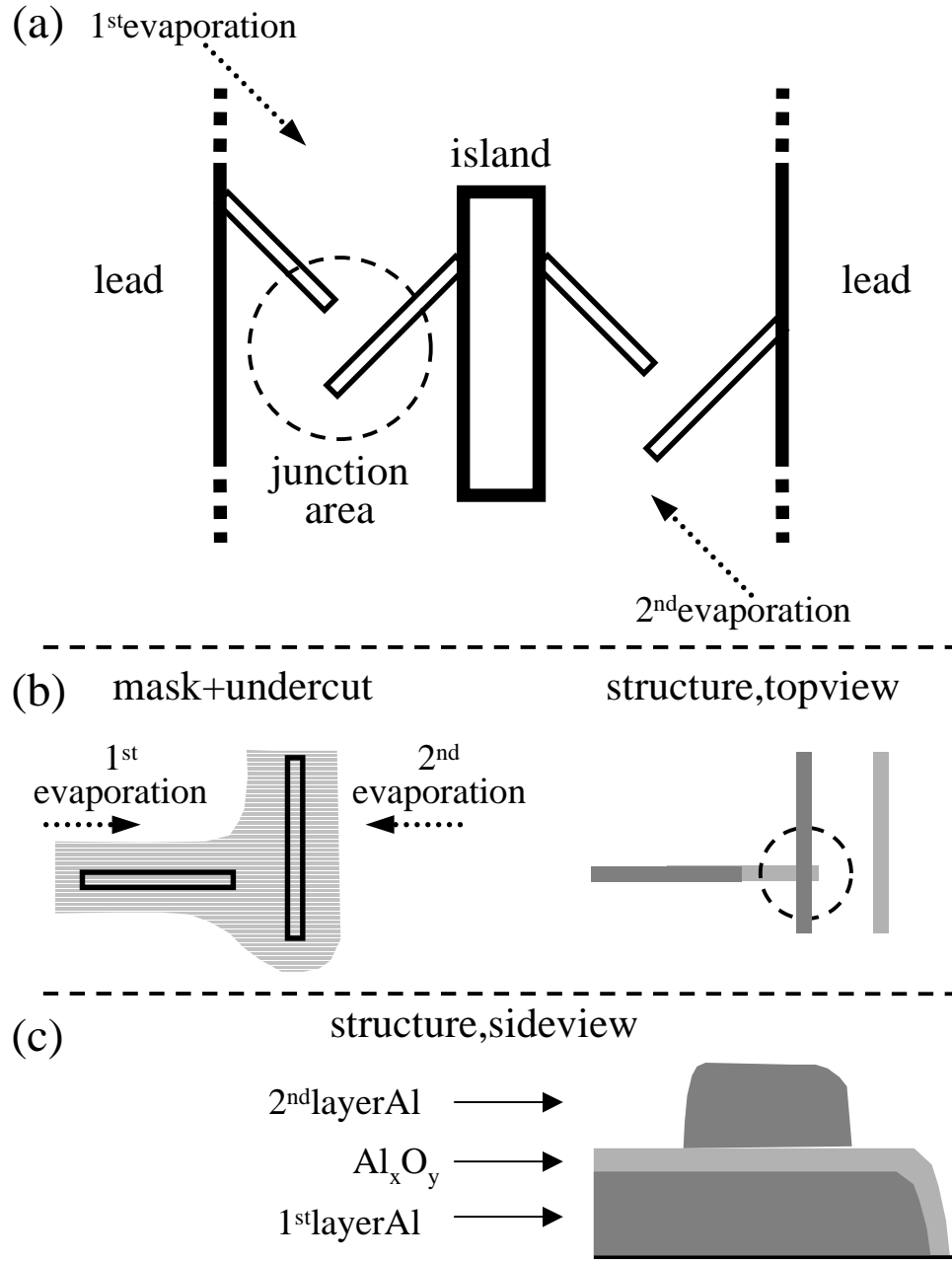


Figure 3.3: (a) The central region of the top portion of the sSET mask. (b) Highlight of the junction area. Left: Top portion of the mask with the region below completely undercut. Right: Top view of the junction structure after two evaporations from opposing angles. The vertical arm from the top layer (dark grey) overlays the horizontal arm from the lower layer (light grey). (c) Side view of the Josephson junction structure.

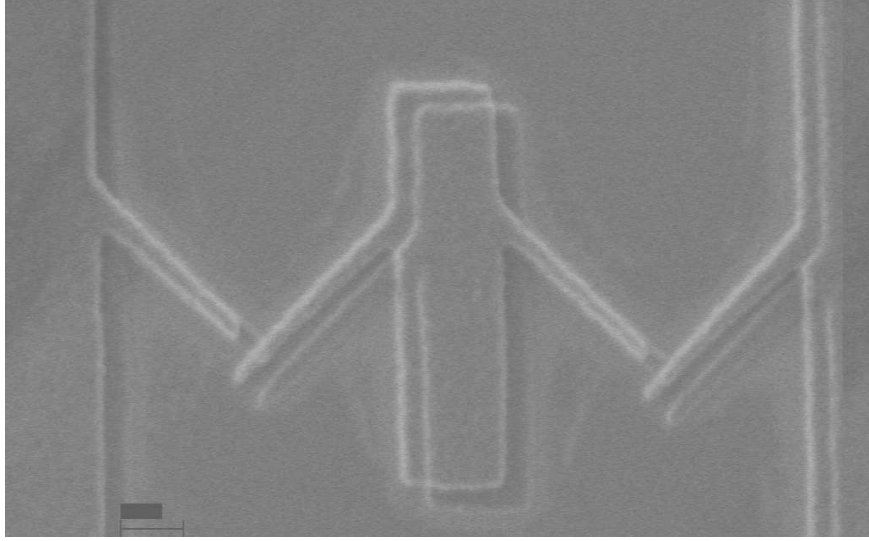


Figure 3.4: Scanning electron microscope image of an sSET. Island: $0.5 \mu\text{m} \times 2 \mu\text{m}$. Leads: $10 \mu\text{m}$ wide. Junctions: $90 \text{ nm} \times 90 \text{ nm}$.

angles. The bottom layer of aluminum is approximately 20 nm thick, and the top layer is approximately 35 nm thick. The bottom layer of aluminum was oxidized by introducing 400 mtorr of a 95% argon, 5% oxygen gas mixture into the evaporation chamber for three minutes. The junctions are located at the intersection of the arms from the bottom and top layers as discussed above. From zoomed SEM images, the junction area is estimated to be $90 \text{ nm} \times 90 \text{ nm}$. The two overlapping layers of aluminum of the island and the leads form large critical current Josephson junctions that effectively act as superconducting shorts at low bias currents and voltages. The island dimensions are $0.5 \mu\text{m} \times 2 \mu\text{m}$. Both leads are $10 \mu\text{m}$ wide and extend far beyond the boundaries of Fig. 3.4. Each lead splits into two leads which run into two separate contact pads. The length of the leads from the junctions to each of the four contact pads is $760 \mu\text{m}$.

3.2 Sample characterization

3.2.1 The sSET

Figure 3.5 contains the circuit diagram for our sSET sample coupled to the 2DEG. The gate voltage V_g is applied to the 2DEG ground plane through one of the InSn ohmic contacts. The back-gate voltage V_{bg} is applied to the metallic gate on the back of the substrate and controls the sheet resistance of the 2DEG, R_{2D} . The normal state resistances of each junction, R_n , were assumed to be equal and were measured to be 18 k Ω at 1.2 K using a four terminal configuration. Assuming a specific capacitance of 45 fF/ μm^2 [25], the junction capacitance C of the 90 nm x 90 nm junctions was estimated to be 0.37 fF. To measure the gate capacitance, we applied a large magnetic field to the sample, driving the aluminum normal, and determined the periodicity of the zero-bias conductance with respect to the gate voltage which is periodic with period e/C_g in the normal state. We estimated a gate capacitance of 1.8 fF.

Using the measured and estimated sSET parameters, we calculated the two important energy scales: the charging barrier, $4E_C$, and the Josephson coupling energy, E_J . Using Eq. 2.3 we calculated a charging barrier of $E_C/k_B \approx 1.5$ K. Using the low temperature limit of Eq. 1.8 and the known superconducting gap in aluminum, $\Delta(0) = 0.17$ meV, we calculated a Josephson energy of $E_J/k_B \approx 380$ mK. For this set of parameters, the sample should be well described by the charge state picture for temperatures ≤ 300 mK.

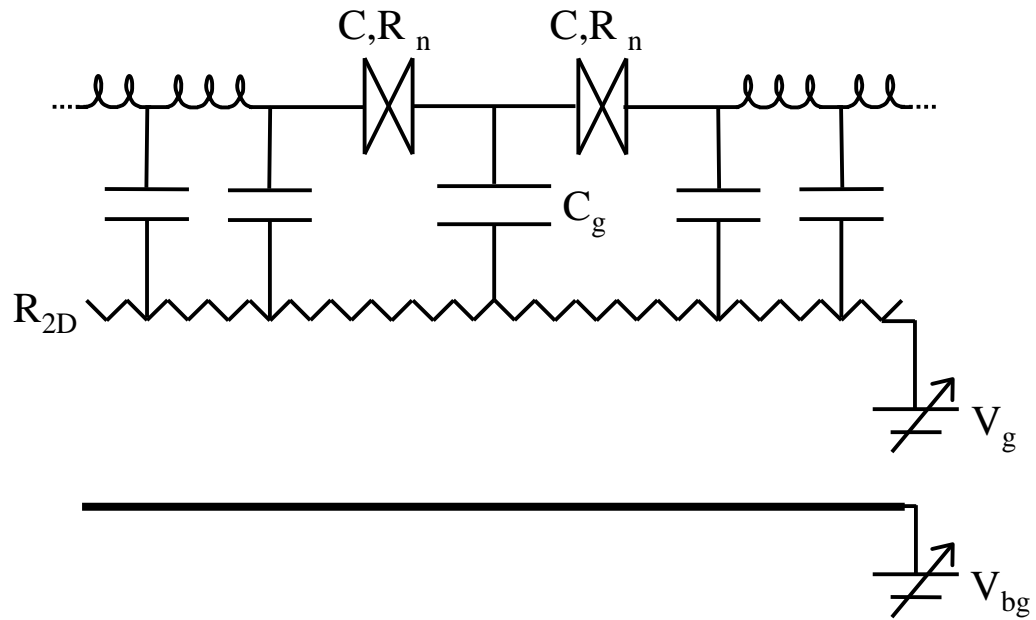


Figure 3.5: Diagram of the sSET coupled to a 2DEG. C and R_n are the junction capacitance and resistance, assumed to be the same for both junctions. C_g is the capacitance of the island to the ground plane which acts as the gate. R_{2D} is the sheet resistance of the 2DEG. V_g is the gate voltage applied to the 2DEG. V_{bg} is the back-gate voltage that depletes the 2DEG and changes the ground plane resistance.

3.2.2 The dissipative ground plane

To characterize the 2DEG, we measured its sheet resistance, R_{2D} , using the Van der Pauw method [26]. Figure 3.6 depicts the lead configuration for this measurement. For an approximately square sample, the sheet resistance is found using the formula

$$R_{2DEG} \approx \frac{\pi}{\ln 2} \frac{R_{24,13} + R_{34,12}}{2} \quad (3.1)$$

where $R_{24,13} = V_{24}/I_{13}$. Figure 3.7 plots R_{2D} as a function of the back-gate voltage. As we apply larger negative back-gate voltages, we deplete the charge carriers in the 2DEG and increase the sheet resistance. The sheet resistance of the 2DEG increases from 160 Ω/\square for $V_{bg} = 0$ V to 600 Ω/\square for $V_{bg} = -300$ V. The resistance between two electrodes placed along opposite edges of a rectangular section of a sheet is given by

$$\text{Resistance (in } \Omega) = \frac{\text{Sheet resistance (in } \Omega/\square) \times \text{length of rectangle}}{\text{width of rectangle}}. \quad (3.2)$$

3.2.3 The leads

The leads running from the junctions to the contact pads are quite long, 760 μm . Therefore it is appropriate to model them as microstrip transmission lines as in Fig. 3.8. The width of the leads, w , is 10 μm , and the distance between the lead and the ground plane, d , is 0.1 μm . For an aspect ratio w/d of 100, we neglect the fringing effects of the electric and magnetic fields. We will also neglect the small contribution to the inductance from the electromagnetic properties of the superconducting lead (see Sec. 3.09 in Ref. [12]). In this simple approximation, the distributed capacitance is $c_t \approx \epsilon_o \epsilon w/d \approx 10^{-8}$ F/m

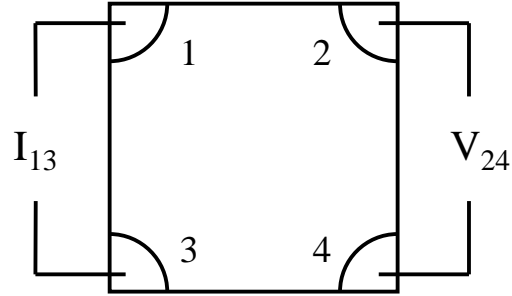


Figure 3.6: Van der Pauw measurement configuration used to measure the sheet resistance of the 2DEG

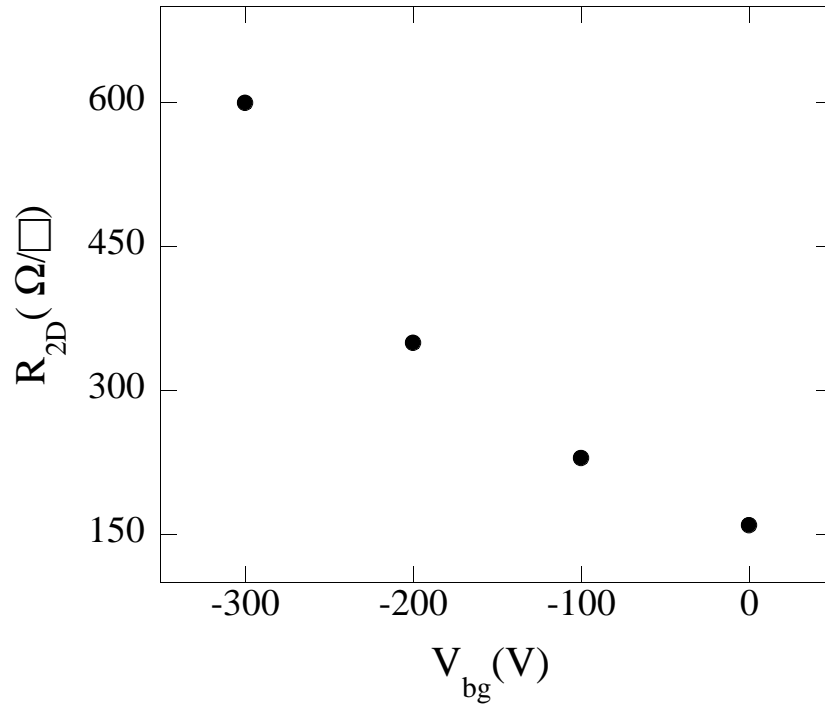


Figure 3.7: 2DEG sheet resistance R_{2D} as a function of the back-gate voltage V_{bg} .

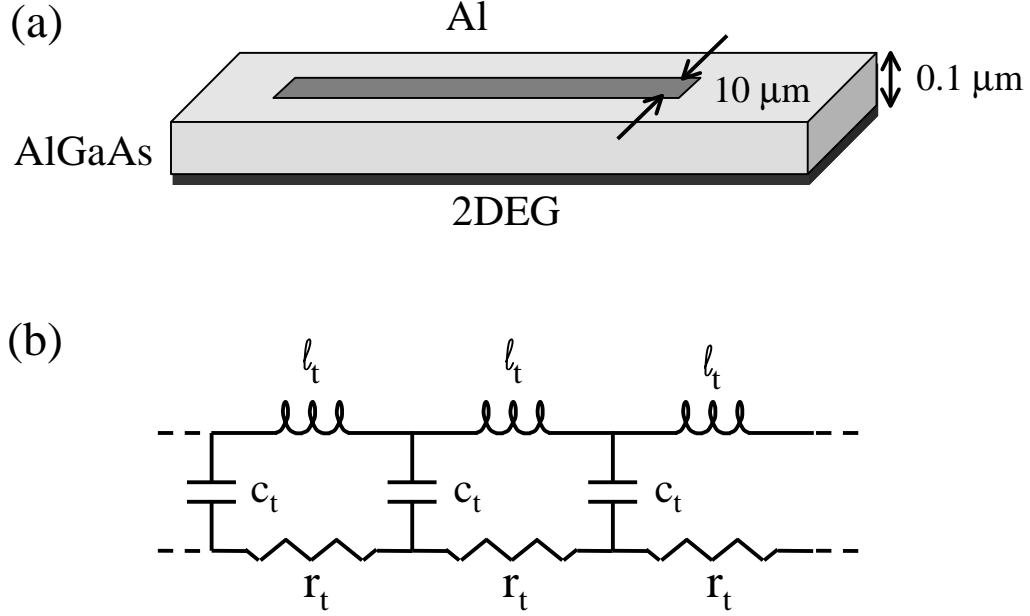


Figure 3.8: (a) Diagram of the leads to the sSET (not to scale) (b) Transmission line model of the leads: ℓ_t = inductance per unit length; c_t = capacitance per unit length; r_t = resistance per unit length

where $\epsilon \approx 12$ is the dielectric constant for AlGaAs. The approximate inductance per unit length is $\ell_t \approx \mu_o \mu d/w \approx 10^{-8}$ H/m where $\mu \approx 1$ is the permeability of AlGaAs. The resistance per unit length can be estimated using Eq. 3.2 to be $r_t \approx R_{2D}/w$. As we vary the back-gate voltage from 0 V to -300 V, we vary r_t from 16 - 60 M Ω /m.

The impedance of the transmission line is highly dependent on frequency. It is convenient to estimate a frequency range of interest based on the dynamics of the sSET. The Cooper pair tunneling frequency is one characteristic frequency. For a typical bias current of 0.34 nA, the tunneling frequency can be estimated as $I/2e \approx 1$ GHz or 10^8 rad/s. The plasma frequency defined in the Preface may also be considered. Using Eq. 1.11 and Eq. 1.7 we find that $\omega_p = (\pi\Delta/\hbar CR_n)^{1/2} \approx 3.5 \times 10^{11}$ rad/s. We are therefore most interested in frequencies from $10^8 - 10^{12}$ rad/s.

For an infinite transmission line, the complex impedance is given by [27]

$$Z_t(\omega) = \sqrt{\frac{r_t + i\omega\ell_t}{i\omega c_t}}. \quad (3.3)$$

For frequencies lower than $r_t/\ell_t \approx 10^{15}$ rad/s, the resistive term dominates over the inductive term and the impedance of the transmission line can be approximated as

$$Z_t(\omega) \approx \sqrt{\frac{r_t}{2\omega c_t}}(1 - i). \quad (3.4)$$

The leads of the sSET have a length, L , of 760 μm . They are terminated by large contact pads. The impedance of a lead terminated by a contact pad with impedance Z_p is given by

$$Z_t \frac{Z_p + Z_t \tanh \gamma L}{Z_t + Z_p \tanh \gamma L} \quad (3.5)$$

where

$$\gamma = \sqrt{(r_t + i\omega\ell_t)i\omega c_t} \approx \sqrt{\frac{\omega r_t c_t}{2}}(1 + i) \quad \text{for } \omega < 10^{15} \text{ rad/s}. \quad (3.6)$$

For frequencies greater than 10^7 rad/s, $\tanh \gamma L \approx 1$ and thus the impedance of the leads is approximately the infinite-transmission-line impedance $Z_t(\omega)$ in Eq. 3.4.

3.2.4 The effective impedance across the junction

We are now ready to estimate the effective impedance across one of the Josephson junctions. Figure 3.9(a) is a condensed circuit diagram of the sSET with the leads represented by the transmission line impedance from Eq. 3.4. The resistance of the 2DEG between the island and the lead was estimated to be $R_{2D}/3$ based on the lateral spread of the current flowing from the island to the lead. Focusing on the left junction in Fig. 3.9(a), we see that the right junction effectively isolates the right half of the circuit diagram from

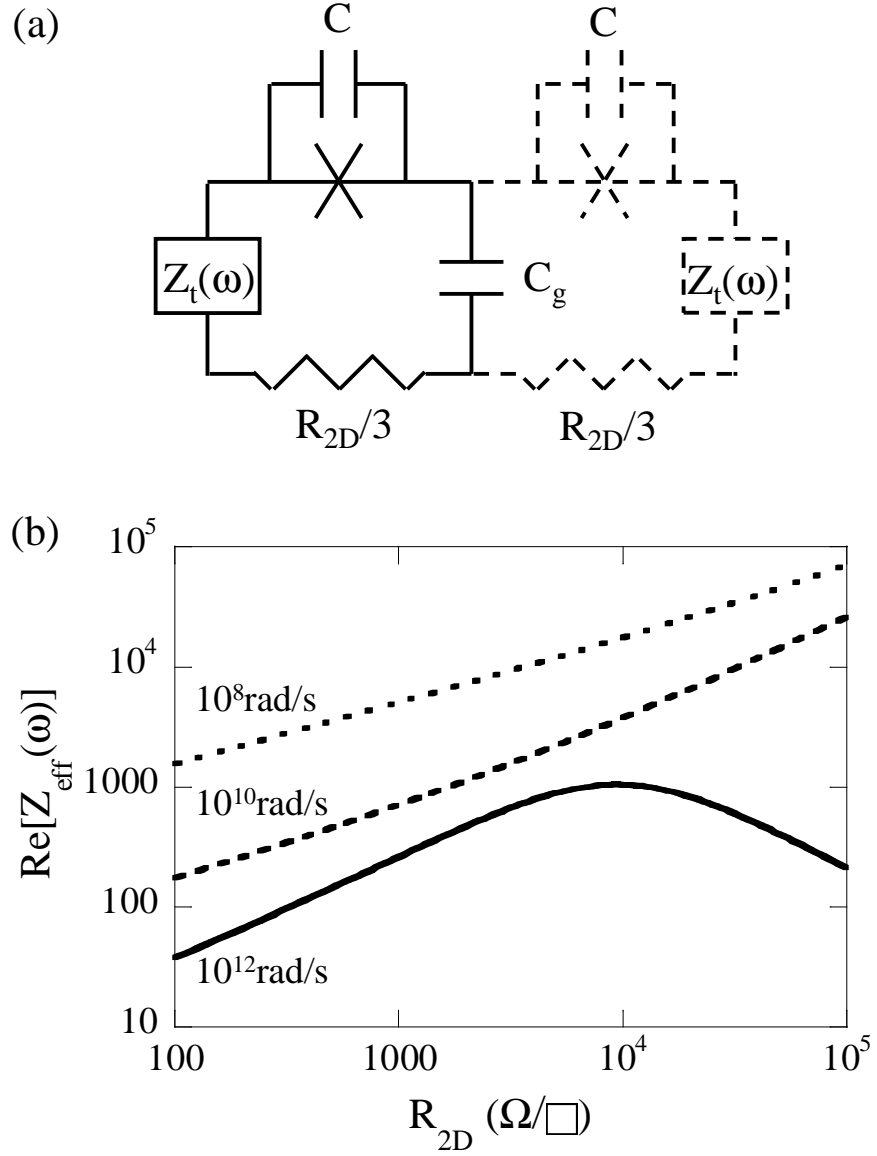


Figure 3.9: (a) Condensed circuit diagram of the sSET. To calculate the effective impedance across the left junction, $Z_{eff}(\omega)$, the right half of the circuit can be neglected. (b) The real part of the effective impedance across one junction as a function of 2DEG resistance.

the left junction. Therefore the effective impedance across one junction is simply

$$Z_{eff}(\omega) = \frac{R_{2D}/3 + Z_t(\omega) + 1/i\omega C_g}{1 + C/C_g + i\omega C [R_{2D}/3 + Z_t(\omega)]}. \quad (3.7)$$

The real part of this expression can vary non-monotonically with 2DEG resistance. As seen in Figure 3.9(b), for the frequencies of interest and for our range of 2DEG resistances, 160-600 Ω/\square , the real part of the impedance monotonically increases with increasing 2DEG resistance.

3.3 Measurement techniques

To observe the quantum mechanical nature of the sSET device, it is necessary to cool the device using a dilution refrigerator. We used an Oxford Model 75 dilution unit run with a homemade circulation system that was assembled by former members of the group [28]. The unit includes a 0.4 T magnet attached to the outside of the vacuum can. A RuO₂ thermometer measures the temperature of the sample. A “Rochlin bridge” measures the resistance of the thermometer and can also provide feedback to a metal film resistor on the mixing chamber to control the temperature of the sample.

Cooling the sample prevents noise in the sample from interfering with the sSET dynamics, but does not prevent noise from equipment at higher temperatures from propagating to the sample. Extensive filtering at several temperature stages is required to prevent this out of equilibrium noise from affecting the transport properties of the sSET. Vion *et al.* have calculated the filtering required to prevent high-temperature noise from overwhelming the intrinsic tunneling rate of Coulomb blockade systems [29]. For a sample temperature of 20 mK, over 200 dB of attenuation is needed.

To provide this attenuation we built high-frequency copper-powder filters based on a design previously developed in the Clarke group [7]. We formed small diameter rods composed of a mixture of stycast and oxidized copper powder (grain size $\approx 30 \mu\text{m}$) around which we wound 300 turn solenoids of manganin wire. These solenoids were sealed in copper tubes with stycast. The copper grains in these filters have a large effective skin area, and eddy current heating greatly attenuates noise at high frequencies. A single filter provided up to 80 dB of attenuation at frequencies above 800 MHz.

Figure 3.10 depicts the experimental configuration used to measure the zero-bias conductance G_0 of the sSET. Each lead was filtered by an LC π filter at room temperature, an RC π filter and a Cu powder filter at 4.2 K, and four Cu powder filters providing greater than 200 dB of attenuation at the sample temperature. To measure G_0 , a four-terminal lock-in technique was used. Typically we applied a 9.19 Hz voltage signal to the primary coil of a transformer. A large bias resistor on the secondary converted the signal to a current bias of typically 0.34 nA rms. The voltage was measured from a separate set of leads. The grounding of the circuit could be adjusted to decrease the common-mode signal to the amplifier. Data were typically acquired over several hours as the voltage on the gate was slowly swept.

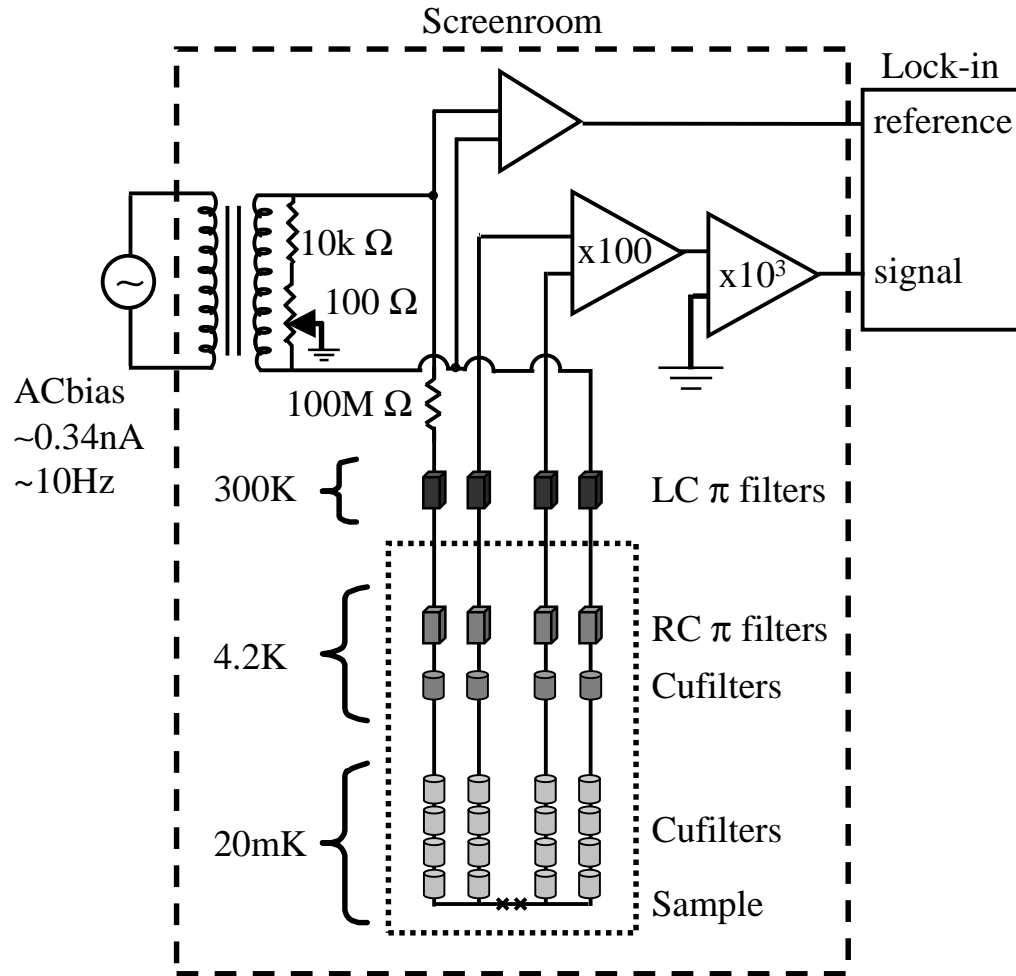


Figure 3.10: Experimental configuration to measure the zero-bias conductance of the sSET

Chapter 4

Experimental Results

4.1 Qualitative observations

Figure 4.1 shows the current voltage characteristic of the sSET at 40 mK with no applied gate or back-gate voltage. The current-voltage curve is hysteretic and low resistance, supercurrent-like behavior can be observed at zero voltage. As current is increased, the voltage switches out to $2\Delta/e$ and then to $4\Delta/e$. The switching current at zero voltage is about 1.5 nA which is approximately 10% of the critical current predicted by Eq. 1.7.

Figure 4.2 plots the zero-bias conductance versus gate voltage at several different temperatures with no applied back-gate voltage. As the temperature of the device increases, the zero-bias conductance decreases. In general, the amplitude of the conductance oscillations also decreases with increasing temperatures although there is a surprising lack of oscillations at 100 mK. Figure 4.3 plots the zero-bias conductance versus gate voltage at 18.7 mK for two different back-gate voltages. The zero-bias conductance decreases as

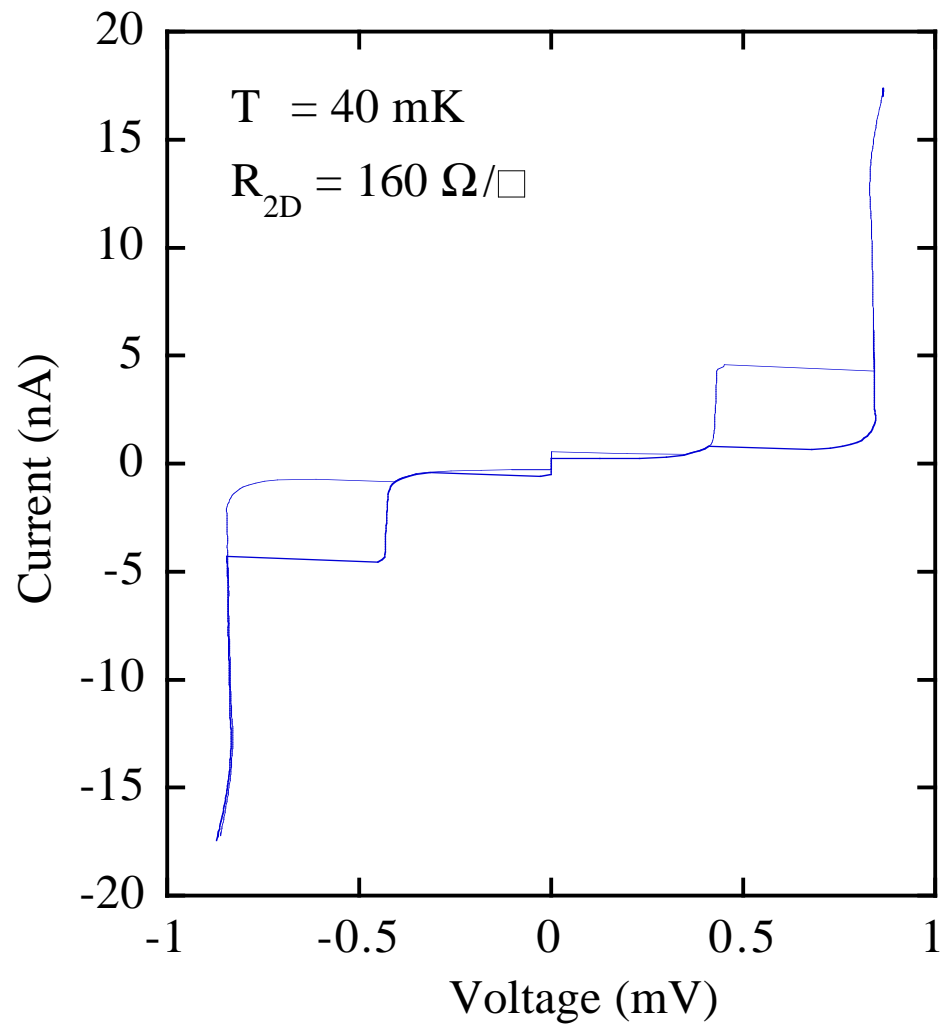


Figure 4.1: Current-voltage characteristic of the sSET

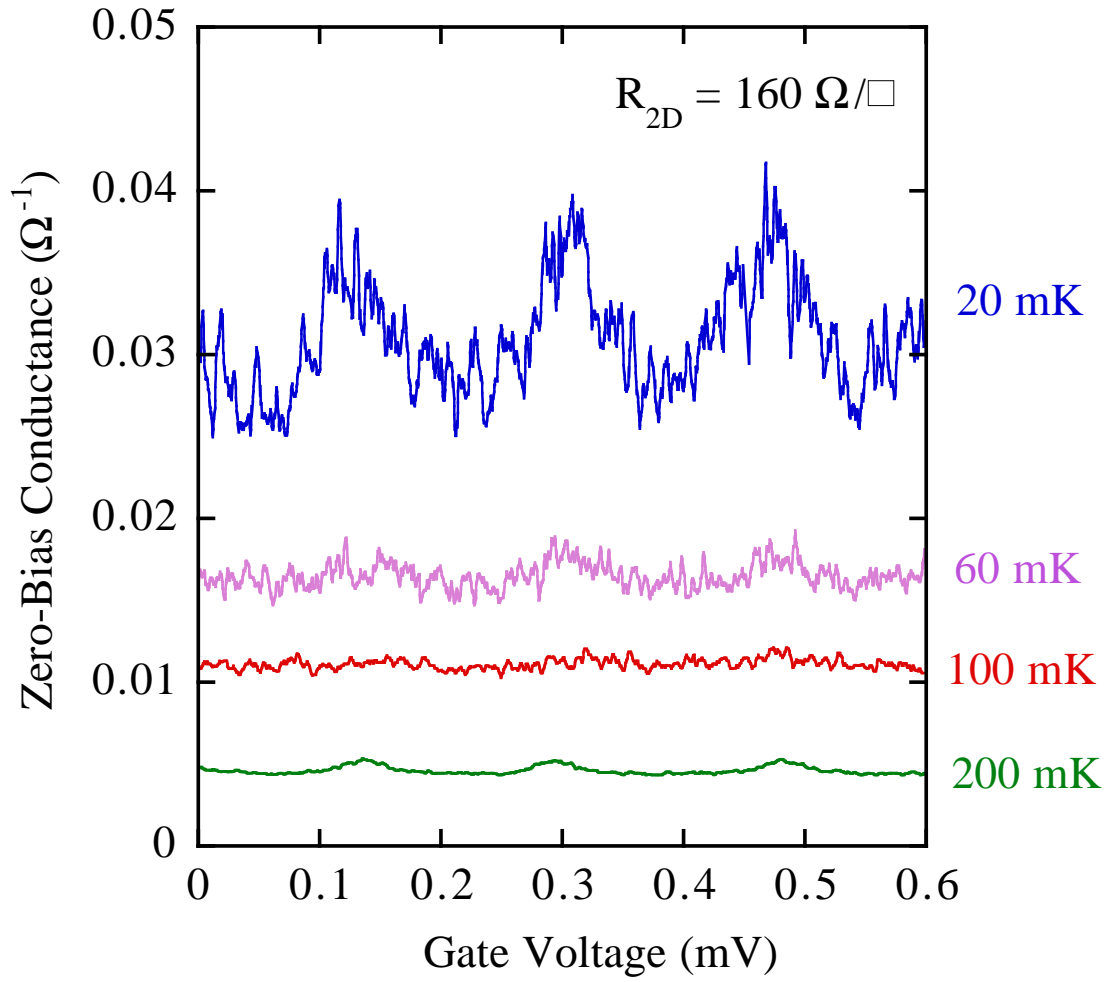


Figure 4.2: Zero-bias conductance as a function of gate voltage at four different temperatures

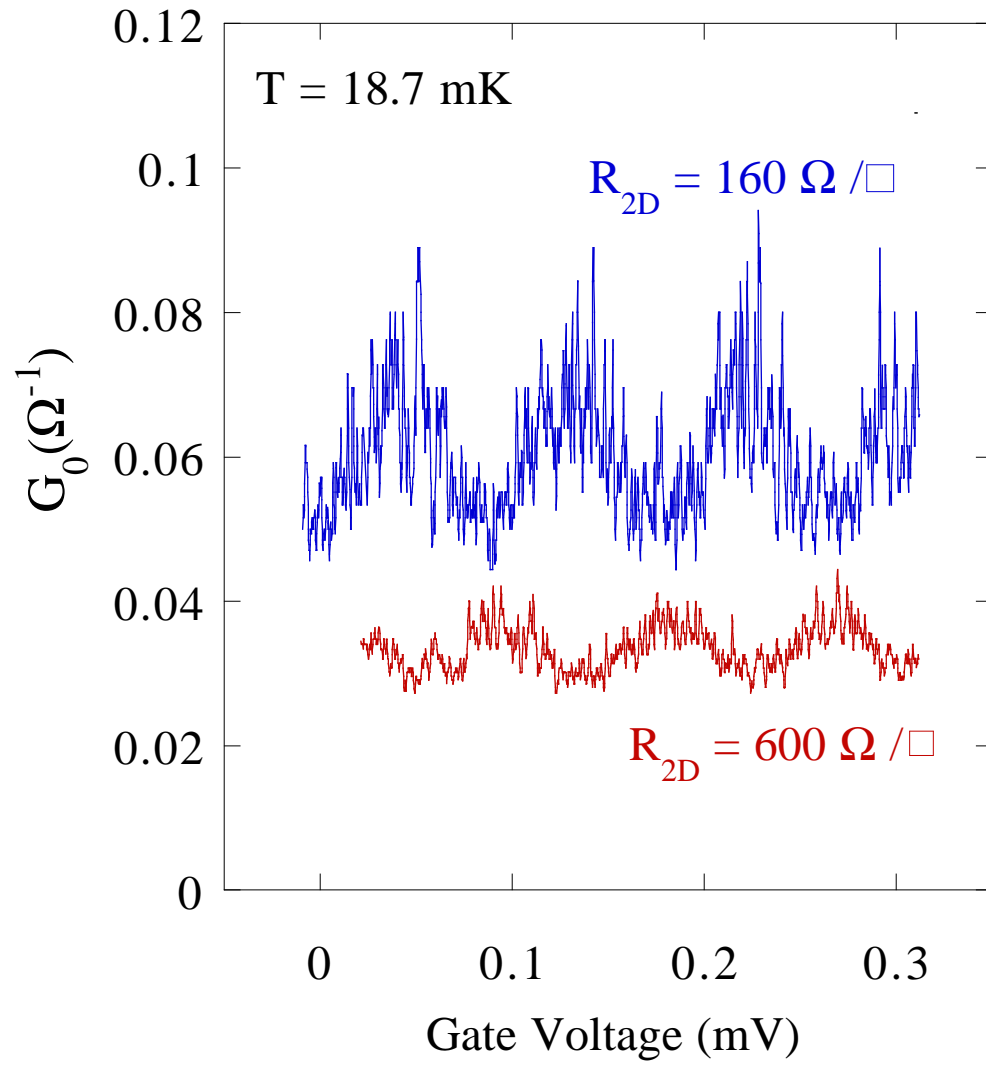


Figure 4.3: Zero-bias conductance as a function of gate voltage for two different values of 2DEG resistance

the 2DEG resistance increases. The oscillation amplitude also decreases with increasing 2DEG resistance. The oscillation of the zero-bias conductance in both of these figures has a period of $1e$ indicating that there most likely is poisoning due to defect states in the material. Unfortunately, this poisoning may partially suppress the Coulomb blockade features of the device. To maximize Coulomb blockade effects on the sSET, we focused our attention on the minimum zero-bias conductance as a function of gate voltage, G_0^{min} , which corresponds to the maximum charging barrier for tunneling between charge states.

Figure 4.4 plots the temperature dependence of the minimum zero-bias conductance for two different values of 2DEG resistance. For both values, the minimum zero-bias conductance decreases monotonically with increasing temperature. At each temperature, the minimum zero-bias conductance is greater for the smaller 2DEG resistance. Figure 4.5 plots the dependence of the minimum zero-bias conductance on 2DEG resistance at 5 different temperatures. At each temperature, the minimum zero-bias conductance decreases with increasing 2DEG resistance. The effect of 2DEG resistance grows weaker with increasing temperature. For each value of 2DEG resistance, the minimum zero-bias conductance increases with decreasing temperature.

4.2 Comparison with theoretical calculations

Before comparing these results with calculations based on the Caldeira-Leggett theory, we first verified that the large back-gate voltages used to change the 2DEG resistance do not simultaneously change the capacitance of the island. To do this we accurately measured C_g with the minimum and the maximum back-gate voltages applied. As

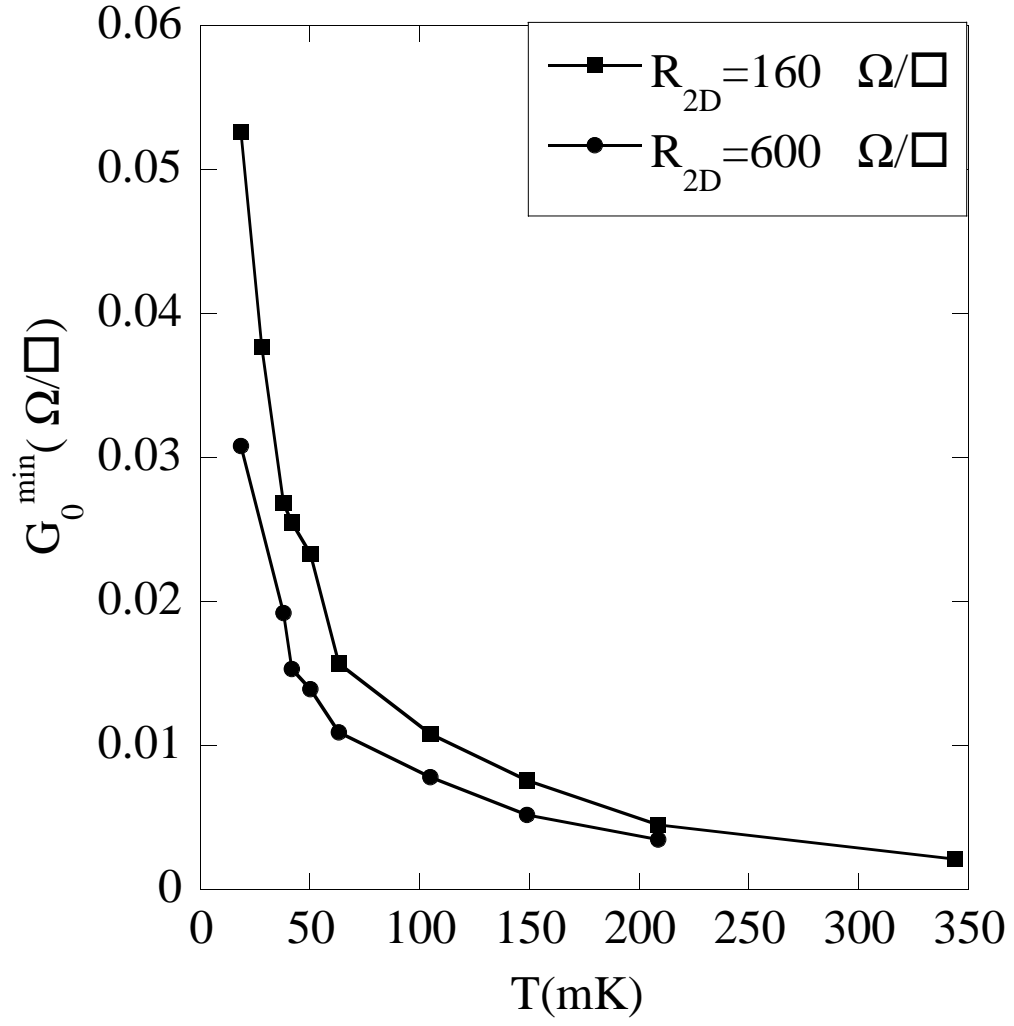


Figure 4.4: Minimum zero-bias conductance versus temperature for different values of 2DEG resistance

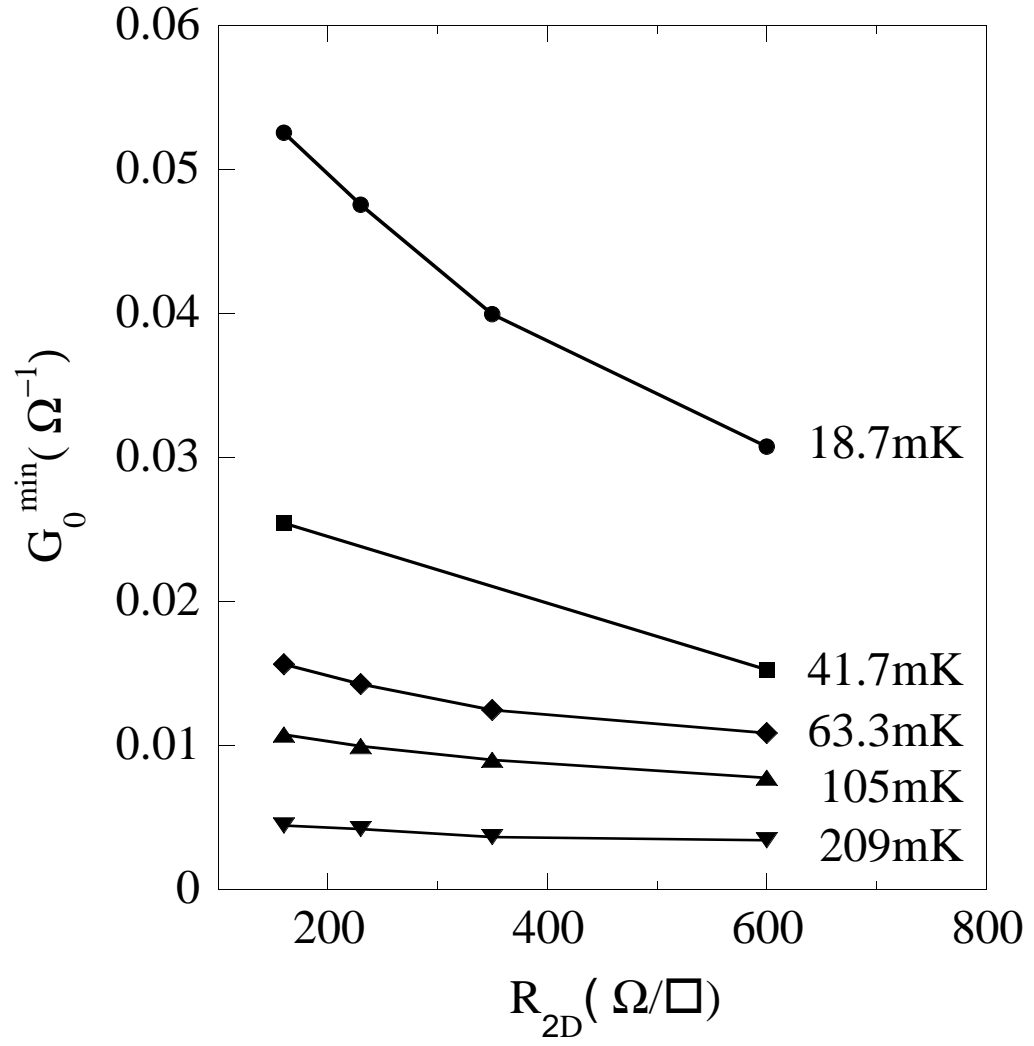
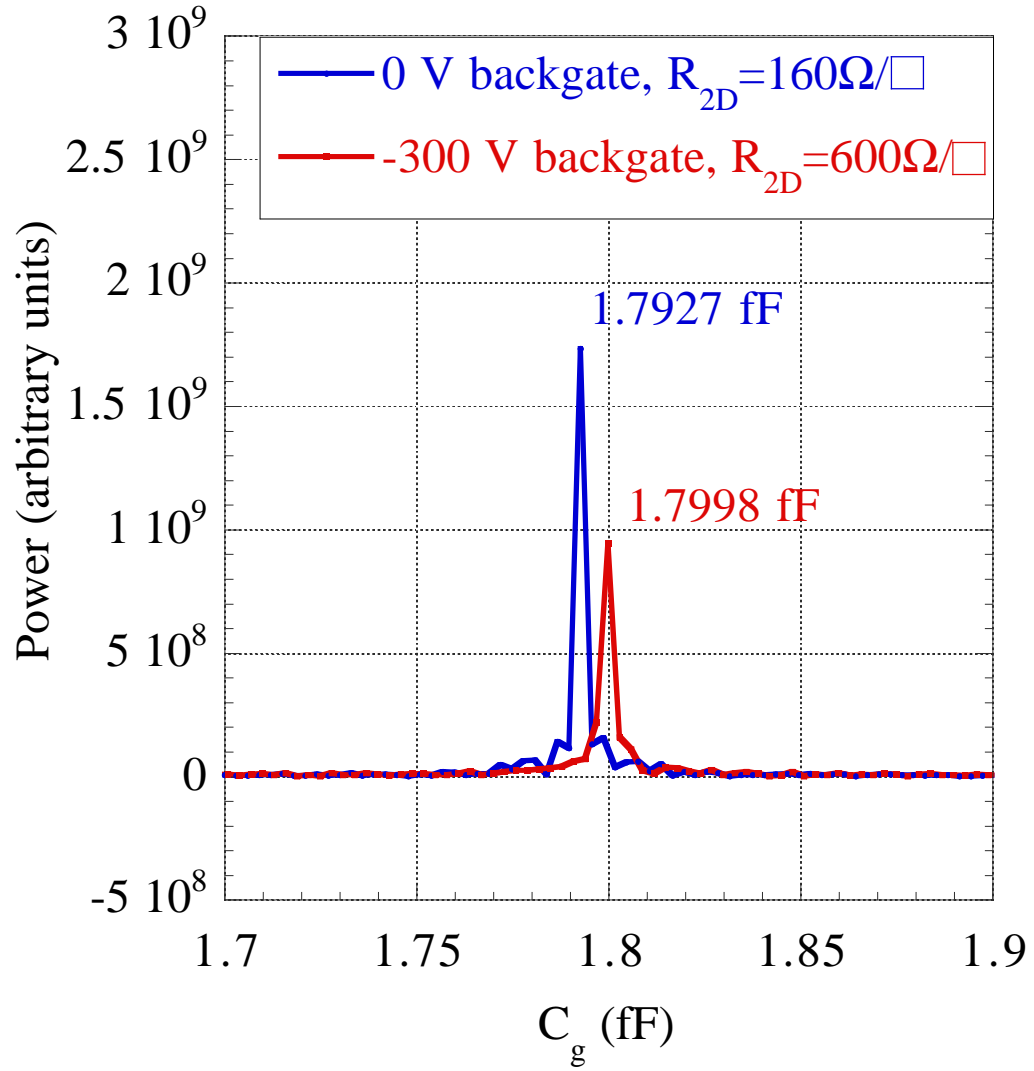


Figure 4.5: Minimum zero-bias conductance versus 2DEG resistance at different temperatures

mentioned in the previous chapter, C_g is measured by determining the periodicity of the zero-bias conductance as a function of gate voltage with the aluminum driven normal. Figure 4.6 plots the power spectrum for approximately 1000 oscillations of the conductance with 0 V and -300 V applied to the back gate. The gate capacitance corresponds to the peaks in the power spectrum. The percent change of the gate capacitance from maximum to minimum back-gate voltage was 0.4 % as compared to a 375 % change in the 2DEG resistance. This confirmed that C_g did not change significantly during the experiment.

The ability to vary the amount of dissipation in the sample *in situ* allows us to make quantitative comparisons with theoretical predictions on the effect of dissipation. For the sSET, F. K. Wilhelm, G. Schön and G. T. Zimanyi predicted the functional dependence of the conductance on temperature and dissipation due to incoherent Cooper pair tunneling to second order in a perturbative expansion in $E_J/4E_C$ [30, 31]. An outline of such a calculation to first order is described in the Appendix. Wilhelm *et al.* used two different models for the environment. The first model represented the leads of the sSET as large capacitors to the ground plane. The second model represented the leads of the sSET as lossy transmission lines. In the zero-bias, linear-conductance limit, Wilhelm *et al.* derived a simple power law dependence of the conductance on temperature and on the environmental conductance, $g \equiv 3R_K/4R_{2D}$ where $R_K \approx 25.8 \text{ k}\Omega$ is the resistance quantum. The parameter g is inversely proportional to the 2DEG sheet resistance and represents the effect of environmental dissipation. For the lumped circuit model, Wilhelm *et al.* predicted that the minimum zero-bias conductance scales as g/T^2 . For the transmission line model, they calculated a dependence of $g^{1/3}/T^{5/3}$.



Percent Change in C_g = 0.40%

Figure 4.6: Determining the effect of the back-gate voltage on the gate capacitance. Power spectrum of the zero-bias conductance as a function of gate voltage. Peaks correspond to the gate capacitance C_g .

Figure 4.7 plots G_0^{min} versus temperature on a log-log plot for the two extreme values of g . The data appear to follow a power law relationship with temperature for temperatures below 100 mK. For each value of g the data below 100 mK were fit to the model $G_0 \propto T^{-\alpha}$. The inset to Fig. 4.7 displays the derived values of α . The values of α appear to increase slightly with increasing g with an average value for α of approximately 0.9. Figure 4.8 plots G_0^{min} versus g on a log-log plot for five different temperatures. The data follow a weak power law dependence on g . At each temperature, we fit the data to the model $G_0 \propto g^\beta$. The inset to Fig. 4.8 displays the values of β at each temperature. The values of β decrease from 0.4 to 0.2 for increasing temperature.

In the above discussion, the observed temperature and dissipation dependence of the minimum zero-bias conductance agrees only roughly with the predictions of Wilhelm *et al.* Below 100 mK, the zero-bias conductance does follow a power law dependence on the temperature for fixed values of the environmental dissipation. The zero-bias conductance also follows a power law dependence on the environmental conductance for fixed values of temperature. However, the average measured temperature exponent, $\alpha \approx 0.9$, does not agree with either the prediction of 2 from the lumped-circuit model or the prediction of $5/3$ from the transmission line model. The measured values of the dissipation exponent, $\beta \approx 0.2 - 0.4$, do lie very close to the prediction of $1/3$ from the transmission line model. Moreover, the temperature dependence of β and the dissipation dependence of α indicate that the observed temperature and dissipation dependence of the minimum zero-bias conductance is not separable by a function of the form, $G_0^{min} \propto g^\beta/T^\alpha$, as predicted.

One possible reason that the theoretical predictions do not completely describe

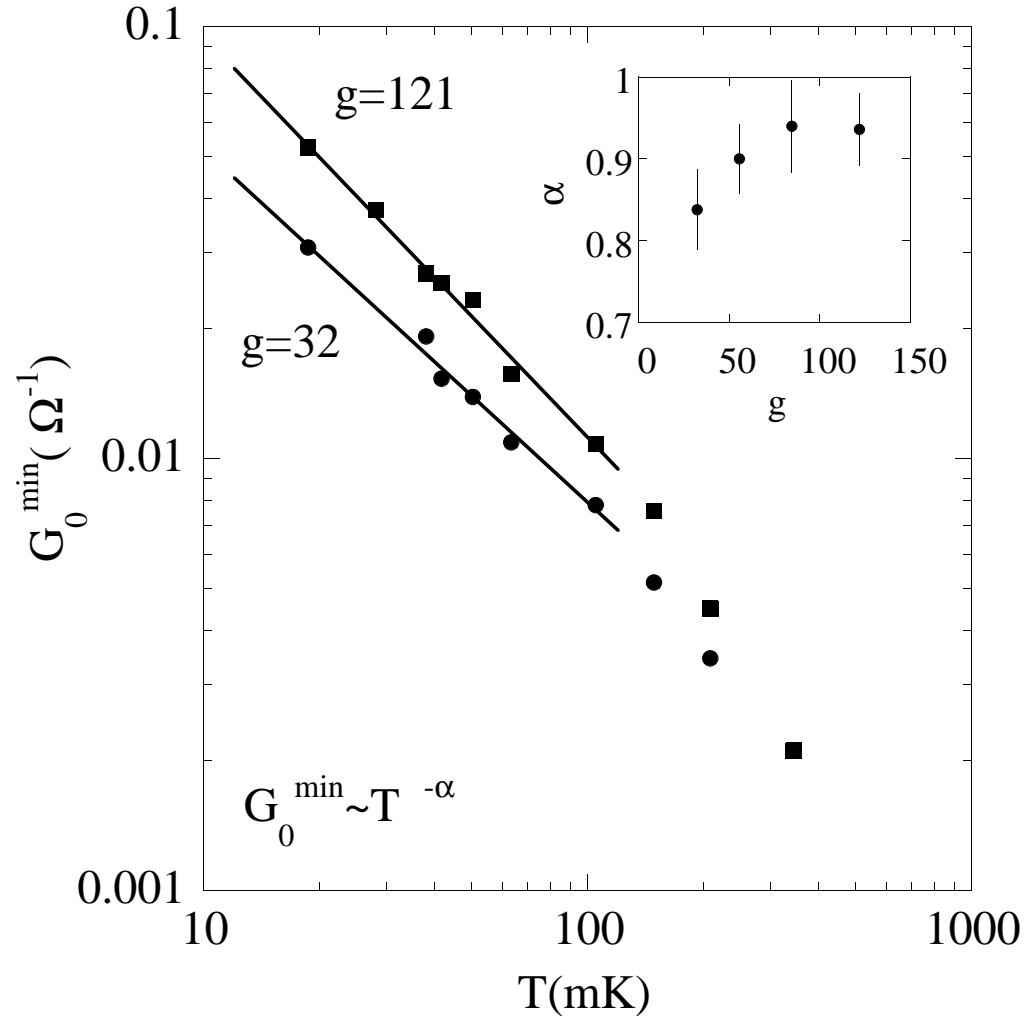


Figure 4.7: Log-log plot of minimum zero-bias conductance versus temperature

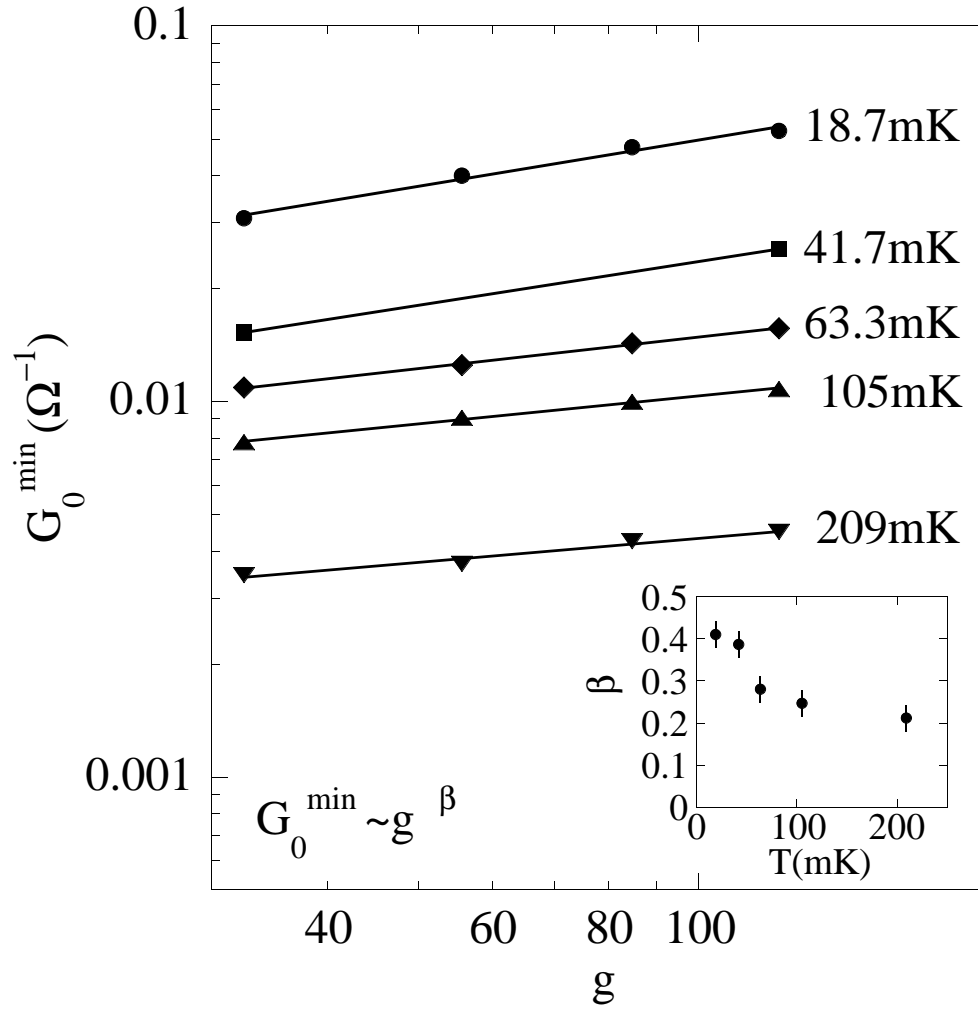


Figure 4.8: Log-log plot of minimum zero-bias conductance versus environmental conductance

the observed temperature and dissipation dependence of our data is that the Coulomb blockade effects of our sample may be suppressed by the quasiparticle poisoning effect discussed in the last section. The presence of quasiparticles may effectively decrease the ratio between the charging barrier, $4E_c/k_B \approx 1.5$ K for zero gate voltage without poisoning, and the Josephson energy, $E_J/k_B \approx 380$ mK. Pessimistically, quasiparticle poisoning could reduce the effective charging barrier to the single-electron charging barrier of $E_c/k_B \approx 360$ mK which is comparable to the Josephson energy. This effect might also explain the supercurrent-like behavior of the current-voltage characteristic.

Chapter 5

Conclusion

Using a superconducting single-electron transistor capacitively coupled to a dissipative ground plane, we have investigated the effect of temperature and environmental dissipation on the tunneling between charge states as measured by the zero-bias conductance of the sample. Temperatures from 20 - 350 mK were achieved by cooling the samples using a dilution refrigerator. The sheet resistance of the ground plane, which was composed of a two-dimensional electron gas, was varied from 160 - 600 Ω/\square by applying a large voltage to a metallic gate on the back of the substrate and depleting the 2DEG. We found that the minimum zero-bias conductance of the sSET decreased monotonically for increasing temperature. The minimum zero-bias conductance also decreased monotonically for increasing 2DEG resistance.

We compared these findings to calculations of the incoherent Cooper pair tunneling to second order in perturbation theory. The effects of the dissipative environment were incorporated using the Caldeira-Leggett technique. We did not find quantitative

agreement with the theoretical predictions. One possible reason for the differences in observed and predicted behavior may be the suppression of Coulomb blockade effects due to quasiparticle spoiling in the sample. It is possible that higher order terms in the perturbative expansion would account for some of these differences. It is also possible to fabricate samples with normal metal attached to the superconducting leads close to the Josephson junctions. The normal metal acts as a trap for stray quasiparticles, reducing the poisoning effect. With such a sample, it may be possible to observe tunneling between charge states in a sSET in good agreement with theoretical predictions.

Part II

MgB₂ Point-Contact Junctions and SQUIDs

Chapter 6

Introduction

In 2001 Nagamatsu *et al.* announced the discovery of superconductivity in magnesium diboride, MgB_2 [32]. To date, the T_c of this material, 39 K, is the highest known critical temperature for a non-copper-oxide material. This discovery greatly excited the scientific community and inspired a flurry of experiments on MgB_2 to determine the mechanism for superconductivity. One key component to analyze was the temperature and momentum vector, \vec{k} , dependence of the superconducting gap. Several experiments on tunneling between normal metals and samples of MgB_2 were performed to try to determine the answer to this question, and a wide variety of results were obtained. Scanning tunneling microscopy experiments yielded estimated superconducting gap values from 2 meV to 7 meV [33, 34, 35]. Point-contact tunneling experiments between gold tips and MgB_2 samples estimated superconducting gap values from 3 meV to 4.5 meV [36, 37]. Adding to the mystery, some tunneling experiments indicated the existence of two superconducting gaps [38, 39].

Besides the intense theoretical interest, researchers were also interested in the practical applications for MgB_2 . Due to the high critical temperature of MgB_2 , wires and devices made from this material may be cooled to operational temperatures using closed-cycle cryocoolers, greatly decreasing the cost of operation compared with that of low- T_c materials. In addition, Mg and B are abundant and inexpensive materials. Potential beneficiaries for this improved technology include Josephson junction devices. Early in 2001, several researchers performed preliminary experiments demonstrating the Josephson effect in MgB_2 . Gonnelli *et al.* used MgB_2 break junctions to observe a Josephson supercurrent [40]. Brinkman *et al.* used nanobridges patterned in thin films of MgB_2 to make the first superconducting quantum interference device (SQUID) from the material [41].

In the next three chapters, I will describe a series of experiments we performed on point-contact junctions between two MgB_2 pieces [42]. In these experiments, we were able to adjust the distance and thus the pressure between the two MgB_2 pieces and in this manner change the observed current-voltage behavior. With very light pressure applied between the MgB_2 contacts, noise suppressed the low Josephson supercurrent, and we observed the current due to quasiparticle tunneling in superconductor-insulator-superconductor (SIS) junctions. Using the quasiparticle tunneling data we estimated the value of the superconducting gap. By increasing the pressure of the contact, we observed current-voltage characteristics in good agreement with a superconductor-normal metal-superconductor (SNS) junction model. We also used MgB_2 pieces with two tips to form two SNS junctions in parallel creating simple SQUIDs. Using these SQUIDs we performed the first noise measurements on MgB_2 devices.

Chapter 7

Experimental Methods

The MgB_2 samples were prepared from flakes of material provided by D. G. Hinks and G. W. Crabtree of Argonne National Laboratory. Compact samples of MgB_2 were formed from high-purity amorphous B powder and Mg metal. The B powder was pressed into pellets under 6 kbar pressure. These free standing pellets were allowed to react with Mg vapor at 850°C for 2 hours in a BN container under 50 bar of Ar. During the diffusion reaction the pellets broke up into irregularly shaped pieces several millimeters on a side and about 0.5 mm thick. The samples had a typical T_c of 39 K.

To produce junctions with variable characteristics, we used a simple point-contact technique. Two pieces of MgB_2 were prepared. One piece, the base, was mounted rigidly to the probe such that the flat surface of the flake was perpendicular to the vertical axis of the probe. For another piece, one or two tips were formed at the edge of the flake. The tip was mounted to a rod whose vertical distance from the base surface could be adjusted *in situ* by a screw that could be turned from the top of the probe. Contact was formed

by moving the tip close to the base. By adjusting the pressure between the two pieces, junctions with different characteristics could be formed. To make electrical contact to the MgB_2 samples, two gold wires were silver pasted to the tip and to the base sample. Four-terminal voltage versus current measurements were acquired. A high-permeability shield was mounted around the sample to screen external magnetic fields.

To cool the samples to 4.2 K, the probe was submerged in a dewar with liquid helium. To vary the temperature, the probe was lifted above the helium bath level. The sample was then vapor cooled to temperatures above 4.2 K. Increasing the distance of the sample from the bath level increased the temperature. To measure the temperature of the He vapor and thus the approximate temperature of the sample, a calibrated Allen-Bradley resistor was mounted close to the sample and at the same vertical height along the probe. The resistance of the thermometer was measured using a four-wire measurement with 10 μA of bias current. After moving the sample to different heights above the bath, we typically waited several minutes for the temperature to become stable.

To irradiate the sample with radio-frequency power, an antenna was placed close to the sample. To apply magnetic fields, two coils were mounted, both centered around the sample area. One large coil was calibrated by applying an oscillating current to the coil and directly measuring the magnetic field at the center using a flux gate magnetometer. The small coil was calibrated against the large coil by comparing the relative currents necessary to produce equal amounts of flux in our MgB_2 SQUID samples. The small coil was used to apply the magnetic field to the SQUID samples during data acquisition to decrease inductive pick up of the magnetic field in the voltage leads of the SQUID.

Chapter 8

Estimating the Superconducting Gap in MgB₂ using SIS Tunnel Junctions

8.1 Quasiparticle tunneling

A direct method of measuring the superconducting gap of a material is to measure the quasiparticle tunneling current. The current due to single electrons tunneling across an insulating barrier is given by the expression

$$I = A|H_T|^2 \int_{-\infty}^{\infty} N_1(E)N_2(E + eV)[f(E) - f(E + eV)]dE \quad (8.1)$$

where A is a proportionality constant, $|H_T|^2$ is the tunneling matrix element, $N_1(E)$ and $N_2(E)$ are the respective density of single electron states for the two electrodes, E is the

energy referred to the Fermi energy, V is the applied voltage, and

$$f(E, T) = \frac{1}{e^{E/k_B T} + 1} \quad (8.2)$$

is the Fermi distribution function. If both electrodes are normal metals, for low voltages we can assume the density of states is approximately constant near the Fermi energy yielding

$$\begin{aligned} I_{NIN} &\approx A|H_T|^2 N_1(0)N_2(0) \int_{-\infty}^{\infty} [f(E) - f(E + eV)]dE \\ &= A|H_T|^2 N_1(0)N_2(0)eV \\ &\equiv G_{nn}V \end{aligned} \quad (8.3)$$

where G_{nn} is the normal state conductance of the tunnel junction. This predicted Ohmic behavior is experimentally observed.

To find the current for quasiparticle tunneling in SIS junctions using Eq. 8.1, it is necessary to find the superconducting density of quasiparticle states. In BCS theory, the energy of quasiparticle excitations $E_k(T)$ is related to the single electron states in a normal metal by the expression in Eq. 1.1 in Chapter 1. To calculate the superconducting density of quasiparticle states $N_s(E)$ in terms of the normal metal density of states $N_n(\epsilon)$, we can equate the number of quasiparticle states in a range dE , $N_s(E)dE$, with the number of single electron states in a range $d\epsilon$, $N_n(\epsilon)d\epsilon$. The resulting expression for the superconducting density of states is

$$\begin{aligned} N_s(E) &= \frac{N_n(\epsilon)E}{\sqrt{E_k^2 - \Delta^2(T)}} \\ &\approx \frac{N_n(0)E}{\sqrt{E_k^2 - \Delta^2(T)}} \end{aligned} \quad (8.4)$$

where again we can assume the normal metal density of states is fairly constant at the Fermi energy. The expression for the quasiparticle tunneling current is

$$I_{SIS} = \frac{G_{nn}}{e} \int_{-\infty}^{\infty} \frac{N_s(E)}{N_n(0)} \frac{N_s(E + eV)}{N_n(0)} [f(E) - f(E + eV)] dE. \quad (8.5)$$

This current is non-linear. At low temperatures, current does not flow until the bias voltage reaches approximately $2\Delta/e$. Therefore a rough estimate of the superconducting gap is obtained by looking for peaks in the conductance as a function of bias voltage. To more accurately estimate the superconducting gap, we can fit the measured current-voltage data to Eq. 8.5. To perform this fit to experimental data, it is necessary to modify the superconducting density of states to the expression

$$\frac{N_s(E)}{N_n(0)} = \text{Re} \left[\frac{E - i\Gamma}{\sqrt{(E - i\Gamma)^2 - \Delta^2(T)}} \right] \quad (8.6)$$

where Γ is a phenomenological gap smearing parameter that accounts for the finite lifetime of the quasiparticle states [43].

8.2 Suppression of the Josephson supercurrent

To measure the quasiparticle tunneling current in SIS junctions of fixed geometry, it is usually necessary to apply a magnetic field through the gap between the superconductors to suppress the supercurrent (see Sec. 4.05 of Ref. [12]). By adjusting the geometry of our junctions, we were able to form junctions with extremely small critical currents in which the supercurrents were suppressed by noise. In practice, the tip of the sample was moved away from the base so that no current was observed. We then slowly moved the tip toward the base until we observed a current between the two pieces with no apparent

supercurrent.

To confirm that the supercurrent was indeed suppressed by noise, we calculated the noise parameter

$$\Gamma_N = \frac{2ek_BT}{\hbar I_c}. \quad (8.7)$$

Studies analyzing the resistively and capacitively shunted junction model, Eq. 1.10, with the addition of thermal noise have found that the supercurrent is suppressed for $\Gamma_N \geq 0.4$ [44]. For our SIS junctions, the values of Γ_N were on the order of 0.5, making it likely that the Josephson effect was quenched by noise. Increasing the pressure between the MgB₂ pieces yielded hysteretic current-voltage characteristics with a supercurrent at zero-bias. The values of Γ_N for these junctions were < 0.01 .

8.3 Data and results

Figure 8.1 plots current and conductance, dI/dV , versus voltage for two SIS junctions at different temperatures. The data are fit using Eq. 8.5 and Eq. 8.6. The data fit well to a single gap model with gap smearing values of less than 5% of the superconducting gap. The conductance peak at zero-bias is due to the gap smearing effect. The two large symmetric conductance peaks roughly correspond to $2\Delta/e$. At larger voltages, there are no features indicating a second gap. Measuring several junctions at different temperatures, we derived the temperature dependence of the superconducting gap. Figure 8.2 shows the results of these measurements along with a fit to the universal temperature dependence of the gap in the weak coupling limit of the BCS theory. Using this fit we estimated $\Delta(0)$ of MgB₂ to be 2.02 ± 0.08 meV. The fitted T_c was 29 K. Although the data fit the universal

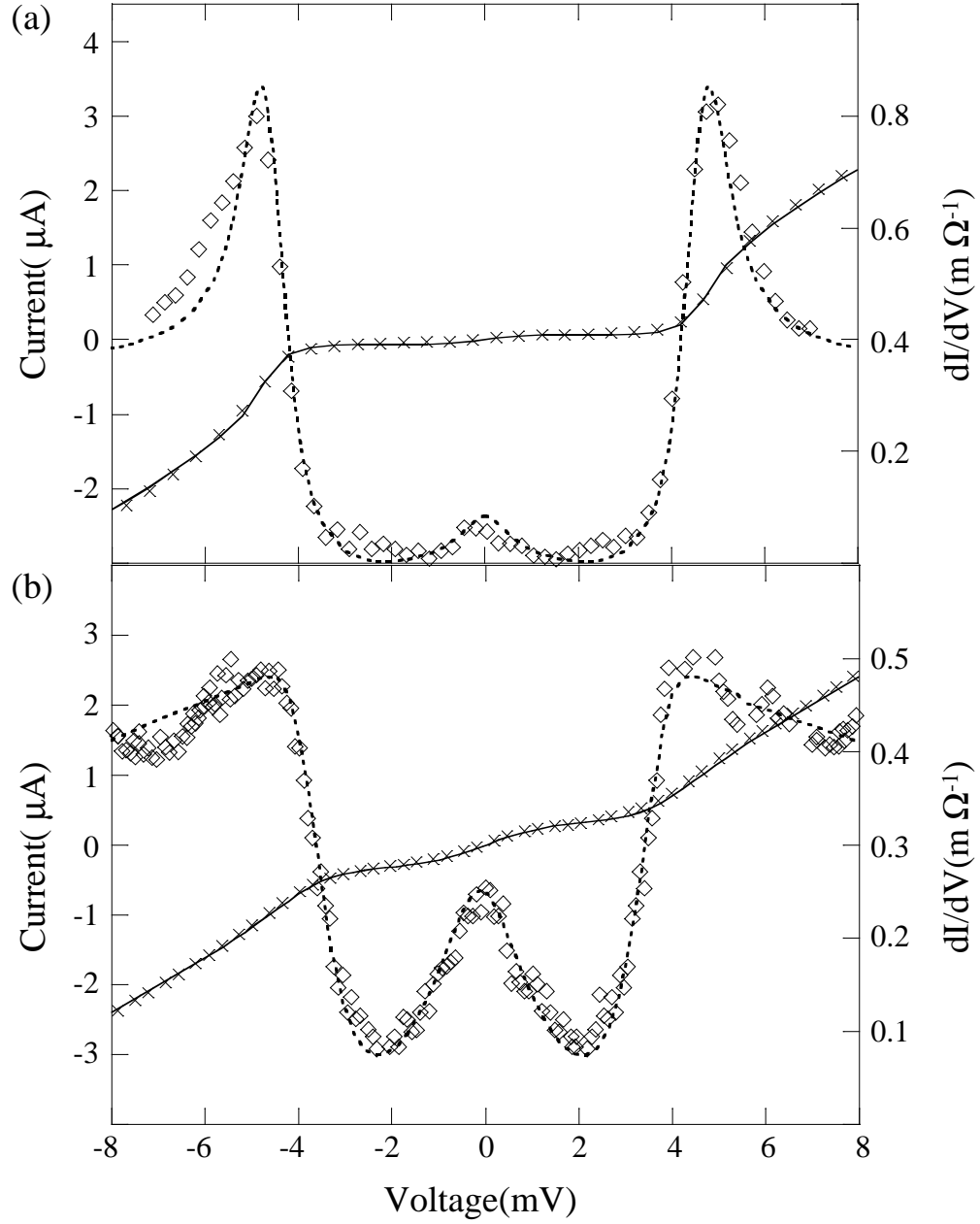


Figure 8.1: Quasiparticle current (crosses) and conductance dI/dV (diamonds) versus voltage for SIS-like junctions. Supercurrent is suppressed by noise. Fits to theory are shown in solid and dotted lines. (a) $T = 8.9$ K; $\Delta(0) = 2.06$ meV; and $\Gamma = 0.120$ meV. (b) $T = 16.4$ K; $\Delta(0) = 1.88$ meV; and $\Gamma = 0.047$ meV.

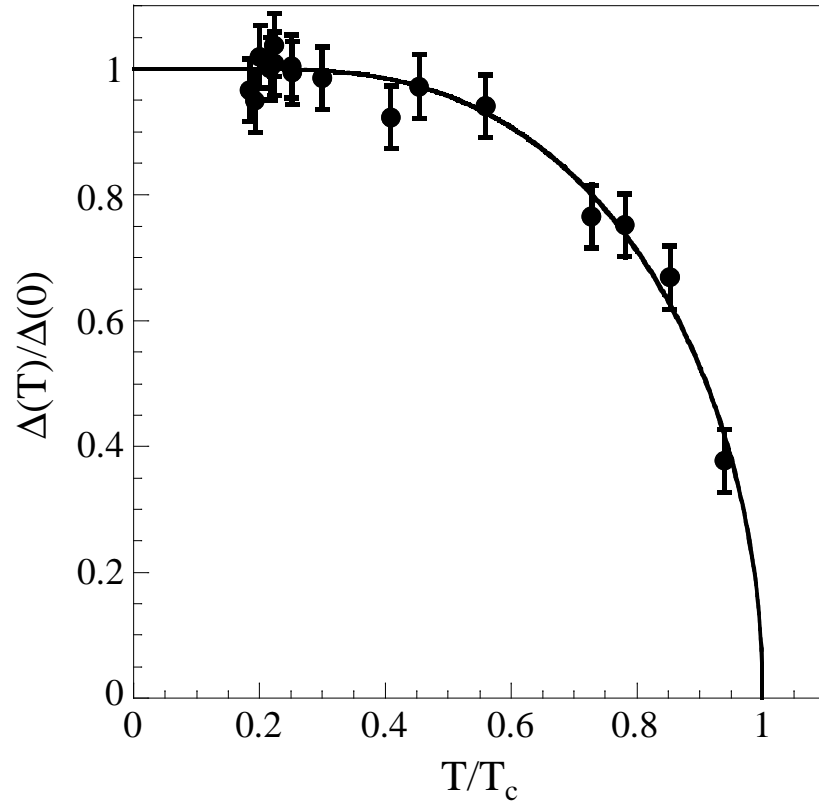


Figure 8.2: Superconducting gap $\Delta(T)$ as a function of temperature T . Data are fitted to the universal curve predicted by the BCS theory in the weak-coupling limit. The superconducting gap is scaled by the fit parameter $\Delta(0) = (2.02 \pm 0.08)$ meV, and the temperature is scaled by the fit parameter $T_c = 29$ K.

temperature dependence fairly well, the predicted $\Delta(0)$ and T_c do not match the expected weak-coupling BCS prediction in Eq. 1.2 in Chapter 1. Moreover, the predicted T_c was significantly lower than the experimentally observed value of 39 K.

Chapter 9

MgB₂ SNS Junctions and SQUIDs

9.1 SNS junctions

As described above, the initial contact between the MgB₂ tip and base produced SIS current-voltage behavior. Increasing the pressure between the two pieces produced hysteretic current-voltage curves with supercurrents at zero-bias. Further increases in pressure led to a third regime with large normal state resistances and non-hysteretic current-voltage characteristics. This current-voltage behavior resembles that of superconductor-normal metal-superconductor (SNS) junctions. The ability of point-contact junctions to produce SNS junction behavior has been documented using other low- T_c superconductors [45]. It has been suggested that these point contacts form nearly ideal microbridges of material that behave like normal metal barriers.

SNS junctions can be modeled using a limiting form of the RCSJ model described in Chapter 1. For these junctions, the resistance due to the single-electron current, R , can be quite low. In this case, the damping term in Eq. 1.10 can dominate over the capacitive

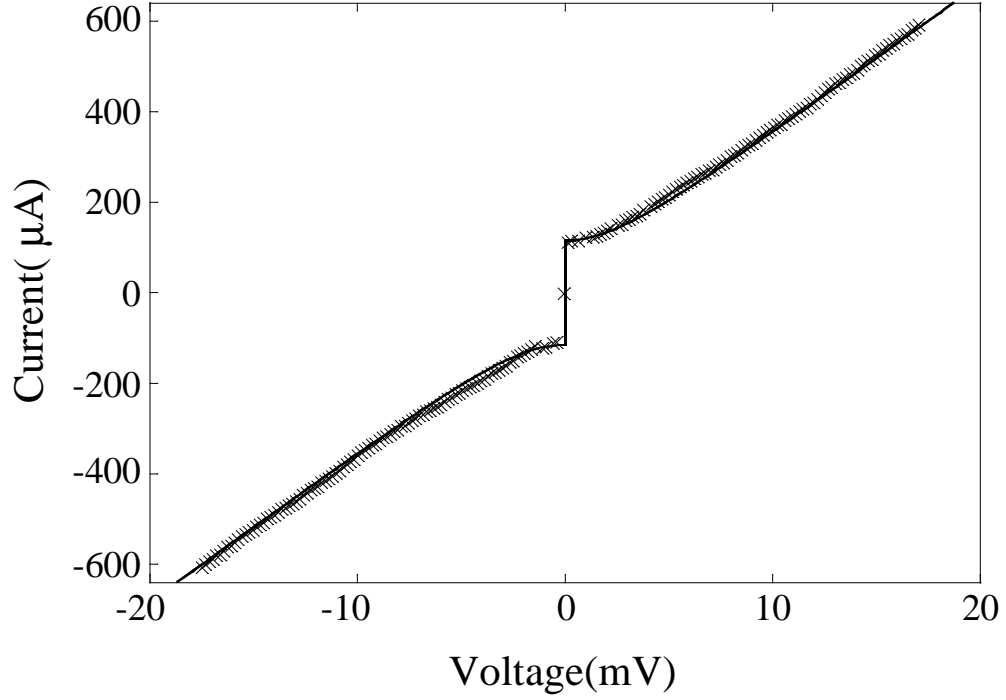


Figure 9.1: Current (crosses) versus voltage for a SNS-like junction at 5 K. The curve is fit to the noise-free resistively shunted junction model with fit parameters $I_c = 0.115$ mA and $R_s = 29.7 \Omega$.

term which can then be neglected. Thus, the model becomes simply a resistively shunted junction (RSJ) model. The equation of motion is now a first order differential equation. The time averaged voltage is a single-valued function of current given by

$$V = R\sqrt{I^2 - I_c^2} \quad \text{for } I > I_c. \quad (9.1)$$

Figure 9.1 depicts a typical current-voltage characteristic for one of our SNS junctions. The data are fit to Eq. 9.1. The noise parameter for this junction is $\Gamma_N = 0.0021$ which accounts for the good fit to the ideal, noise-free model.

9.2 RF-driven SNS junctions

By applying radio-frequency power to the system using an antenna placed close to the sample, we also demonstrated some of the high frequency Josephson effects in our junctions. If we assume an ideal voltage bias across the junction of

$$V = V_{dc} + V_{rf} \cos \omega_{rf} t, \quad (9.2)$$

we can derive the expression for the time dependent phase difference using the second Josephson relation, Eq. 1.4. Inserting this phase difference into the first Josephson relation, Eq. 1.3, yields an expression for the current

$$I_s = I_c \sum_m (-1)^m J_m(2eV_{rf}/\hbar\omega_{rf}) \sin [(2eV_{dc}/\hbar + m\omega_{rf})t + \phi_0] \quad (9.3)$$

where ϕ_0 is an integration constant and J_m are Bessel functions. The above equation predicts the existence of current steps, called Shapiro steps, at voltages

$$V_m = \frac{m\hbar\omega_{rf}}{2e} \quad (9.4)$$

of height

$$I_m = I_c J_m(2eV_{rf}/\hbar\omega_{rf}). \quad (9.5)$$

For SNS junctions, the rf power behaves more like a current source. Numerical calculations of the current source model also predict the existence of Shapiro steps. In this case, the step heights are modulated by varying the rf current but do not follow a Bessel-function dependence [45]. Figure 9.2(a) shows an example of Shapiro steps observed in our MgB₂ junctions, and Fig. 9.2(b) plots the step heights as a function of rf voltage. The step locations closely follow Eq. 9.4.

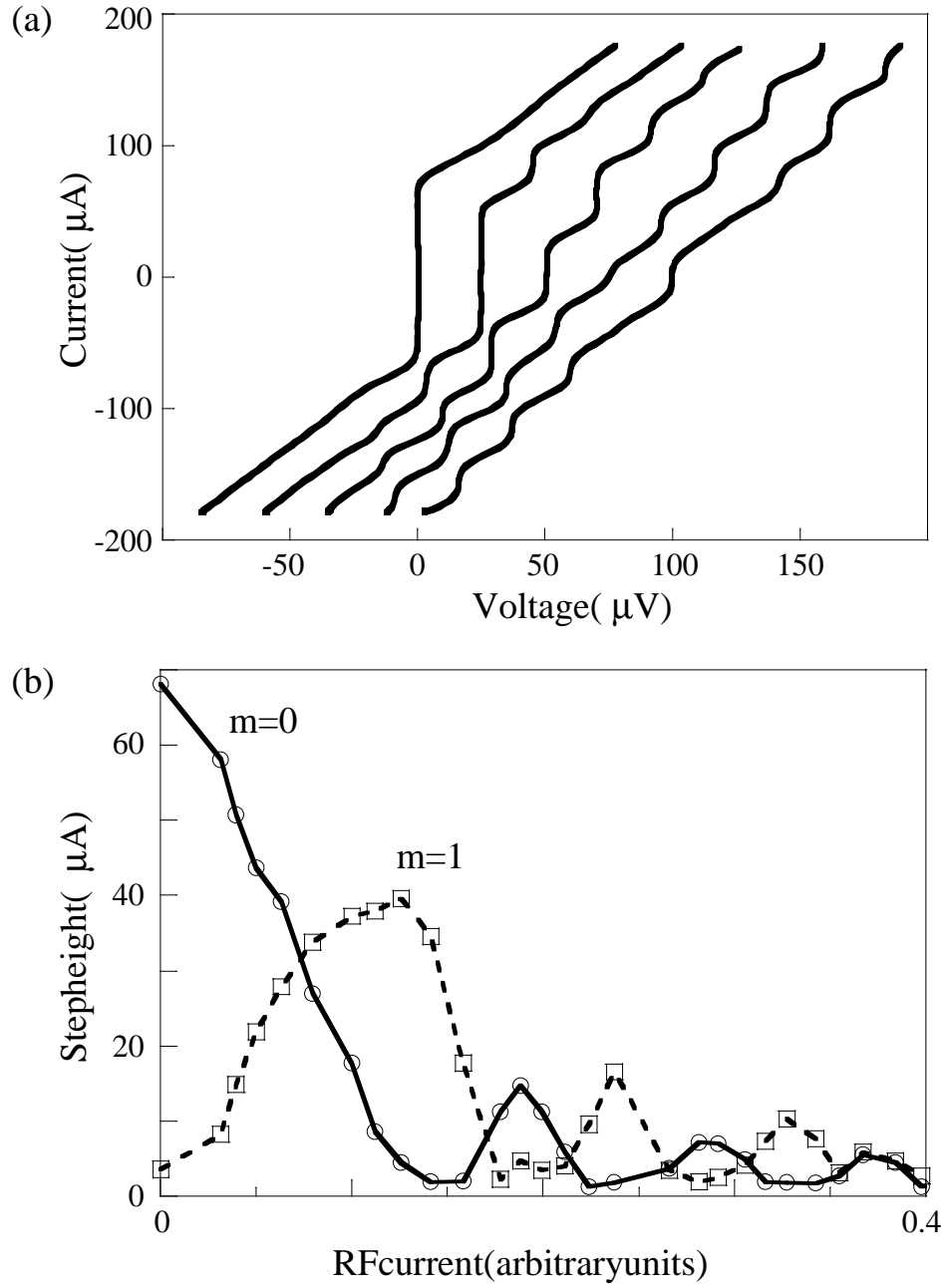


Figure 9.2: Shapiro steps in a SNS-like junction at 20 K. RF power is applied at frequency $f = 10$ GHz. (a) Current versus voltage for increasing rf power. Steps occur at voltages $m h f / 2e$ where m is an integer and $h f / 2e = 20.7 \mu\text{V}$. Curves are offset by $25 \mu\text{V}$ for clarity. (b) Step height for step $m = 0$ (circles connected by solid line) and $m = 1$ (squares connected by dashed line) as a function of rf current.

9.3 MgB₂ SQUIDS

As mentioned in Chapter 1, SQUIDS are currently the most sensitive detectors of magnetic flux. A dc SQUID consists of two non-hysteretic Josephson junctions in parallel as depicted in Fig. 9.3. At zero-voltage bias, the current through the SQUID is the sum of the supercurrents through each junction calculated using the phase difference across each junction and the first Josephson relation, Eq. 1.3. The phase differences across each junction are not completely independent. Rather they are linked by the relationship

$$\phi_1 - \phi_2 = 2\pi\Phi/\Phi_0 \pmod{2\pi} \quad (9.6)$$

where Φ is the magnetic flux through the SQUID loop and $\Phi_0 = h/2e \approx 2 \times 10^{-15} \text{ T m}^2$ is the flux quantum. Thus the maximum supercurrent through the SQUID, I_{sm} , depends on the magnetic flux through the SQUID as

$$I_{sm} = 2I_c |\cos(\pi\Phi/\Phi_0)| \quad (9.7)$$

where each junction is assumed to have the same I_c . Therefore the current-voltage characteristic of a SQUID is a periodic function of magnetic flux through the SQUID with period Φ_0 . According to Eq. 9.7, the maximum supercurrent of $2I_c$ should be observed for integer values of magnetic flux through the SQUID while the supercurrent should be completely suppressed for half-integer values of magnetic flux. The self-inductance of the SQUID, however, produces screening currents that prevent the full suppression of the supercurrent for half-integer applied magnetic flux. If we bias the SQUID with a current above I_{sm} , the voltage across the SQUID modulates with the applied magnetic flux. In this manner the SQUID acts as a flux-to-voltage transducer.

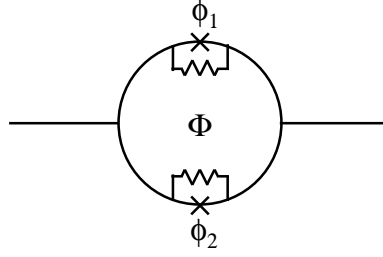


Figure 9.3: SQUID configuration

To make MgB_2 dc SQUIDS, we again used a point-contact technique. We replaced the single-tip MgB_2 pieces with double-tip pieces. The tip pieces were placed on the movable mount. The pressure between the tips and the base was increased until non-hysteretic SNS-like current-voltage characteristics were obtained. Figure 9.4(a) shows the current voltage characteristic for one such SQUID. By applying magnetic flux via the small coil centered about the sample, we modulated the flux through the SQUID. As can be seen, the current voltage characteristic can be modulated from a maximum supercurrent with an integer flux quantum through the SQUID to a minimum supercurrent with half integer flux quantum through the SQUID. If we bias the SQUID with a constant current, we can observe the associated modulation of the voltage across the SQUID as a function of applied flux seen in Fig. 9.4(b). The peak-to-peak voltage of the oscillations varies with the bias current. The maximum observed peak-to-peak voltage is $60 \mu\text{V}$. The oscillations are somewhat asymmetric, suggesting that the critical currents and resistances of the two junctions were not equal or the two junctions were asymmetrically located on the superconducting loop. At a bias current of $13.5 \mu\text{A}$, the average maximum transfer coefficient is $280 \mu\text{V}/\Phi_0$.

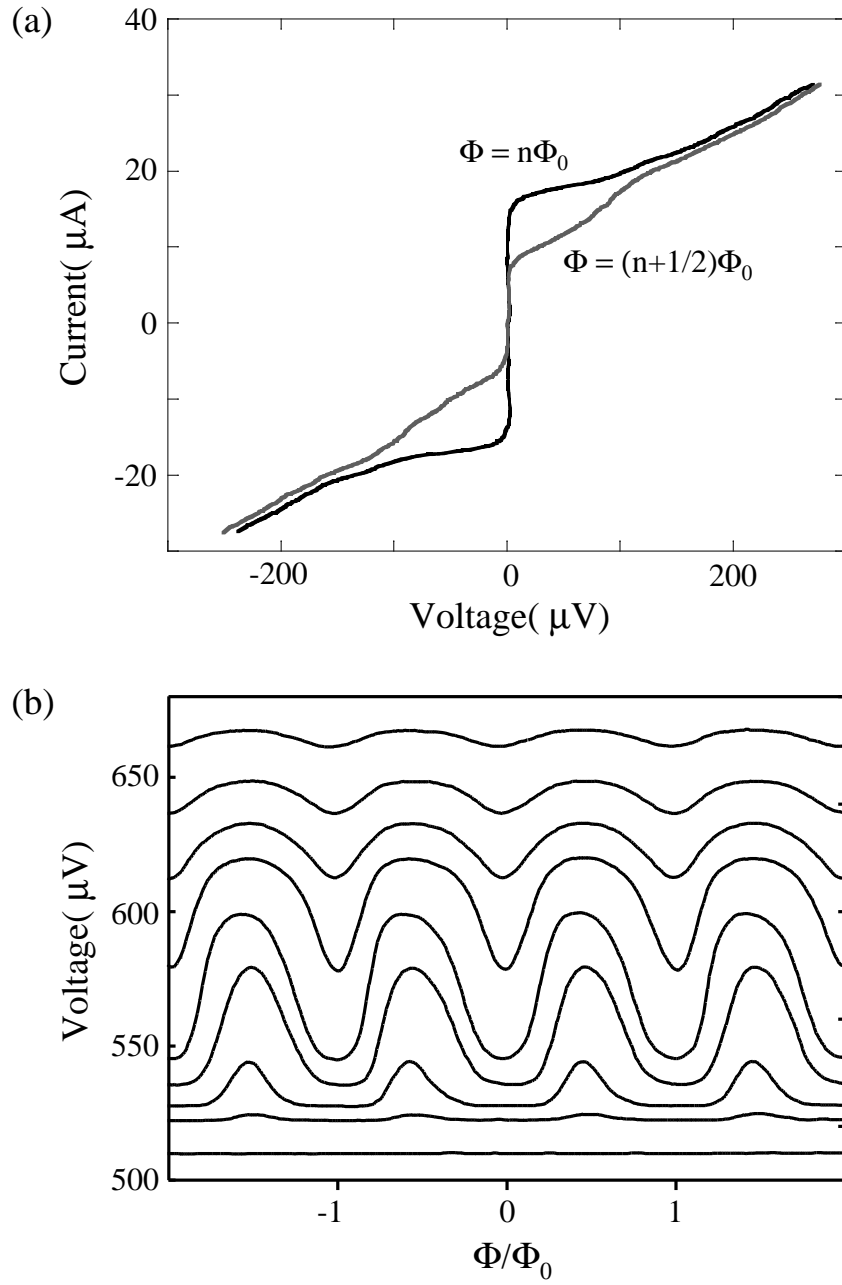


Figure 9.4: (a) Current versus voltage for a dc SQUID for integer n and half-integer $n+1/2$ applied flux quanta. (b) Voltage versus applied magnetic flux for bias currents of 0, 6.6, 8.0, 11.0, 13.5, 16.0, 17.0, 18.0, and 19.2 μA (from bottom to top).

9.4 Noise measurements

To measure the noise of our MgB_2 SQUIDs, we enclosed the samples in a high-permeability shield to screen the effect of external magnetic field noise. We also operated the devices using the standard SQUID read-out schemes described below.

As mentioned in the previous section, a current-biased SQUID acts as a flux-to-voltage transducer. The voltage, however, is a periodic function of the magnetic flux. To linearize the output of the SQUID, the SQUID is operated in a negative feedback loop called the flux-locked loop. Through a feedback coil inductively coupled to the SQUID, the feedback circuit applies a magnetic flux to the SQUID that cancels the magnetic flux signal. The current through the feedback coil is proportional to the magnetic flux signal and is read-out by the electronics.

A couple of features can be added to the feedback circuit described above to decrease the effect of low-frequency noise. One source of low-frequency $1/f$ noise is the amplifier used to measure the voltage across the SQUID. To reduce the effect of this noise, the voltage across the SQUID can be measured using the ac lock-in technique depicted in Figure 9.5. An oscillating current of frequency f_m is applied to the feedback coil to produce a modulating flux of peak-to-peak amplitude $\Phi_0/2$ in the SQUID. If there is no signal applied, the flux through the SQUID modulates about a minimum of the voltage-flux curve as depicted in Fig. 9.6(a). The resulting voltage across the SQUID is periodic with frequency $2f_m$. The lock-in amplifier which is referenced at f_m does not produce an output. If there is a quasi-static signal applied to the SQUID, the resulting voltage across the SQUID has some component at frequency f_m which does produce an output from the

as horizontal shifting of the voltage-flux curve. The f_m frequency component of the voltage across a SQUID with flux modulation (Fig. 9.6) is not effected by a quasi-static vertical shift of the voltage-flux curve. To reduce the effect of a quasi-static horizontal shift of the voltage-flux curve, a bias-reversal scheme is used. The bias of the SQUID is reversed while simultaneously $\Phi_0/2$ magnetic flux is applied to the SQUID. The net effect of these actions on the voltage-flux curve is to create the opposite quasi-static horizontal shift of equal magnitude. Periodically reversing the bias current with a frequency commensurate with the flux modulation frequency averages out the effect of the flux fluctuation. Low- T_c SQUIDS are often operated using a flux-locked loop with flux modulation. High- T_c SQUIDS have greater $1/f$ noise due to critical current flucutations and thus are often operated using bias reversal as well. However, high- T_c SQUIDS also suffer from $1/f$ noise due to the motion of trapped flux vortices in the superconducting film which is not alleviated by bias reversal. This has prevented high- T_c SQUIDS from attaining sensitivities at low frequencies comparable to the most sensitive low- T_c SQUIDS.

Figure 9.7 shows two noise spectra for two MgB_2 SQUIDS operated in a flux-locked loop with flux modulation. The left ordinate shows the magnetic flux noise and the right ordinate is scaled to show the magnetic field noise. The two are related by the effective area A_{eff} of the SQUID,

$$S_B^{1/2} = S_\Phi^{1/2}/A_{eff}. \quad (9.8)$$

The effective area of the SQUID samples were determined by measuring the magnetic field necessary to produce one flux quantum through the SQUID.

In Figure 9.7(a) we measured a SQUID with an effective area of 0.16 mm^2 . The

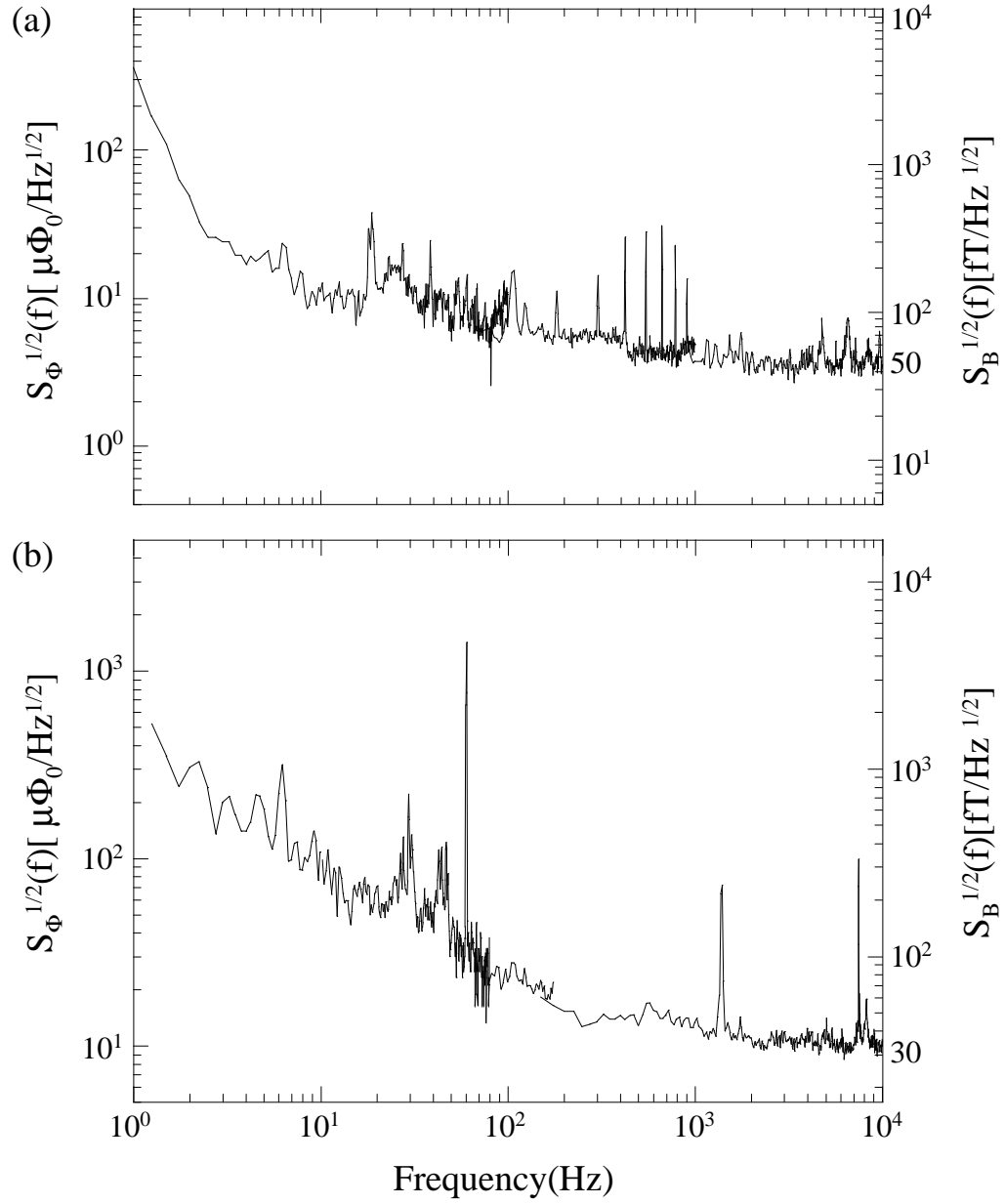


Figure 9.7: Noise spectra for two SQUIDs at 19 K. Left-hand ordinate shows magnetic flux noise, right-hand shows magnetic field noise. (a) Effective area of the SQUID is 0.16 mm^2 . White noise level is $4 \mu\Phi_0/\text{Hz}^{1/2}$ or $52 \text{ fT}/\text{Hz}^{1/2}$. (b) Effective area of the SQUID is 0.6 mm^2 . White noise level is $10 \mu\Phi_0/\text{Hz}^{1/2}$ or $35 \text{ fT}/\text{Hz}^{1/2}$.

white, or frequency-independent, noise extends down to frequencies of about 500 Hz. The white noise level is about $4 \mu\Phi_0/\text{Hz}^{1/2}$ or about $50 \text{ fT}/\text{Hz}^{1/2}$. As the frequency is lowered, the noise increases with a slope of roughly $-1/4$. The large low-frequency noise below 3 Hz is most likely due to external noise that is not fully attenuated by the shielding. The noise between 3 Hz and 500 Hz may be intrinsic or may be due to temperature fluctuations. In Figure 9.7(b) we measured a SQUID with an effective area of 0.60 mm^2 . The white noise of $10 \mu\Phi_0/\text{Hz}^{1/2}$ or about $35 \text{ fT}/\text{Hz}^{1/2}$ extends to about 1 kHz. The noise below 1 kHz is approximately $1/f$ in character. We also operated the SQUIDs using bias reversal with no change in the noise spectra.

The noise of the simple MgB_2 SQUIDs described above is comparable to the noise of state-of-the-art high- T_c SQUIDs. A recent review reports a best flux noise of $2.2 \mu\Phi_0/\text{Hz}^{1/2}$ and a best field noise of $10 \text{ fT}/\text{Hz}^{1/2}$ at 1 kHz for a single-layer YBCO high- T_c SQUID [46]. However, low- T_c devices made from niobium regularly achieve noise levels in the $\text{fT}/\text{Hz}^{1/2}$ range. Nonetheless, the noise measurements presented here from MgB_2 SQUIDs are a promising first step towards creating low-noise devices with high operational temperatures. Practical MgB_2 SQUIDs most likely will come in the form of thin-film devices, similar to those produced from niobium or YBCO.

Chapter 10

Conclusion

In the two years since we performed these experiments, a tremendous amount of research has been performed on MgB₂. As a result, the mechanism for superconductivity in this material is believed to be understood. The crystal structure of MgB₂ consists of alternating planes of Mg and B atoms. The bonds between the B atoms lying in one of these planes are sp^2 -hybridized σ bonds. The p orbitals of the B atoms form π bonds that connect adjacent planes. This structure produces two conduction bands: the σ band which is effectively two-dimensional and the π band which is three-dimensional. Both these bands contribute equally to the structure of the Fermi surface. Recent theoretical calculations have found that an electron-phonon interaction in this material does yield a superconducting gap that varies significantly as a function of momentum vector \vec{k} . One such calculation found that $\Delta(\vec{k})$ separated into two groups: one group, Δ_σ , range from 6.4 - 7.2 meV and another group, Δ_π , ranged from 1.2 - 2.7 meV [47]. These calculations predict that both gaps exist out to the full critical temperature. Several experiments on

scanning tunneling microscopy on single crystal samples of MgB_2 have demonstrated that the superconducting gap is dependent on the orientation of \vec{k} [48, 49]. Measured values of the gap for \vec{k} parallel to the atomic planes, Δ_σ , vary from 6.5 - 7.5 meV. Measured values for \vec{k} perpendicular to these planes, Δ_π , vary from 1.9 - 2.8 meV. These experiments also confirm that both gaps exist out to approximately the same temperature.

In light of this new understanding of MgB_2 , we can reconsider the results of our SIS tunneling experiment. While our MgB_2 pieces were not single crystal, it is possible that in general the B atom planes lay parallel to the flat surface of the base piece. The junctions formed by the initial contact of the tip with the base may have produced a flow of electrons with \vec{k} approximately perpendicular to the B atom planes. Under these assumptions, in our experiment we observed tunneling only between the π bands, explaining our observation of a single gap of approximately 2 meV. This does not, however, explain the observed reduced critical temperature of 29 K.

There remains a lot of excitement for using MgB_2 for practical devices. Work continues to improve thin-film techniques [50, 51]. In addition, there is growing excitement for MgB_2 wires and tapes for transmission cables or magnets. Selective doping of the material has yielded films with large critical current densities and increasing critical fields [52].

Part III

SQUID-based

Magnetocardiography for the

Detection of Heart Disease

Chapter 11

Introduction

11.1 Biological and medical applications of SQUIDS

Since the invention of the superconducting quantum interference device (SQUID), researchers have been interested in using SQUIDS to measure the minute magnetic fields produced by electrical currents flowing in the body. These currents perform important biological functions for the brain and nervous system, the heart, the muscles, and the eyes. The magnetic fields produced by the body are extremely small and in many cases are only detectable using SQUIDS. For example, the largest magnetic field signals measured outside of the body produced by the heart are on the order of 50 pT. The magnetic fields measured outside the head produced by the brain range from 10 fT to 1 pT. These magnetic field strengths are many orders of magnitude smaller than the Earth's magnetic field of about 50 μ T. These signals are also smaller than environmental magnetic field noise produced by moving metallic objects and power lines. Environmental noise in urban environments have been reported to range from 100 pT/Hz^{1/2} to 10 nT/Hz^{1/2} at 1 Hz [53]. Therefore,

to measure biological magnetic fields it is also necessary to use some combination of magnetic shielding, gradiometric cancellation of distant noise sources, active cancellation of measured noise, and signal averaging.

These techniques have steadily advanced over the past couple of decades, and there are now many SQUID-based systems worldwide that measure the magnetic field from the body. Magnetoencephalography, the measurement of magnetic fields from the brain, has become a well-known technique in neuroscience research as well as a useful tool in the diagnosis of brain disorders such as epilepsy. Although technically easier, the field of magnetocardiography (MCG), the measurement of magnetic fields from the heart, has progressed more slowly due to competition with the many other techniques available to study the heart. The recent development of MCG systems designed to work in magnetically unshielded environments has increased the potential for MCG in medical practice and generated a renewed interest in studying the clinical value of the magnetic fields from the heart.

11.2 Bioelectromagnetism and the heart

In the heart, electrical currents perform the important function of stimulating the muscle and causing the heart to beat. Figure 11.1 diagrams the major structures of the heart including its chambers: the left and right atria and the left and right ventricles. In the resting phase, the cardiac muscle cells are polarized; the inside of the cell is at a negative electric potential with respect to the outside of the cell. When the cell is stimulated with an excitation current, the cell membrane ion permeability changes leading to

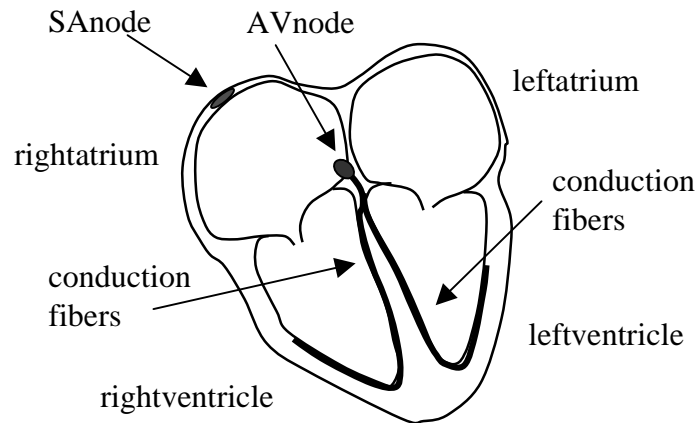


Figure 11.1: Diagram of the heart

an increase in the flow of various ions in and out of the cell. The net result is the increase in the intracellular potential, or the depolarization of the cell. In order for the heart muscle to contract, entire sections of the heart must depolarize synchronously. The initial excitation signal originates at the sinoatrial (SA) node and then propagates throughout the atrial muscle tissue to the atrioventricular (AV) node. Sometime after atrial depolarization, the atrial muscle fibers contract. The ventricular muscle tissue is electrically isolated from the atrial tissue in the normal heart and is not directly stimulated from the excitation signal in the atria. The AV node delays the excitation signal from the atria and then transmits the signal throughout the ventricular muscle tissue along specialized conduction fibers (Fig. 11.1). The depolarization of the ventricular muscle tissue leads to the contraction of the ventricles.

After depolarization, the cells must return to the resting polarized state in order for the cycle to begin again. This process is called repolarization and occurs concurrently with the mechanical contraction of the muscle. Repolarization occurs in individual cells as

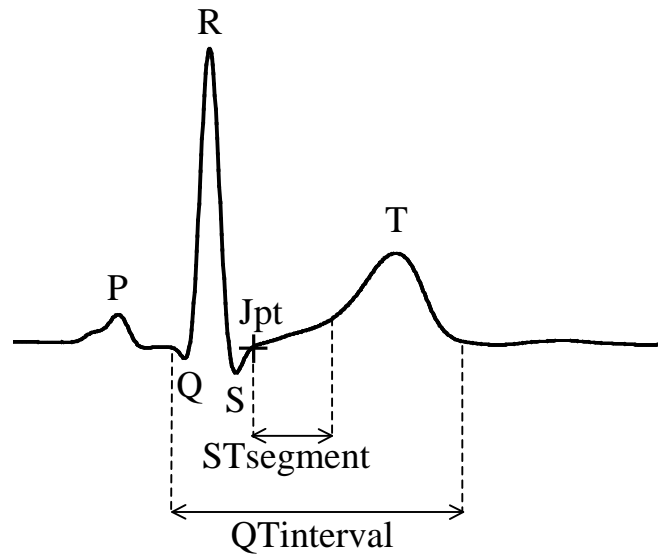


Figure 11.2: Typical electrocardiogram

the action of ion pumps imbedded in the cellular membrane and the evolving membrane ion permeability restore the original intracellular and extracellular ionic concentrations. Repolarization normally occurs systematically in the various regions of the heart. Deviations from the normal large scale repolarization of the heart may indicate disease.

The electrical currents that flow through the heart during the stages of depolarization and repolarization produce very characteristic electric potential patterns on the chest. Electrocardiography (ECG) refers to the measurement of these electric potentials by placing electrodes on the chest. Electrocardiography has been studied for over a century, and the various morphological features in the ECG signal are well documented. Figure 11.2 depicts a sample ECG signal labeled with the conventional names for the different features. The first hump, called the P wave, is produced by atrial depolarization. The series of rapid deflections of alternating sign are the Q, R, and S waves and are produced

by ventricular depolarization. The end of the S wave, labeled the J point, marks the end of the depolarization phase of the heart beat. The next wave, the T wave, is produced by ventricular repolarization. From the J point to the approximate onset of the T wave is the ST segment. The interval from the Q wave onset to the end of the T wave, the QT interval, encompasses the full depolarization and repolarization stages of the ventricles. The repolarization of the atria occurs during ventricular depolarization and produces a small signal which is in general masked by the larger signal from ventricular depolarization. The currents that produce these electrical potentials also produce the magnetic fields measured with MCG. The MCG signal shares many features with the ECG signal, and the naming convention for the waves has been carried over from ECG.

11.3 Comparing magnetocardiography and electrocardiography

Electrocardiography at rest and in conjunction with the application of cardiovascular stress is one of the oldest diagnostic tools in cardiology and remains a mainstay in clinical practice. Although both the MCG signal and the ECG signal stem from a common origin, there are theoretical reasons to believe that the MCG signal may reveal additional information to the ECG. Using volume conductor models for the heart, one can show that azimuthal currents in the heart produce a magnetic field without an accompanying electric field [54]. Researchers have also proposed that current flowing through helical or spiral cardiac muscle tissue would produce magnetic fields without corresponding electric fields [55]. The magnetic field measurement may also be advantageous because it does not

require the use of electrodes physically attached to the body. The MCG signal is thus less affected by contact resistance and noise due to muscle motion. Without electrodes, it is also much easier to measure at a large number of sites. This makes it possible to map the spatial distribution of the signal with little patient preparation time.

Besides the theoretical considerations, there have also been promising studies on human subjects suggesting that MCG reveals complementary information to ECG. In studies comparing MCG and ECG recordings in healthy volunteers undergoing exercise or pharmacological stress, investigators observed changes in the MCG waveform amplitudes during repolarization not seen in the ECG [56, 57, 58]. In comparisons between the MCG and ECG in patients with known cardiac injuries, the MCG was more sensitive than the ECG in detecting abnormalities again during the repolarization stage [59, 60]. These studies suggest that MCG may well provide additional clinical information and identify the need to fully understand the normal MCG.

11.4 Magnetocardiography for the detection of ischemia

Cardiac disorders of various origins can influence the electrophysiology of the heart. Myocardial ischemia refers to the lack of oxygen supply to cardiac muscle cells relative to metabolic demand. It is often caused by the constriction and obstruction of the coronary arteries. Heart disease is the leading cause of death in Americans with ischemic heart disease being the most common form of the disease. The ischemic cells of the heart undergo abnormal depolarization and repolarization. As a result, injury currents flow to and from the ischemic region and neighboring healthy regions of the heart. These injury

currents create changes in the measured ECG and MCG that can be used to diagnose ischemia. Resting and exercise ECG are the most commonly used tests in cardiology to screen patients for possible disease. Depression of the ST segment and the T wave in the ECG signal at rest or during stress are indicators of ischemia (Fig. 11.2). Studies based on tens of thousands of subjects suggest that the sensitivity of exercise ECG to coronary artery disease, the percentage of diseased individuals detected by the exam, is approximately 68% [61]. It is therefore still desirable to develop new non-invasive screening tests for ischemic heart disease.

Several research groups have studied MCG for detecting ischemia with some promising initial results. Studies on patients with documented ischemia but normal resting ECG examinations suggest that MCG can discriminate these patients from healthy subjects [62, 63]. Recently there have been many successful studies investigating the efficacy of MCG in detecting ischemia using large multi-channel systems in a magnetically shielded environment. One study found that the maximum magnetic field component parallel to the chest during repolarization was significantly lower in patients with ischemia than in healthy controls [64, 65]. Other studies have focused on stress-testing using special ergometers made of non-magnetic materials used while the subject is supine. These researchers found that the orientations of the magnetic field contour maps and the amplitudes of the ST segment and T wave immediately after and two minutes after cessation of stress distinguished ischemic patients from healthy volunteers [66, 67, 68].

In this study we tested our ability to acquire MCGs with clinical information using a relatively small multi-channel system in an unshielded clinical environment and

using standard upright treadmill exercise to apply stress. We measured 51 healthy volunteers, both females and males, with a wide range of ages. We examined the MCG from these healthy subjects to determine the normal variation of the MCG and the differences related to age and sex. We also performed a pilot study of ischemic patients. Comparing our patients with the healthy controls, we determined the ischemic signatures in MCG attainable using standard exercise equipment and measuring in an unshielded clinical environment. We also compared various MCG parameters to determine if they were simply correlated and thus contained redundant information. For the MCG analysis, we focused on the repolarization stage of the heart beat, from the J point to the end of the T wave.

Chapter 12

Experimental Methods

12.1 MCG system and measurement

Until recently, multi-channel magnetocardiographs have been used exclusively by researchers in magnetically shielded laboratories. In the past couple of years, there has been growing interest in developing magnetocardiographs for use in unshielded, clinical environments, greatly reducing the cost of operation. In this study, we used one of the first of these instruments, a 9-channel magnetocardiograph, Model 3609, from CardioMag Imaging, Inc. (Schenectady, NY). The system was located first in an unshielded hospital room at Summit Medical Center in Oakland and subsequently at Alta Bates Hospital in Berkeley. To reduce the effect of external magnetic field noise, this system employs second-order, axial gradiometers as its sensors. Figure 12.1 diagrams this sensor. The gradiometer consists of superconducting pickup loops of alternating orientations inductively coupled to the SQUID. This gradiometer is relatively insensitive to uniform magnetic fields as well as to first-order gradients along the axis of the gradiometer. The magnitude of higher order

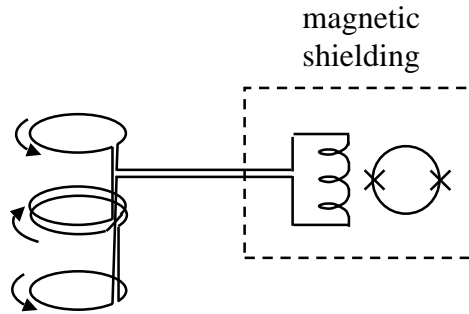


Figure 12.1: Diagram of second-order gradiometer

magnetic field gradients drops off rapidly with distance from the source. A gradiometer, therefore, preferentially detects the biological source which is placed near the pickup coil and suppresses the effect of distant environmental noise sources. In this system, the distance between the lower pickup loop and the outside of the dewar is 14 mm. The distance between pickup loops, the baseline, is 55 mm, and the diameter of the loops is 20 mm. In addition to the 9 gradiometers, the system also includes three SQUIDs oriented in orthogonal directions. These reference SQUIDs, located above the pickup loops of the gradiometers, are used to improve the rejection of uniform magnetic fields. All SQUIDs used in the system are low- T_c niobium SQUIDs with noise levels of $10 \text{ fT/Hz}^{1/2}$ above 10 Hz.

Figure 12.2 is a photograph of the MCG system. The dewar holding the SQUID sensors is supported over a non-magnetic bed by a non-magnetic gantry. The vertical position of the dewar can be adjusted. The bed can move in the horizontal plane along two sets of perpendicular rails. Inside the dewar, the 9 gradiometers are arranged on a 3×3 grid with a 40 mm separation between sensors. During the MCG measurement, the subject lies supine on the bed with the sensors placed in a plane slightly anterior



Figure 12.2: Photograph of the MCG system

to the chest wall. The bed and patient can be accurately positioned in four different locations under the sensor array using guide bars on the bed support for a total of 36 MCG measurement points arranged on a 6 x 6 grid covering a 0.2 m x 0.2 m area. During the MCG measurement, a single ECG trace is simultaneously recorded using 3 electrodes on the limbs. All signals are low pass filtered with a cutoff frequency of 100 Hz and then digitally recorded at 1 kHz.

12.2 Subjects

12.2.1 Normal subjects

After excluding 5 subjects with excessively noisy data and one subject with an abnormal ECG, we examined data from 51 healthy volunteers, 27 males and 24 females. Their ages ranged from 25 to 76 years of age (mean age 48 years, standard deviation 15 years). The volunteers were apparently healthy individuals with no known coronary disease, did not suffer from chest pain or high blood pressure, and were not taking any medications known to affect the ECG. In addition, each subject was given a 12-lead ECG as well as a treadmill test with normal to non-specific results. These standard electrocardiographic tests are described in more detail in Sec. 12.2.3.

12.2.2 Ischemic patients

After excluding 3 subjects for failing to demonstrate physical symptoms or ECG changes indicative of ischemia during the treadmill test and 3 subjects for whom the data were excessively noisy, we examined 11 patients, 7 males and 4 females. The mean age

of the patient group was 76 years and the standard deviation was 7 years. The patient group consisted of individuals with ischemic cardiac disease, including those with known cardiac scars and a history of bypass surgery or other types of cardiac intervention. We administered a 12-lead ECG as well as a standard treadmill test on all patients. Except for one patient, none of the 12-lead ECGs showed changes suggestive of ischemia. Some patients had other cardiac diagnostic exams as part of their medical records. Using all available medical information, we classified the patients based on their likelihood of having ischemic heart disease. The 3 category A patients exhibited typical chest pain or shortness of breath indicative of ischemia as well as typical ECG changes during the treadmill test. The category A patients also had other medical test results within 4 months of this study suggesting ischemia. The 8 category B patients exhibited either typical chest pain or typical ST changes during the treadmill test. A couple of these patients also had recent medical tests suggesting ischemia. All subjects gave informed consent prior to the start of the study.

12.3 Study protocol

Each subject first underwent a standard 12-lead ECG. Six electrodes were placed on the chest and three electrodes were placed on the limbs. Twelve traces were acquired while the subject was resting. The subject was then placed supine on the MCG bed for the rest MCG measurements. The operator positioned the subject with respect to the sensors with use of a laser pointer. As shown in Fig. 12.3, the subject was initially positioned such that the 0.2 m x 0.2 m measurement field was centered 0.14 m inferior to the suprasternal

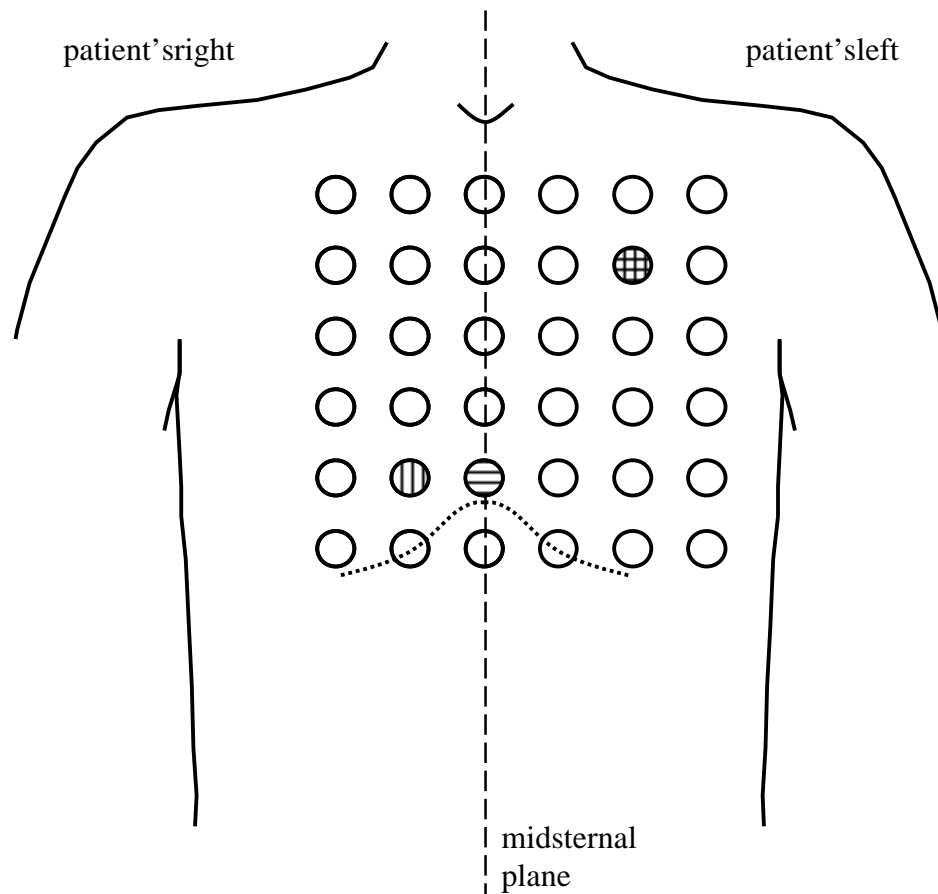


Figure 12.3: Locations of measurement channels in initial positioning of subject relative to the suprasternal notch (at the base of the neck as depicted). Approximate relative position of the rib cage is also marked. Sensors are located on a 6 x 6 grid with 40 mm separation between adjacent points. The checkered sensor corresponds to the channel over the upper left thorax used in MCG waveform parameter calculations. The sensor marked with horizontal stripes was the channel over the lower thorax near the midsternal plane used to calculate the ST amplitude. The channel marked with vertical stripes was the lower thorax position used for all other waveform parameters.

notch and 20 mm to the left of the midsternal plane. For some subjects, it was observed that this measurement field did not optimally cover the measured MCG signals. These subjects shifted position and repeated the resting measurement. The upper left, the upper right, the lower right, and then the lower left positions were measured for 1.5 minutes each for 6 minutes total measurement time.

After the rest measurements were complete, the subject underwent an exercise treadmill test following the standard Bruce protocol. Electrodes were placed on the body in the same positions as for the 12-lead ECG. ECG traces were acquired as the subject walked and ran on the treadmill. The speed and steepness of the treadmill were increased periodically as outlined in the Bruce protocol [69]. Exercise was terminated when the subject's heart rate reached 85% of the maximum age-predicted heart rate defined by medical convention. Using the laser pointer, the subjects were then placed in the same position relative to the sensor array as the rest examination. To reduce the variability of the signal, MCG measurements were not taken immediately post-exercise when the subject's heart rate was rapidly changing. Instead, post-exercise MCG measurements began after the subject's heart rate fell to within 20% of baseline or after 3-4 minutes, whichever came first. Each position was measured for 1 minute for a total recording time of 4 minutes. On average, the healthy volunteer's heart rate slowed by 5 beats per minute (bpm) during the post-exercise MCG measurement compared with a 3 bpm variation at rest. On average, the patient's heart rate slowed by 7 bpm post-exercise as opposed to a 3 bpm variation at rest.

Chapter 13

Data Analysis and Results

13.1 Signal processing

All the signal processing and much of the data display and analysis were performed using LabVIEW programs. Simultaneously acquired MCG and ECG traces were processed together. The traces were digitally filtered with a low-pass finite impulse response (FIR) filter with a cutoff frequency of 25 Hz. A computer algorithm identified the peaks of the R waves in the ECG trace and used these time markers to define synchronized time segments. Noisy time segments were manually removed and then the signals were averaged. A baseline was defined by drawing a line from a manually selected point before the P wave to a point after the T wave and was subtracted from the averaged traces (Fig. 13.1(a)). Average traces that were excessively affected by noise were replaced with interpolated traces when possible. A cubic-spline interpolation was used.

To estimate the effect of environmental magnetic field noise on our data, we regularly obtained noise measurements by acquiring data without a subject under the

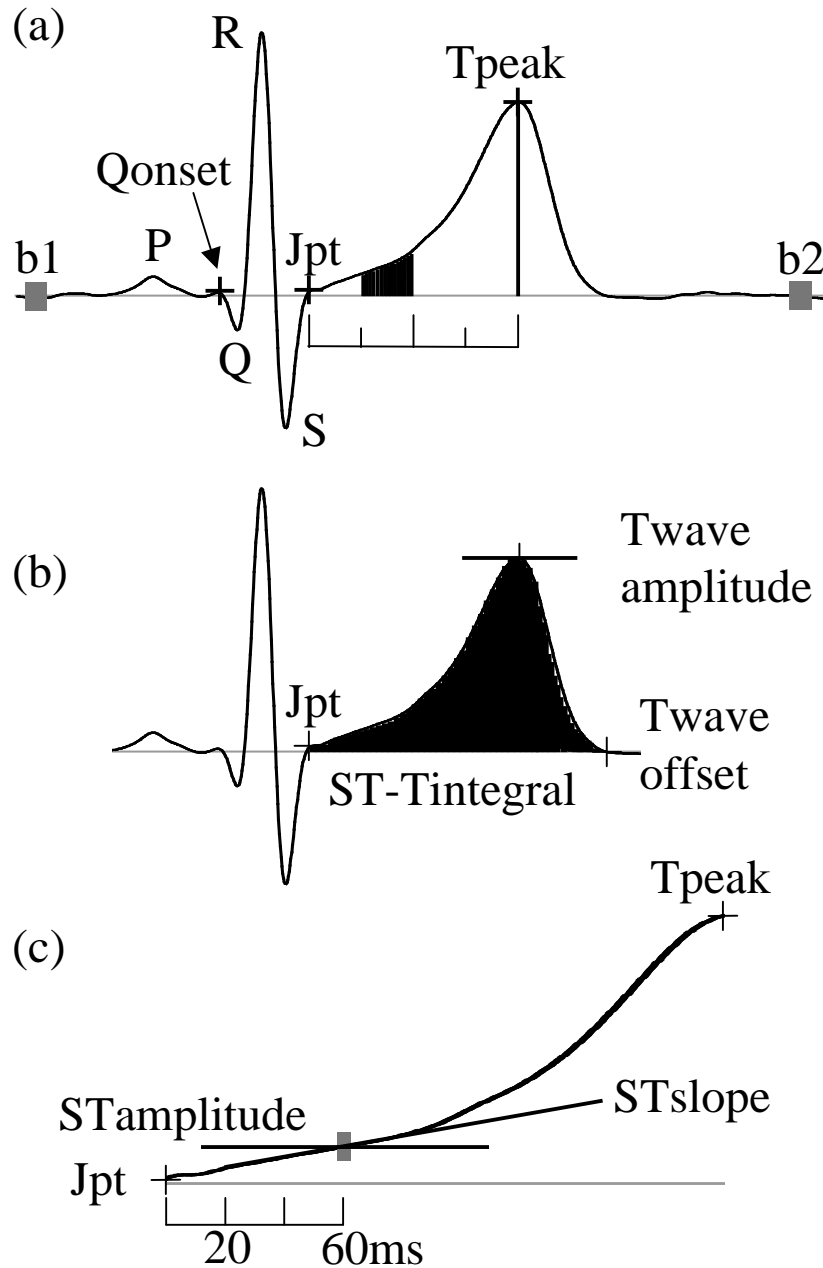


Figure 13.1: (a) Diagram of an averaged MCG time trace. A line drawn between the averages over 20 ms time intervals at b1 and b2 defines the baseline. MCG maps were calculated from the ST segment defined as the second quarter of the interval from the J point to the peak of the T (shaded area) and from the T peak. (b), (c) Definitions of the MCG waveform parameters. (b) T wave amplitude is measured at the peak of the T wave. ST-T integral is the integrated signal from the J point to the T wave offset. (c) The ST amplitude is the average over a 5 ms interval centered 60 ms after the J point. ST slope is the slope of a linear regression line fit to the interval from 20 ms to 60 ms after the J point.

sensors. The magnetic field noise detected by the system could vary from minute to minute depending on the movement of large metallic objects in the hallway or outside the building and on the operation of equipment in neighboring rooms. From the noise measurements, we estimated the power spectra of the environmental noise in our signal. Integrating over the bandwidth, we estimated the average rms noise to be approximately 3 pT. Assuming the MCG measurements were in general averaged over at least 30 beats, the estimated noise level for our averaged MCG traces was approximately 0.5 pT.

13.2 MCG data analysis

We analyzed the averaged MCG data in two different formats. MCG contour maps describe the spatial distribution of the magnetic field component perpendicular to a plane above the chest. Maps can be formed using the signal from a single point in time in the average cardiac cycle or using the MCG signal integrated at each channel over an interval of time. We also examined individual average MCG time traces and waveform morphology parameters derived from them. MCG averaged time traces describe the time-evolving magnetic field component measured at a single location.

13.2.1 MCG contour map parameters

To study the time-evolving spatial distribution of the magnetic fields produced by the heart, we examined animated sequences of MCG contour maps during the repolarization phase of the heart beat. To compare directly the rest and post-exercise measurements from an individual subject, we displayed the two animated sequences next to each other.

The map display rates were scaled to correct approximately for the difference in heart rate. Using this technique to examine the MCG from all subjects, we observed that the MCG spatial patterns often varied substantially early during the repolarization phase. By the peak of the T wave, however, the patterns were very stable in healthy volunteers. The stabilization of the post-exercise MCG repolarization pattern appeared delayed in the patient group (see Fig. 13.2).

To quantify our observations we tracked the progress of the orientation of the MCG maps. The orientation was defined following conventions previously introduced by other researchers [67]. A vector was drawn from the maximum field component (representing magnetic flux directed posteriorly) to the minimum field component (representing magnetic flux directed anteriorly). The orientation of the MCG map was defined as the orientation of this vector as depicted in Figure 13.3. To measure the stabilization rate, we defined a new parameter, the repolarization stabilization interval (RSI). We found it effective to define the stabilization time as the time at which the map orientation reaches within 50° of the orientation at the peak of the T wave. The RSI is measured from the Q wave onset (Fig. 13.1) to the stabilization time. In order to correct for heart rate variation between different individuals and between post-exercise and rest measurements from the same individual, the RSI was corrected by dividing by the square root of the average R-R period measured in seconds. This method of heart rate correction is widely used to correct the QT interval [70, 71]. We calculated the RSI for the rest and post-exercise MCG measurement. We also found the exercise-induced change, the difference in the post-exercise and rest values in each subject.

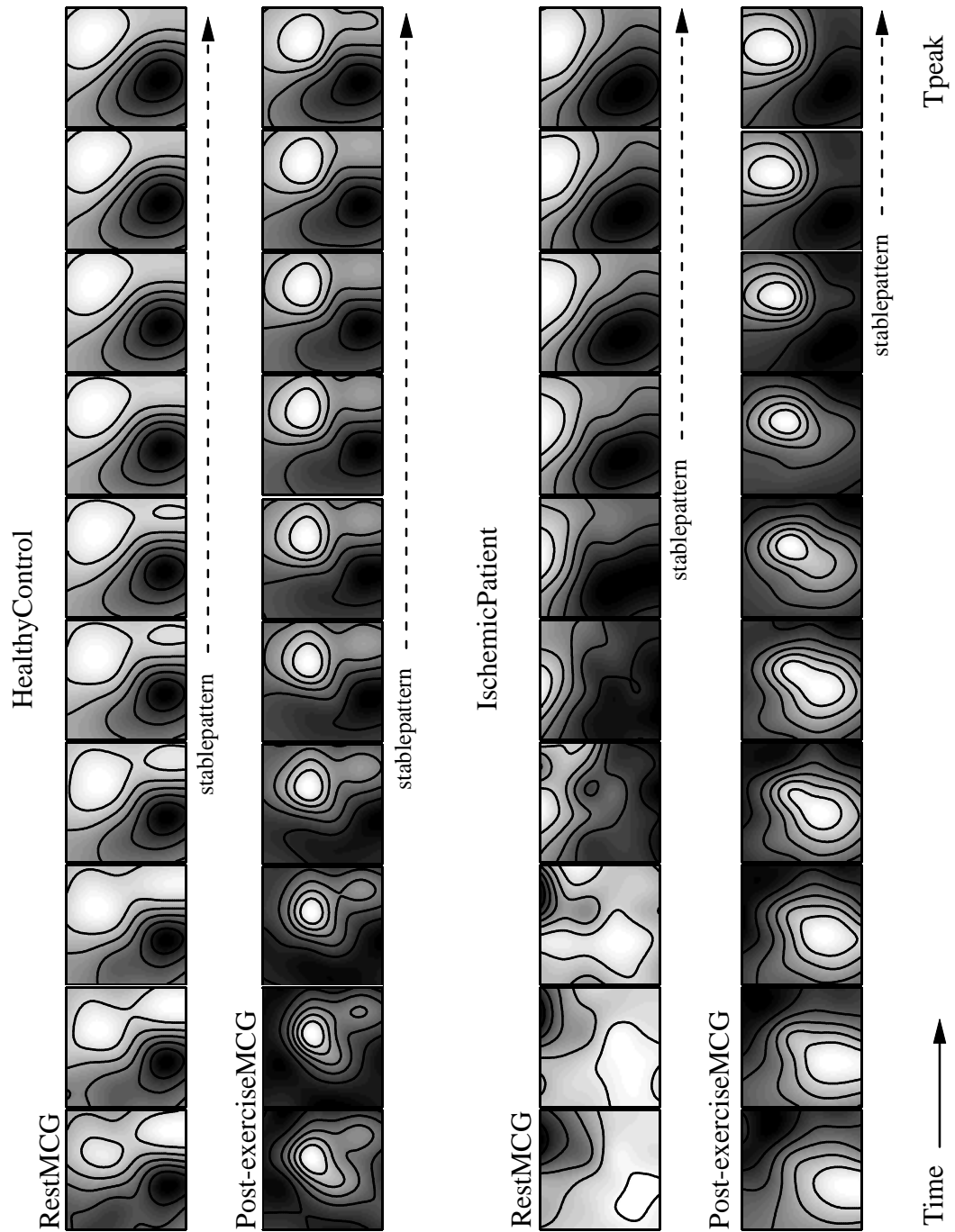


Figure 13.2: Magnetic field contour maps from a healthy control and an ischemic patient during repolarization. The rest and post-exercise contour maps from the healthy control both stabilize early during repolarization. The rest contour map from the patient stabilizes a bit later during repolarization. The post-exercise contour map from the patient stabilizes significantly later during repolarization.

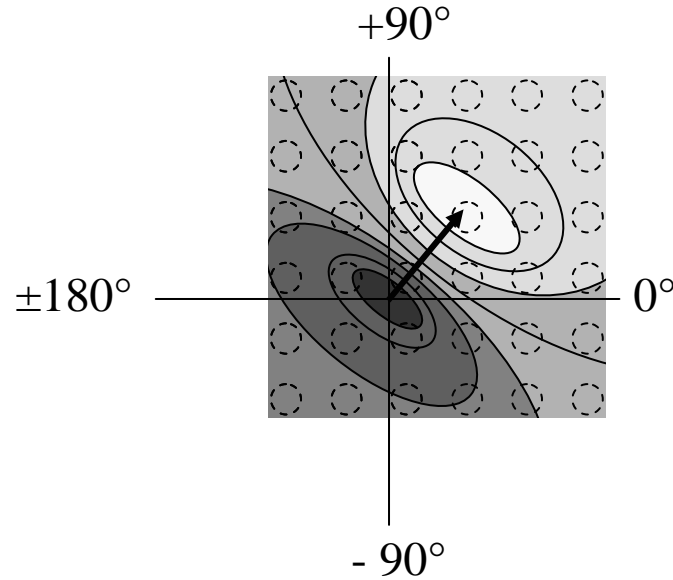


Figure 13.3: Definition of MCG map orientations. Vector was drawn from maximum field component (corresponding to flux directed posteriorly) to minimum field component. The angle of the vector was measured counterclockwise from the subject's right-left line. (Ref. [67])

For comparison we also examined static MCG map orientations that have previously been studied. We calculated MCG map orientations during the ST segment and at the peak of the T wave measured post-exercise. For the data analysis, the ST segment was defined as the second quarter of the interval from the J point to the peak of the T wave as depicted in Fig. 13.1(a) [66]. For each data record, the J point and the Q wave onset were manually selected and the peak of the T wave was automatically found using an MCG channel with a distinct Q wave and large upright R and T peaks. I marked all manually-selected time points using a standardized MCG waveform display with a time scale of 50 mm/s and amplitude scale of 1.7mm/pT [72].

13.2.2 MCG waveform morphology parameters

In addition to examining MCG map parameters, we calculated the rest and post-exercise values and the exercise-induced change (difference between post-exercise and rest values in the same subject) of several waveform morphology parameters. These parameters are analogous to well-known ECG parameters and have recently been demonstrated to be useful in MCG analysis [66]. These parameters are derived from the averaged MCG time traces such as the traces from a healthy volunteer displayed in Figure 13.4. Several parameters were defined. The ST amplitude was defined as the value of the MCG signal averaged over a 5 ms interval centered about 60 ms after the J point. The ST slope is the slope of a linear regression line fit to the interval from 20 ms to 60 ms after the J point. The T wave amplitude is the value of the signal at the peak of the T wave. The ST-T integral is the integrated signal (positive area minus negative area) from the J point to the T wave offset. These parameters are depicted in Fig. 13.1 (b) and (c).

Each morphology parameter was evaluated in two different MCG channels from the sensor array positioned above the anterior chest wall: a channel located approximately over the lower thorax near the midsternal plane and a channel located over the upper left thorax (Fig. 12.3). In general the MCG traces in the channels over the lower thorax near the midsternal plane have upright R and T waves while the signal in the channels over the upper left thorax have inverted R and T waves (Fig. 13.4). The Q wave onset, J point, and T wave offset were manually selected for each channel using the standardized display. The T peak was found automatically. For channels with indistinguishable T waves, we used nearby channels to define the T peak and T wave offset.

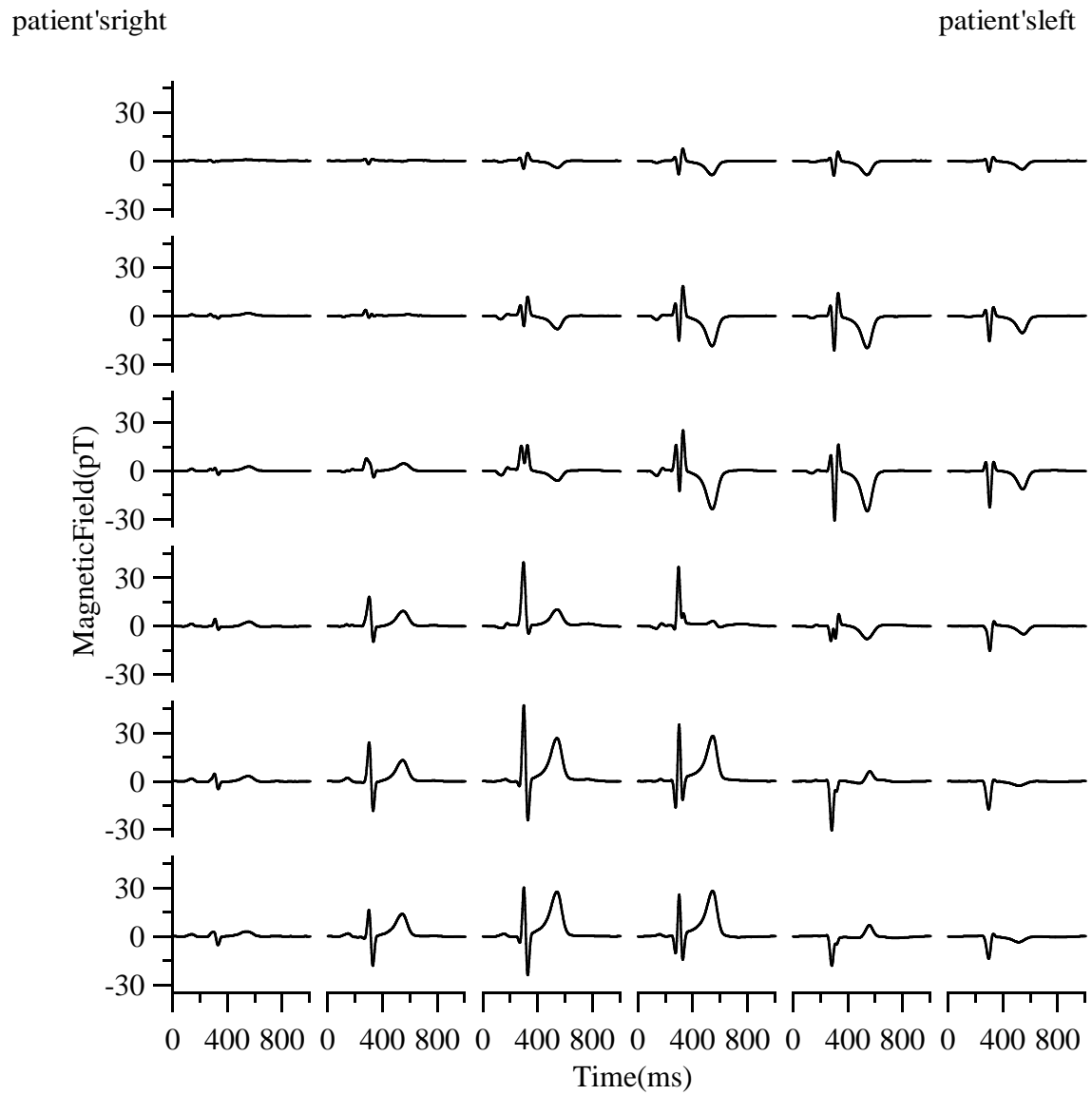


Figure 13.4: Averaged MCG time traces from a healthy volunteer

13.3 Results

13.3.1 Variation of MCG in healthy subjects

To compare different subsets of the healthy volunteers, we calculated the mean and the standard deviation for all the MCG parameters. To test the statistical significance of differences in the means we used the Student's t test for two independent samples with unequal variances (Satterthwaite's method) [73]. The test statistic is given by the expression

$$t = \frac{\bar{x}_1 - \bar{x}_2}{\sqrt{\frac{s_1^2}{n_1} + \frac{s_2^2}{n_2}}} \quad (13.1)$$

where \bar{x}_1 and \bar{x}_2 are the respective means, n_1 and n_2 are the respective sample sizes, and s_1^2 and s_2^2 are the respective sample variances. This test statistic is compared with the t distribution with d degrees of freedom given by

$$d = \frac{(s_1^2/n_1 + s_2^2/n_2)^2}{\frac{(s_1^2/n_1)^2}{n_1-1} + \frac{(s_2^2/n_2)^2}{n_2-1}} \quad \text{rounded down to the nearest integer.} \quad (13.2)$$

The p value for this test can be thought of as the probability of obtaining the observed differences in the two sample means assuming that the two samples are in fact drawn from two populations with the same mean. Table 13.1 compares males with females for all parameters. We found that the post-exercise repolarization stabilization interval in females was longer than in males. The ST orientation was also somewhat different in males and females. The rest and post-exercise values of the waveform morphology parameters were different in males and females, but the exercise-induced changes in the parameters were not. In the MCG channels located over the lower thorax near the midsternal plane, the amplitudes, slopes, and integral values were lower for females than for males. In the MCG

	Males	Females	<i>p</i> Values
MCG map parameters			
Repolarization stabilization interval (ms)			
Rest	161±53	177±55	NS
Post-exercise	174±46	204±58	0.05
Change	13±45	27±49	NS
ST orientation, post-exercise (deg)	86±49	-100±110	0.02
T peak orientation, post-exercise (deg)	56±8	56±9	NS
MCG waveform parameters			
ST amplitude, LowM channel (pT)			
Rest	1.7±1.3	0.5±0.7	<0.001
Post-exercise	1.2±1.4	0.2±0.8	<0.005
Change	-0.6±0.9	-0.4±0.5	NS
ST amplitude, UpL channel (pT)			
Rest	-0.8±0.8	-0.2±0.6	<0.01
Post-exercise	-0.6±0.9	0.0±0.6	<0.005
Change	0.2±0.6	0.3±0.5	NS
ST slope, LowM channel (pT/s)			
Rest	14±8	7±6	<0.001
Post-exercise	13±8	6±5	<0.001
Change	-0.4±5.8	-1.1±6.9	NS
ST slope, UpL channel (pT/s)			
Rest	-11±8	-5±4	<0.001
Post-exercise	-15±15	-4±9	<0.005
Change	-3.6±12.8	1.0±8.5	NS
T wave amplitude, LowM channel (pT)			
Rest	8±5	5±2	<0.005
Post-exercise	9±5	5±2	<0.005
Change	0.3±1.8	0.5±1.0	NS
T wave amplitude, UpL channel (pT)			
Rest	-7±4	-4±3	<0.01
Post-exercise	-8±5	-5±3	0.01
Change	-0.4±2.1	-0.5±1.0	NS
ST-T integral, LowM channel (fT s)			
Rest	1020±620	550±330	<0.005
Post-exercise	860±510	520±320	<0.01
Change	-160±260	-30±120	0.03
ST-T integral, UpL channel (fT s)			
Rest	-870±510	-490±360	<0.005
Post-exercise	-780±550	-450±310	0.01
Change	80±300	40±160	NS

Table 13.1: Comparison of male and female healthy volunteers. Mean±standard deviation reported. The *p* values were calculated from the Student's *t* test for two independent samples with unequal variances. LowM channel is located over the lower thorax near the midsternal plane. UpL channel is over the upper left thorax. NS = not significant.

channel located over the upper left thorax, the values were greater for females.

To uncover differences in the normal MCG due to age, we created a younger and an older subset of healthy volunteers using an age cutoff to define the two groups. Rather than designate an arbitrary age, we varied the age cutoff. For each age cutoff, we calculated the difference in the means of the older and younger groups as well as the p value using the Student's t test described above. Tables 13.2 and 13.3 report the optimal age cutoff corresponding to the minimum p value calculated as well as the corresponding mean values and standard deviations for the older and younger groups. Any p value less than 0.01 was considered significant and corresponding age cutoffs are marked in Tables 13.2 and 13.3. Because of the differences found between healthy males and females, we performed this analysis on the two groups separately. In general, the rest and post-exercise repolarization stabilization intervals were shorter in the younger subjects. The rest and post-exercise values of the waveform morphology parameters in the channels over the lower thorax were greater in the younger subjects. Conversely, the rest and post-exercise values of these parameters in the channels over the upper left thorax were lower in the younger subjects. In general the exercise-induced changes in the parameters were not different in the two groups. Averaging the optimal age cutoff for p values less than 0.01, the mean age cutoff for males was 45 years and the mean age cutoff for females was 43 years.

13.3.2 Differences between ischemic patients and older healthy controls

We created a subset of 33 healthy controls (18 males, 15 females), 44 years of age or older, for comparison with the ischemic patients who were all older than 44 years of age. The mean age of the older healthy controls was 58 years and the standard deviation

	Younger	Older	Age Cutoffs
MCG map parameters			
Repolarization stabilization interval (ms)			
Rest	123±22	177±54	39.5 [†]
Post-exercise	152±35	197±54	50
Change	24±36	-19±54	61
ST orientation, post-exercise (deg)	61±33	95±51	36.5
T peak orientation, post-exercise (deg)	54±7	61±8	59.5
MCG waveform parameters			
ST amplitude, LowM channel (pT)			
Rest	2.9±1.2	1.3±1.1	36.5
Post-exercise	2.2±1.9	0.8±1.1	36.5
Change	-0.8±1.2	-0.4±0.7	43
ST amplitude, UpL channel (pT)			
Rest	-1.6±0.6	-0.4±0.5	39.5 [‡]
Post-exercise	-1.0±1.0	-0.1±0.5	51 [†]
Change	0.1±0.7	0.3±0.5	56.5
ST slope, LowM channel (pT/s)			
Rest	17±8	12±7	43
Post-exercise	16±7	10±6	51
Change	1.7±4.8	-4.6±5.6	56.5
ST slope, UpL channel (pT/s)			
Rest	-15±8	-5±5	54 [‡]
Post-exercise	-21±16	-7±8	51 [*]
Change	-0.5±8.1	-4.7±14.1	36.5
T wave amplitude, LowM channel (pT)			
Rest	11±5	7±4	43
Post-exercise	12±5	7±4	43
Change	0.7±2.0	-0.7±0.9	59.5
T wave amplitude, UpL channel (pT)			
Rest	-11±4	-5±2	43 [†]
Post-exercise	-12±5	-5±2	43 [†]
Change	-0.7±2.2	0.3±1.8	59.5
ST-T integral, LowM channel (fT s)			
Rest	1330±590	860±580	43
Post-exercise	1170±520	700±430	43
Change	-110±280	-270±180	59.5
ST-T integral, UpL channel (fT s)			
Rest	-1380±430	-610±330	43 [‡]
Post-exercise	-1290±600	-530±290	43 [†]
Change	190±300	40±290	39.5

Table 13.2: Comparison of older and younger subsets of healthy males using the Student's t test for two independent samples. The age cutoff reported in years corresponds to the minimum p value as do the mean±standard deviation listed for younger and older groups. * indicates p value <0.01, [†] indicates p value <0.005, and [‡] indicates p value <0.001. LowM channel is located over the lower thorax near the midsternal plane. UpL channel is over the upper left thorax.

	Younger	Older	Age Cutoffs
MCG map parameters			
Repolarization stabilization interval (ms)			
Rest	124±18	199±50	33 [‡]
Post-exercise	163±44	239±45	48 [‡]
Change	16±47	33±50	40.5
ST orientation, post-exercise (deg)	66±76	-79±88	40.5
T peak orientation, post-exercise (deg)	58±9	52±9	60.5
MCG waveform parameters			
ST amplitude, LowM channel (pT)			
Rest	1.3±0.6	0.2±0.4	34.5 [‡]
Post-exercise	0.7±0.7	-0.4±0.5	49.5 [‡]
Change	-0.2±0.4	-0.5±0.6	49.5
ST amplitude, UpL channel (pT)			
Rest	-0.8±0.6	0.0±0.3	33
Post-exercise	-0.4±0.5	0.3±0.4	40.5 [†]
Change	0.2±0.4	0.5±0.7	60.5
ST slope, LowM channel (pT/s)			
Rest	11±6	5±4	34.5
Post-exercise	11±3	4±5	34.5 [‡]
Change	0.9±4.8	-3.4±8.5	51.5
ST slope, UpL channel (pT/s)			
Rest	-8±4	-3±3	34.5
Post-exercise	-9±7	0±9	40.5
Change	-2.2±3.9	2.9±10.0	40.5
T wave amplitude, LowM channel (pT)			
Rest	6±2	4±2	34.5
Post-exercise	7±2	5±2	34.5
Change	0.5±1.1	0.7±0.8	60.5
T wave amplitude, UpL channel (pT)			
Rest	-6±3	-3±2	46.5
Post-exercise	-7±3	-4±2	46.5 [†]
Change	-0.9±1.1	0.1±0.5	53*
ST-T integral, LowM channel (fT s)			
Rest	790±280	430±280	34.5
Post-exercise	720±310	380±240	46.5
Change	-20±120	-60±120	56.5
ST-T integral, UpL channel (fT s)			
Rest	-710±390	-330±240	46.5
Post-exercise	-690±350	-280±120	46.5*
Change	10±150	120±160	60.5

Table 13.3: Comparison of older and younger subsets of healthy females using the Student's t test for two independent samples. The age cutoff reported in years corresponds to the minimum p value as do the mean±standard deviation listed for younger and older groups. * indicates p value <0.01, † indicates p value <0.005, and ‡ indicates p value <0.001. LowM channel is located over the lower thorax near the midsternal plane. UpL channel is over the upper left thorax.

was 9 years. Due to our small number of patients, we grouped male and females together for this analysis. To estimate the abilities of the MCG parameters to detect ischemia, we calculated the areas under the receiver operating characteristic (ROC) curve [74]. The ROC curve plots the sensitivity and false-positive rate of a diagnostic test as the cutoff value that defines a positive test is varied (see Fig. 13.5). The sensitivity is defined as the number of true-positives (diseased individuals who have tested positive) divided by the total number of diseased individuals tested. A high sensitivity demonstrates the ability of a test to detect disease. The false-positive rate is the number of false positives (healthy individuals who have tested positive) divided by the total number of healthy individuals tested. A low false-positive rate demonstrates the ability of a test to correctly identify healthy people as healthy. A perfect diagnostic test will have an area under the ROC curve of 100%.

Table 13.4 reports the means and standard deviations for the map parameters as well as the areas under the ROC curve. As shown in Table 13.4, the exercise-induced change in the repolarization stabilization interval and the post-exercise value were highly effective in separating patients from healthy controls. The RSI rest and post-exercise values in patients were longer than in healthy controls, and the exercise-induced change was greater in patients than in the healthy controls. On the other hand, the ST and the T peak orientations did not discriminate the patients from the controls.

As Table 13.4 details, several MCG waveform parameters also distinguished patients from healthy controls. In general post-exercise values of the MCG waveform parameters performed better than rest values, with ST slope being the one exception. The

	Controls	Patients	ROC areas
MCG map parameters			
Repolarization stabilization interval (ms)			
Rest	188±54	220±60	69%
Post-exercise	208±51	312±28	99%
Change	19±51	92±47	88%
ST orientation, post-exercise (deg)	104±96	-116±37	76%
T peak orientation, post-exercise (deg)	57±9	21±53	65%
MCG waveform parameters			
ST amplitude, LowM channel (pT)			
Rest	0.8±1.0	-0.3±0.6	81%
Post-exercise	0.4±1.0	-1.0±1.1	85%
Change	-0.4±0.6	-0.7±1.0	57%
ST amplitude, UpL channel (pT)			
Rest	-0.2±0.5	0.4±0.5	78%
Post-exercise	0.0±0.7	0.9±0.5	88%
Change	0.2±0.6	0.5±0.5	66%
ST slope, LowM channel (pT/s)			
Rest	8.9±6.7	3.7±2.5	75%
Post-exercise	7.6±6.9	3.6±5.1	73%
Change	-1.3±6.9	-0.1±3.4	55%
ST slope, UpL channel (pT/s)			
Rest	-5.6±5.2	4.5±11.7	85%
Post-exercise	-6.0±13.8	-0.3±4.5	73%
Change	-0.5±12.1	-4.8±11.1	61%
T wave amplitude, LowM channel (pT)			
Rest	5.6±3.6	3.4±2.2	69%
Post-exercise	5.9±3.2	2.1±2.0	86%
Change	0.2±1.2	-1.3±1.5	81%
T wave amplitude, UpL channel (pT)			
Rest	-4.4±2.3	-1.4±1.6	88%
Post-exercise	-4.6±2.2	-1.2±2.1	91%
Change	-0.2±1.2	0.2±1.8	53%
ST-T integral, LowM channel (fT s)			
Rest	670±510	340±220	71%
Post-exercise	570±390	60±220	91%
Change	-104±185	-285±274	75%
ST-T integral, UpL channel (fT s)			
Rest	-500±320	-130±210	84%
Post-exercise	-430±260	10±190	94%
Change	71±198	139±228	52%

Table 13.4: Comparison of ischemic patients with a subset of older healthy controls. Mean \pm standard deviation reported. ROC area = area under receiver operating characteristic curve. ROC areas $\geq 80\%$ are highlighted in bold face. LowM channel is located over the lower thorax near the midsternal plane. UpL channel is over the upper left thorax.

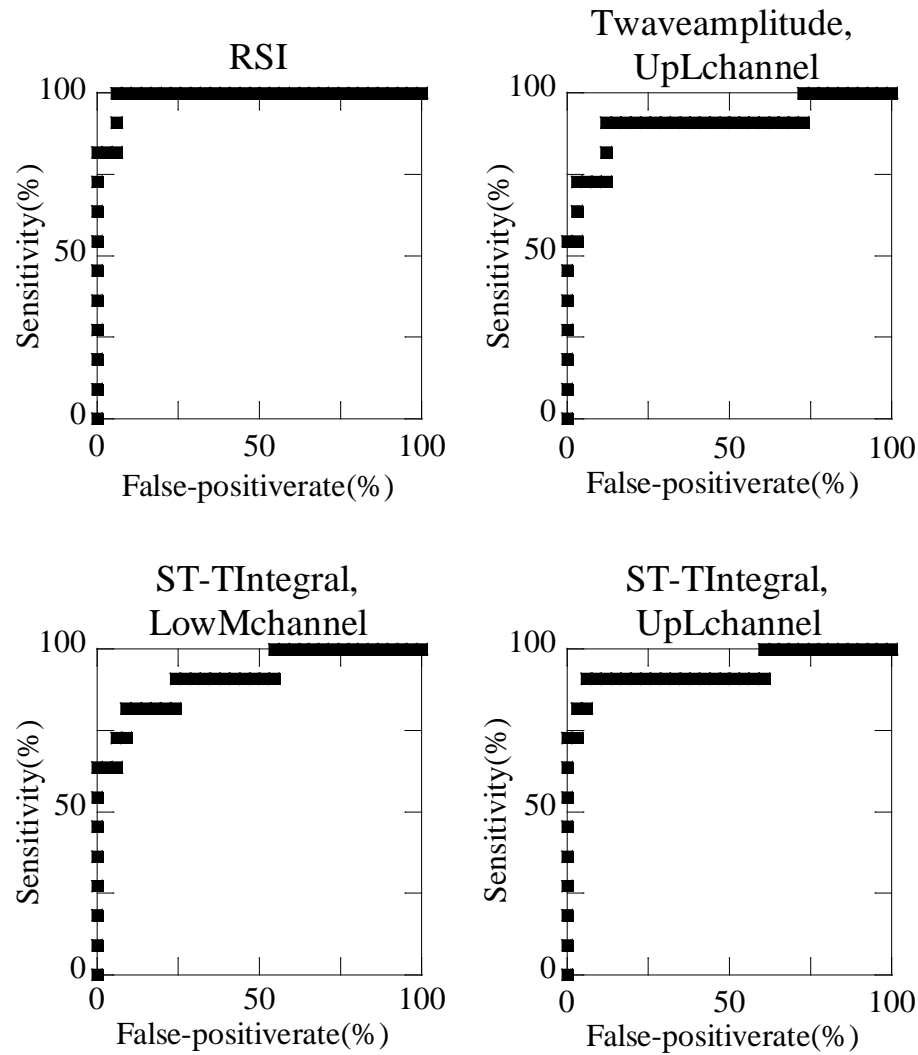


Figure 13.5: ROC curves for the post-exercise repolarization stabilization interval (upper left), T wave amplitude measured in the upper left thorax (upper right), ST-T integral measured in the lower thorax (lower left), and ST-T integral measured in the upper left thorax (lower right). Curves plot the sensitivity (y-axis) and false positive rate (x-axis) as a function of the cutoff parameter used to define a positive test. A perfect diagnostic test would have an area under the curve of 100%.

values of the waveform parameters in the patients were lower in the channel over the lower thorax and greater in the channel over the upper left thorax than those in the healthy controls. For the most part, the exercise-induced changes in the parameters performed worse than both the rest and post-exercise values. For the T wave amplitudes and the ST-T integral in the channel over the lower thorax, the exercise-induced changes in the parameters had ROC areas comparable to the rest and post-exercise values.

Overall, the post-exercise repolarization stabilization interval best separated the ischemic patients from the controls. The post-exercise ST-T integrals and the post-exercise T wave amplitude in the channel over the upper left thorax also performed extremely well. Figure 13.5 graphs the ROC curves for these parameters. Although we used the areas under the ROC curve to compare different MCG parameters, a study with larger numbers of subjects would be needed to determine accurately the sensitivity and the false-positive rate for these parameters.

13.3.3 Comparison of different MCG parameters

In order to explore how various parameters were related, we calculated the correlation coefficients between them using the SAS program. The correlation coefficient is defined as

$$\frac{\sum (x_i - \bar{x})(y_i - \bar{y})}{\sqrt{\sum (x_i - \bar{x})^2 \sum (y_i - \bar{y})^2}} \quad (13.3)$$

where \bar{x} and \bar{y} are the means of the two parameters. Correlation coefficients of ± 1 indicate the existence a simple linear relationship between the two parameters, while a correlation of 0 indicates no relationship. For this analysis, we analyzed the healthy volunteers and

the patient group separately. Table 13.5 reports the correlation coefficients between the MCG map parameters and the MCG waveform parameters, comparing rest values, post-exercise values, and exercise-induced changes in the parameters separately. In general the rest and post-exercise values of the repolarization stabilization interval were somewhat negatively correlated with waveform parameters measured over the lower thorax and somewhat positively correlated with parameters measured over the upper left thorax for both healthy volunteers and patients. The exercise-induced change in the RSI was not well correlated with the change in the waveform parameters for either the healthy volunteers or the patients. The ST orientation was somewhat positively correlated with the waveform parameters in the lower thorax channel and somewhat negatively correlated with the waveform parameters in the upper left channel in the healthy volunteers. In patients, however, there was less correlation between the ST orientation and the waveform parameters. The T peak orientation was uncorrelated with the waveform parameters for both the healthy subjects and the patients.

Table 13.6 reports the correlation coefficients of the waveform parameters in the channel over the lower thorax with their counterparts in the channel over the upper left thorax, again comparing rest values, post-exercise values, and the exercise-induced changes separately. In healthy volunteers, the rest and post-exercise values showed fair to strong negative correlation between the two reciprocal channels. In contrast, the correlations between reciprocal channels in the rest and post-exercise values of the patients were on average substantially lower in magnitude. The correlations between the exercise-induced changes were generally low for both groups.

Correlation of repolarization stabilization interval with concurrent waveform parameters						
	Controls				Patients	
	Rest	Post-exercise	Change	Rest	Post-exercise	Change
ST amp., LowM chan.	-0.54	-0.67	-0.35	-0.49	-0.59	-0.33
ST amp., UpL chan.	0.60	0.58	0.37	0.29	0.34	0.36
ST slope, LowM chan.	-0.37	-0.42	-0.19	-0.64	-0.68	0.01
ST slope, UpL chan.	0.43	0.26	0.06	0.19	0.44	0.18
T wave amp., LowM chan.	-0.32	-0.37	0.02	-0.15	-0.43	-0.17
T wave amp., UpL chan.	0.44	0.46	0.14	0.25	0.07	0.28
ST-T integral, LowM chan.	-0.38	-0.52	-0.14	-0.50	-0.76	-0.39
ST-T integral, UpL chan.	0.52	0.54	0.23	0.35	0.30	0.37
Mean absolute correlation	0.45	0.48	0.19	0.36	0.45	0.26
Correlation of ST orientation, post-exercise with post-exercise waveform parameters						
	Controls				Patients	
ST amp., LowM chan.	0.51			-0.37		
ST amp., UpL chan.	-0.54			0.27		
ST slope, LowM chan.	0.46			-0.01		
ST slope, UpL chan.	-0.47			-0.41		
T wave amp., LowM chan.	0.36			-0.22		
T wave amp., UpL chan.	-0.45			-0.01		
ST-T integral, LowM chan.	0.44			-0.59		
ST-T integral, UpL chan.	-0.49			0.03		
Mean absolute correlation	0.47			0.24		
Correlation of T peak orientation, post-exercise with post-exercise waveform parameters						
	Controls				Patients	
ST amp., LowM chan.	-0.15			-0.16		
ST amp., UpL chan.	0.10			0.29		
ST slope, LowM chan.	0.02			0.11		
ST slope, UpL chan.	-0.08			0.15		
T wave amp., LowM chan.	0.05			0.08		
T wave amp., UpL chan.	0.03			0.58		
ST-T integral, LowM chan.	0.01			0.00		
ST-T integral, UpL chan.	0.06			0.56		
Mean absolute correlation	0.06			0.24		

Table 13.5: Correlation between MCG map and waveform morphology parameters. Rest, post-exercise, and the exercise-induced change compared separately. LowM chan. is located over the lower thorax near the midsternal plane. UpL chan. is over the upper left thorax.

	Controls			Patients		
	Rest	Post-exercise	Change	Rest	Post-exercise	Change
ST amplitude	-0.79	-0.62	-0.04	-0.34	-0.71	-0.03
ST slope	-0.56	-0.68	-0.25	0.17	-0.32	0.34
T wave amplitude	-0.81	-0.83	-0.60	-0.28	-0.40	0.08
ST-T integral	-0.80	-0.82	-0.29	-0.31	-0.13	-0.04
Mean	-0.74	-0.74	-0.30	-0.19	-0.39	0.09

Table 13.6: Correlation between waveform parameters in channels located over the lower and left upper thorax. Rest, post-exercise, and the exercise-induced change compared separately.

Chapter 14

Discussion and Conclusion

14.1 Discussion

Several studies have been performed in laboratory environments that have revealed features in the MCG that correspond well with the presence of ischemia. One goal of this study was to determine if MCG measurements containing clinically important information could be measured using a 9-channel MCG system and standard treadmill exercise equipment in a typical clinical environment. Technically, we successfully obtained MCG measurements 89% of the time. In order to gauge our ability to obtain clinically relevant information we first studied many healthy volunteers to estimate the variability in the normal signal and to understand the dependence on age and sex. We then performed a pilot study comparing several ischemic patients to our control population. Finally, we examined the relationship between different MCG parameters to investigate possible redundancy. In our analysis we examined two classes of parameters, one derived from MCG contour maps and the other derived from the waveform morphology of individual aver-

aged time traces. In the first class, we examined the repolarization stabilization interval, a parameter defined to characterize the spatio-temporal features in the MCG, and the orientations of the MCG maps during the ST segment and at the peak of the T wave. In the second class, we examined the ST amplitude, ST slope, T wave amplitude, and the ST-T integral in two channels: one over the lower thorax near the midsternal plane and one over the upper left thorax.

In general there were large variations in the MCG from healthy subjects. Standard deviations of 1 pT or greater in the ST amplitude or T wave amplitude were observed. This large variation cannot be completely attributed to magnetic field noise in the unshielded environment. By comparing subsets of the healthy volunteers, we found sex and age dependent trends in the MCG parameters. Females exhibited longer repolarization stabilization intervals, lower waveform parameter values in the lower thorax, and greater waveform parameter values in the upper left thorax when compared with males. Subjects younger than 44 years showed the opposite trend when compared with older subjects. Consequently, the distributions of normal MCG parameter values for females lie closer to the distributions for the ischemic patients than their male counterparts, while the distributions for younger subjects lie farther from the distributions of ischemic patients. Therefore, it is possible that the age and sex of a subject should be considered when evaluating the MCG for diagnostic purposes.

By comparing our patient group with a subset of the control population, we found several MCG parameters that distinguished the two groups despite the intragroup variation. The most successful parameter was the repolarization stabilization interval

measured post-exercise. This parameter was able to capture the stress-induced delay in the stabilization of the repolarization MCG pattern in patients that was qualitatively observed when simultaneously viewing animated sequences of the rest and post-exercise MCG maps. Compared with past studies, the ST segment and T peak orientations did not perform well. This may be due to our inability to obtain MCG measurements immediately post-exercise. Additionally, the ST orientation may have been affected by additional environmental noise. We also tested the ability of the MCG waveform parameters to discriminate ischemic patients. In general we were unable to distinguish ischemic patients from healthy controls using the exercise-induced change in these parameters. We were able to discriminate patients using the rest and/or post-exercise values of the waveform morphology parameters as was successfully done in magnetically shielded MCG studies [66]. Because the normal variation in the waveform parameters is quite large, additional environmental noise due to the unshielded environment appears not to have significantly affected the ability of these parameters to discriminate ischemic patients. Of the post-exercise parameters, the ST-T integrals and the T wave amplitude over the upper left thorax were most effective. This finding supports the previously asserted hypothesis that T wave changes due to ischemia persist longer after the cessation of exercise than ST segment changes [66]. At rest, the best parameters were T wave amplitude, ST slope and ST-T integral in the channel over the upper left thorax.

In order to determine whether many of these parameters contain the same clinical information, we examined the correlation coefficient between parameters. The repolarization stabilization intervals at rest and post-exercise were somewhat but not highly

correlated to the waveform parameters. The ST and T peak orientations seemed fairly uncorrelated to waveform parameters. We observed large correlations between the waveform parameters in the channels located over the lower thorax and the upper left thorax in healthy controls, possibly suggesting that the information in the two channels is redundant. However, there were low correlations between the reciprocal waveform channels in the patient group. Not only does this suggest that the two channels contain different information but it suggests that ischemia may introduce asymmetry in the MCG signal.

14.2 Conclusion

In this study, we have demonstrated the ability to acquire magnetocardiograms containing clinical information using a 9-channel system in a unshielded environment and applying stress with the standard treadmill equipment currently in place in cardiac testing centers. As mentioned previously, researchers continue to improve SQUID technology and instrumentation, ensuring that MCG systems will continue to decrease in cost and increase in practicality. However, the research required to solidify our understanding of the clinical information provided by MCG has only just begun. In this study, we measured a relatively large number of healthy volunteers of both sexes from a wide range of ages and found age and sex dependent trends in the normal MCG that suggest that females and younger subjects may need to be evaluated using different criteria than their male or older counterparts. We also introduced a spatio-temporal MCG parameter, the repolarization stabilization interval, which very successfully discriminated patients from healthy volunteers. We confirmed that rest and post-exercise waveform morphology parameters

measured in an unshielded environment, especially those involving the T wave, also distinguish ischemic patients from controls. MCG map parameters appear to have information complementary to waveform morphology parameters. Waveform parameters in reciprocal channels also contain complementary information. As MCG systems for use in unshielded environments become more available, the number of MCG studies should increase, leading to a greater understanding of magnetocardiography and the electrophysiology of the heart.

Chapter 15

Concluding Remarks

In this dissertation, I have described three experiments using Josephson junction devices that demonstrate some of their various uses. The first experiment exploited the macroscopic quantum mechanical properties of a superconducting single electron transistor (sSET). Using this device, we studied the effect of dissipation on the tunneling between charge states of the superconducting island. The sSET was fabricated on top of a GaAs/AlGaAs heterostructure with an imbedded two-dimensional electron gas (2DEG) 110 nm from the top surface. The 2DEG acted as a tunably dissipative ground plane whose sheet resistance could be varied by applying a voltage to a gate on the back of the substrate. The effective charging barrier to tunneling could be varied by applying a voltage directly to the ground plane which also acts as a gate capacitively coupled to the island. We focused our analysis on the minimum zero-bias conductance of the sSET as a function of the gate voltage, or the conductance for the maximum charging barrier. We found that the minimum zero-bias conductance decreased monotonically for increas-

ing temperature and for increasing ground plane resistance. We compared the functional form of the temperature and dissipation dependence of the zero-bias conductance with tunneling rate calculations made to second order in the Josephson perturbation using the Caldeira-Leggett formulation to account for the dissipative environment. We did not find quantitative agreement with these calculations. The presence of quasiparticles may have decreased the effective charging barrier of our sample, accounting for the observed discrepancies.

The second experiment I described used point-contact junctions in magnesium diboride. This material, consisting of alternating planes of B and Mg, was recently discovered to become superconducting at 39 K. By applying light pressure between two pieces of MgB_2 , one tip piece and one base piece, we formed superconductor-insulator-superconductor junctions in which the Josephson supercurrent was quenched by noise. With this tunneling configuration, we observed the tunneling of quasiparticles with momentum vectors approximately perpendicular to the B atom planes in the base piece. We fit the quasiparticle current to BCS theory to estimate the superconducting gap and critical temperature of the material. Our estimated critical temperature of 29 K was suppressed below the bulk critical temperature. Our estimated superconducting gap of 2 meV matched theoretical calculations and experimental observations of the superconducting gap for momentum vectors perpendicular to the atomic planes. We did not observe the second superconducting gap corresponding to momentum vectors parallel to the B atom planes that has also been predicted and experimentally verified. By applying greater pressure between the tip and base pieces, we also formed junctions with superconductor-

normal metal-superconductor characteristics. Using two of these junctions in parallel, we formed superconducting quantum interference devices (SQUIDs). With these devices we performed the first noise measurements from MgB₂ SQUIDs. The lowest noise levels measured were $35 \text{ fT/Hz}^{1/2}$ and $4 \mu\Phi_0/\text{Hz}^{1/2}$ at 1 kHz. These noise levels are comparable to state-of-the-art single-layer high- T_c devices.

The third experiment involved a medical application of SQUIDs, magnetocardiography (MCG), the measurement of the magnetic fields produced by the heart. Recently, commercial multi-channel magnetocardiographs for use in unshielded environments have been developed. We tested the ability of one such instrument installed in an unshielded hospital room to acquire magnetocardiograms with clinical information. We measured 51 healthy volunteers, both females and males, with a wide range of ages. We also performed a pilot study involving 11 patients with ischemic heart disease, the lack of oxygen to the heart muscle relative to demand. We measured the MCG with the subjects at rest and 3-4 minutes after the cessation of treadmill exercise. We analyzed parameters derived from magnetic field contour maps as well as parameters derived from the morphology of the averaged MCG time traces in two different channels: a channel over the lower thorax near the midsternal plane and a channel over the upper left thorax. For many of the parameters, the distribution of values obtained from healthy females was closer to the patients' distribution than the distribution from healthy males. The distribution of parameters from younger healthy subjects was further from the patients' distribution than the distribution from older healthy subjects. Thus, the MCG from females and subjects younger than 45 years may need to be evaluated for ischemia using different criteria. We also defined a pa-

parameter, the repolarization stabilization interval (RSI), which accounts for both the spatial and temporal changes in the MCG. In our pilot study of ischemic patients, we found that the RSI post-exercise was the most effective parameter to distinguish the patients from the healthy controls. We also found that the contour map parameters contained information complementary to the waveform morphology parameters, and the waveform morphology parameters in the two different locations also contained complementary information.

In the future, Josephson junction devices will continue to play an important role both in fundamental physics research and in commercial applications. Currently, many researchers world-wide are developing Josephson junction devices for quantum computing, again making use of their macroscopic quantum mechanical properties. In terms of medical applications, there is an effort to perform a large-scale multi-center clinical trial for SQUID-based MCG using systems operating in unshielded hospital rooms. SQUID-based magnetic resonance imaging is also being developed. As advancements in technology improve the performance and affordability of Josephson junction devices, we can expect to see these devices used in many more inventive ways.

Appendix A

Transport Calculation for the sSET

This appendix contains an example of a transport calculation for the sSET using the Caldeira-Leggett procedure to incorporate dissipation. I will briefly summarize the calculation of the current through the sSET to first order in perturbation theory following more detailed descriptions in several references [75, 76, 31]. First we calculate the transition rate $\Gamma_{LI}(N)$ for one Cooper pair to tunnel from the left lead to an island that initially contains N excess Cooper pairs. To first order, we use the Golden rule,

$$\Gamma_{i \rightarrow f} = \frac{2\pi}{\hbar} |\langle f | H_T | i \rangle|^2 \delta(E_i - E_f) \quad (\text{A.1})$$

where H_T is the term in the Hamiltonian responsible for the tunnelling. Using the Josephson coupling with phase fluctuations in Eq. 2.6 for H_T , the rate for a Cooper pair to tunnel

from the left lead to the island with an associated change in the environment is given by

$$\Gamma_{LI}(N, X \rightarrow X') = \frac{\pi}{2\hbar} E_J^2 \left| \langle X' | e^{i\delta\phi} | X \rangle \right|^2 \delta(\Delta E_{ch} + E_X - E_{X'}) \quad (\text{A.2})$$

where X and X' refer to environmental states and

$$\Delta E_{ch} = E_C [N - C_g V_g / 2e]^2 + V/2 - E_C [(N+1) - C_g V_g / 2e]^2 \quad (\text{A.3})$$

is the difference in the initial and final charging energies of the sSET with bias voltage V .

Since we are not interested in the environment, we can sum over all possible environmental transitions to find

$$\begin{aligned} \Gamma_{LI}(N) &= \frac{\pi}{2\hbar} E_J^2 \sum_{X, X'} p_B(X) \left| \langle X' | e^{i\delta\phi} | X \rangle \right|^2 \delta(\Delta E_{ch} + E_{X'} - E_X) \\ &\equiv \frac{\pi}{2\hbar} E_J^2 P(\Delta E_{ch}) \end{aligned} \quad (\text{A.4})$$

where $p_B(X)$ is the probability of finding the bath in the initial state X and the defined quantity $P(\Delta E_{ch})$ is proportional to the tunneling probability. We can use the identity

$$\delta(\Delta E_{ch} + E_{X'} - E_X) = \frac{1}{2\pi\hbar} \int_{-\infty}^{\infty} dt e^{\frac{i}{\hbar}(\Delta E_{ch} + E_{X'} - E_X)t} \quad (\text{A.5})$$

to rewrite $P(\Delta E_{ch})$ as

$$P(\Delta E_{ch}) = \sum_{X, X'} p_B(X) \left| \langle X' | e^{i\delta\phi} | X \rangle \right|^2 \frac{1}{2\pi\hbar} \int_{-\infty}^{\infty} dt e^{\frac{i}{\hbar}(\Delta E_{ch} + E_{X'} - E_X)t}. \quad (\text{A.6})$$

Switching the order of the summation and the integration and moving into the Heisenberg picture yields

$$P(\Delta E_{ch}) = \frac{1}{2\pi\hbar} \int_{-\infty}^{\infty} dt e^{\frac{i}{\hbar}\Delta E_{ch}t} \sum_{X, X'} \langle X | e^{i\delta\phi(t)} | X' \rangle \langle X' | e^{-i\delta\phi(0)} | X \rangle p_B(X). \quad (\text{A.7})$$

We can now simplify the summation as follows

$$\begin{aligned}
\sum_{X,X'} \langle X | e^{i\delta\phi(t)} | X' \rangle \langle X' | e^{-i\delta\phi(0)} | X \rangle p_B(X) &= \sum_X \langle X | e^{i\delta\phi(t)} e^{-i\delta\phi(0)} | X \rangle p_B(X) \\
&= \langle e^{i\delta\phi(t)} e^{-i\delta\phi(0)} \rangle_{bath} \\
&= e^{\langle [\delta\phi(t) - \delta\phi(0)] \delta\phi(0) \rangle_{bath}} \\
&\equiv e^{K(t)}
\end{aligned} \tag{A.8}$$

where $K(t)$ is the phase correlation function. Phase fluctuations are related to voltage fluctuations via the second Josephson relation, Eq. 1.4. The voltage correlation function is given by the Johnson-Nyquist formula, Eq. 2.8. The phase correlation function is then

$$K(t) = 4 \int_{-\infty}^{\infty} \frac{d\omega}{\omega} \frac{\text{Re}[Z_{eff}(\omega)]}{R_K} \left\{ \coth\left(\frac{\hbar\omega}{2k_B T}\right) [\cos(\omega t) - 1] - i \sin(\omega t) \right\} \tag{A.9}$$

where $R_K = h/e^2 \approx 25.8 \text{ k}\Omega$ is the resistance quantum. Thus the transition rate is proportional to

$$P(\Delta E_{ch}) = \frac{1}{2\pi\hbar} \int_{-\infty}^{\infty} dt e^{K(t) + i\Delta E_{ch}t/\hbar} \tag{A.10}$$

where $K(t)$ is given by the expression above.

The probability of finding the island with N Cooper pairs, $p(N, t)$, is related to the tunneling rates between the island and the two leads. For an appropriate range of gate voltages and bias voltages, the only important charge states to consider are N and $N + 1$ Cooper pairs on the island, and the Cooper pairs tunnel strictly from left to right. In this case,

$$\frac{d}{dt} p(N, t) = -\Gamma_{LI}(N) p(N, t) + \Gamma_{IR}(N + 1) p(N + 1, t) \tag{A.11}$$

where

$$p(N, t) + p(N + 1, t) = 1 \tag{A.12}$$

and $\Gamma_{IR}(N+1)$ is the transition rate for a Cooper pair to tunnel off an island, initially with $N+1$ Cooper pairs, to the right lead. In a steady state solution, $\frac{d}{dt}p(N,t) = 0$ and the current through the sSET is equal to the current through either of the junctions. Using these assumptions we find that the current is

$$\begin{aligned} I = I_L &= -2e\Gamma_{LI}(N)p(N,t) \\ &= -2e\frac{\Gamma_{LI}(N)\Gamma_{IR}(N+1)}{\Gamma_{LI}(N) + \Gamma_{IR}(N+1)} \end{aligned} \quad (\text{A.13})$$

where I_L is the current through the left junction.

Bibliography

- [1] J. Bardeen, L. N. Cooper, and J. R. Schrieffer. Theory of superconductivity. *Phys. Rev.*, 108:1175–1204, 1957.
- [2] B. D. Josephson. Possible new effects in superconductive tunnelling. *Phys. Lett.*, 1:251–253, 1962.
- [3] M. Tinkham. *Introduction to Superconductivity*. McGraw-Hill, San Francisco, second edition, 1996.
- [4] V. Ambegaokar and A. Baratoff. Tunneling between superconductors. *Phys. Rev. Lett.*, 10:486–489, 1963.
- [5] D. Goldhaber-Gordon, H. Shtrikman, D. Mahalu, D. Abusch-Magder, U. Meirav, and M. A. Kastner. Kondo effect in a single-electron transistor. *Nature*, 391:156–159, 1998.
- [6] A. J. Rimberg, T. R. Ho, Ç. Kurdak, J. Clarke, K. L. Campman, and A. C. Gosard. Dissipation-driven superconductor-insulator transition in a two-dimensional Josephson-junction array. *Phys. Rev. Lett.*, 78:2632–2635, 1997.

- [7] J. M. Martinis, M. H. Devoret, and J. Clarke. Experimental tests for the quantum behavior of a macroscopic degree of freedom: The phase difference across a Josephson junction. *Phys. Rev. B*, 35:4682–4698, 1987.
- [8] V. Bouchiat, D. Vion, P. Joyez, D. Esteve, and M. H. Devoret. Quantum coherence with a single Cooper pair. *Phys. Scr.*, T76:165–170, 1998.
- [9] J. R. Friedman, V. Patel, W. Chen, S. K. Tolpygo, and J. E. Lukens. Quantum superposition of distinct macroscopic states. *Nature*, 406:43–46, 2000.
- [10] C. H. van der Wal, A. C. J. ter Haar, F. K. Wilhelm, R. N. Schouten, C. J. P. M. Harmans, T. P. Orlando, S. Lloyd, and J. E. Mooij. Quantum superposition of macroscopic persistent-current states. *Science*, 290:773–777, 2001.
- [11] D. Vion, A. Aassime, A. Cottet, P. Joyez, H. Pothier, C. Urbina, D. Esteve, and M. H. Devoret. Manipulating the quantum state of an electrical circuit. *Science*, 296:886–891, 2002.
- [12] T. Van Duzer and C. W. Turner. *Superconducting Devices and Circuits*. Prentice Hall, New Jersey, 1999.
- [13] J. Clarke. SQUID fundamentals. In H. Weinstock, editor, *SQUID Sensors: Fundamentals, Fabrication and Applications*, volume 329 of *NATO ASI Series*, pages 1–62. Kluwer Academic Publishers, Netherlands, 1996.
- [14] A. O. Caldeira and A. J. Leggett. Influence of dissipation on quantum tunneling in macroscopic systems. *Phys. Rev. Lett.*, 46:211–214, 1981.

- [15] A. O. Caldeira and A. J. Leggett. Quantum tunnelling in a dissipative system. *Ann. Phys.*, 149:374–456, 1983.
- [16] A. N. Cleland, J. M. Martinis, and J. Clarke. Measurement of the effect of moderate dissipation on macroscopic quantum tunnelling. *Phys. Rev. B*, 37:5950–5953, 1988.
- [17] E. Turlot, D. Esteve, C. Urbina, J. M. Martinis, M. H. Devoret, S. Linkwitz, and H. Grabert. Escape oscillations of a Josephson junction switching out of the zero-voltage state. *Phys. Rev. Lett.*, 62:1788–1791, 1989.
- [18] L. S. Kuzmin, Y. V. Nazarov, D. B. Haviland, P. Delsing, and T. Claeson. Coulomb blockade and incoherent tunneling of Cooper pairs in ultrasmall junctions affected by strong quantum fluctuations. *Phys. Rev. Lett.*, 67:1161–1164, 1991.
- [19] J. B. Kycia, J. Chen, R. Therrien, Ç. Kurdak, K. L. Campman, A. C. Gossard, and J. Clarke. Effects of dissipation on a superconducting single electron transistor. *Phys. Rev. Lett.*, 87:017002–1/4, 2001.
- [20] K. K. Likharev. *Dynamics of Josephson Junctions and Circuits*. Gordon and Breach, Philadelphia, 1986.
- [21] M. T. Tuominen, J. M. Hergenrother, T. S. Tighe, and M. Tinkham. Experimental evidence for parity-based $2e$ periodicity in a superconducting single-electron tunneling transistor. *Phys. Rev. Lett.*, 69:1997–2000, 1992.
- [22] T. M. Eiles and J. M. Martinis. Combined Josephson and charging behavior of the supercurrent in the superconducting single-electron transistor. *Phys. Rev. B*, 50:627–630, 1994.

- [23] H. B. Callen and T. A. Welton. Irreversibility and generalized noise. *Phys. Rev.*, 83:34–40, 1951.
- [24] G. J. Dolan. Offset works for lift-off photoprocessing. *Appl. Phys. Lett.*, 31:337–339, 1977.
- [25] L. J. Geerligs, M. Peters, L. E. M. de Groot, A. Verbruggen, and J. E. Mooij. Charging effects and quantum coherence in regular Josephson junction arrays. *Phys. Rev. Lett.*, 63:326–329, 1989.
- [26] L. J. van der Pauw. A method of measuring the resistivity and Hall coefficient on lamellae of arbitrary shape. *Philips Techn. Rdsch.*, 20:220–224, 1958/59.
- [27] D. M. Pozar. *Microwave Engineering*. John Wiley & Sons, Inc., New York, 1998.
- [28] T. R. Ho. *Transport in Arrays of Submicron Josephson Junctions Over a Ground Plane*. PhD thesis, University of California, Berkeley, 1997.
- [29] D. Vion, P. F. Orfila, P. Joyez, D. Esteve, and M. H. Devoret. Miniature electrical filters for single electron devices. *J. Appl. Phys.*, 77:2519–2524, 1995.
- [30] F. K. Wilhelm, G. Schön, and G. T. Zimanyi. Superconducting single-charge transistor in a tunable dissipative environment. *Physica B*, 284-288:1810–1811, 2000.
- [31] F. K. Wilhelm. *Ladungstransport in Supraleitenden Nanostrukturen*. PhD thesis, Institut für Theoretisch Festkörperphysik der Universität Karlsruhe, 1999.
- [32] J. Nagamatsu, N. Nakagawa, T. Muranaka, Y. Zenitani, and J. Akimitsu. Superconductivity at 39 K in magnesium diboride. *Nature*, 410:63–64, 2001.

- [33] G. Rubio-Bollinger, H. Suderow, and S. Vieira. Tunneling spectroscopy in small grains of superconducting MgB_2 . *Phys. Rev. Lett.*, 86:5582–5584, 2001.
- [34] A. Sharoni, I. Felner, and O. Millo. Tunneling spectroscopy and magnetization measurements of the superconducting properties of MgB_2 . *Phys. Rev. B*, 63:220508/1–4, 2001.
- [35] G. Karapetrov, M. Iavarone, W. K. Kwok, G. W. Crabtree, and D. G. Hinks. Scanning tunneling spectroscopy in MgB_2 . *Phys. Rev. Lett.*, 86:4374–4377, 2001.
- [36] A. Kohen and G. Deutscher. Symmetry and temperature dependence of the order parameter in MgB_2 from point contact measurements. *Phys. Rev. B*, 64:060506/1–3, 2001.
- [37] H. Schmidt, J. F. Zasadzinski, K. E. Gray, and D. G. Hinks. Energy gap from tunneling and metallic contacts onto MgB_2 : Possible evidence for a weakened surface layer. *Phys. Rev. B*, 63:220504/1–4, 2001.
- [38] P. Szabó, P. Samuely, J. Kačmarčík, T. Klein, J. Marcus, D. Fruchart, S. Miraglia, C. Marcenat, and A. G. M. Jansen. Evidence for two superconducting energy gaps in MgB_2 by point-contact spectroscopy. *Phys. Rev. Lett.*, 87:137005/1–4, 2001.
- [39] F. Giubileo, D. Roditchev, W. Sacks, R. Lamy, D. X. Thanh, J. Klein, S. Miraglia, D. Fruchart, and J. Marcus. Two-gap state density in MgB_2 : A true bulk property or a proximity effect? *Phys. Rev. Lett.*, 87:177008/1–4, 2001.
- [40] R. S. Gonnelli, A. Calzolari, D. Daghero, G. A. Ummarino, V. A. Stepanov,

- G. Giunchi, S. Ceresara, and G. Ripamonti. Josephson effect in MgB_2 break junctions. *Phys. Rev. Lett.*, 87:097001/1–4, 2001.
- [41] A. Brinkman, D. Veldhuis, D. Mijatovic, G. Rijnders, D. H. A. Blank, H. Hilgenkamp, and H. Rogalla. Superconducting quantum interference device based on MgB_2 nanobridges. *Appl. Phys. Lett.*, 79:2420–2422, 2001.
- [42] Y. Zhang, D. Kinion, J. Chen, J. Clarke, D. G. Hinks, and G. W. Crabtree. MgB_2 tunnel junctions and 19 K low-noise dc superconducting quantum interference devices. *Appl. Phys. Lett.*, 79:3995–3997, 2001.
- [43] R. C. Dynes, V. Narayanamurti, and J. P. Garno. Direct measurement of quasiparticle-lifetime broadening in a strong-coupled superconductor. *Phys. Rev. Lett.*, 41:1509–1512, 1978.
- [44] V. Ambegaokar and B. I. Halperin. Voltage due to thermal noise in the dc Josephson effect. *Phys. Rev. Lett.*, 22:1364–1366, 1969.
- [45] Y. Taur, P. L. Richards, and F. Auracher. Application of the shunted junction model to point-contact Josephson junctions. In K. D. Timmerhaus, W. J. O’Sullivan, and E. F. Hammel, editors, *Low Temperature Physics-LT-13*, volume 3, pages 276–280, New York, 1974. Plenum Press.
- [46] A. I. Braginski, H.-J. Krause, and J. Vrba. SQUID magnetometers. In M. H. Francombe, editor, *Handbook of Thin Film Devices*, volume 3: Superconducting Film Devices, pages 149–225. Academic Press, San Diego, 2000.

- [47] H. J. Choi, M. L. Cohen, and S. G. Louie. Anisotropic Eliashberg theory of MgB_2 : T_c , isotope effects, superconducting energy gaps, quasiparticles, and specific heat. *Physica C*, 385:66–74, 2003.
- [48] M. R. Eskildsen, M. Kugler, G. Levy, S. Tanaka, J. Jun, S. M. Kazakov, J. Karpinski, and Ø. Fischer. Scanning tunneling spectroscopy on single crystal MgB_2 . *Physica C*, 385:169–176, 2003.
- [49] M. Iavarone, G. Karapetrov, A. E. Koshelev, W. K. Kwok, G. W. Crabtree, D. G. Hinks, R. Cook, W. N. Kang, E. M. Choi, H. J. Kim, and S. I. Lee. Directional scanning tunneling spectroscopy in MgB_2 . *Physica C*, 385:215–220, 2003.
- [50] W. N. Kang, H.-J. Kim, E.-M. Choi, C. U. Jung, and S.-I. Lee. MgB_2 superconducting thin films with a transition temperature of 39 Kelvin. *Science*, 292:1521–1523, 2001.
- [51] C. B. Eom, M. K. Lee, J. H. Choi, L. J. Belenky, X. Song, L. D. Cooley, M. T. Naus, S. Patnaik, J. Jiang, M. Rikel, A. Polyanskii, A. Gurevich, X. Y. Cai, S. D. Bu, S. E. Babcock, E. E. Hellstrom, D. C. Larbalestier, N. Rogado, K. A. Regan, M. A. Hayward, T. He, J. S. Slusky, K. Inumaru, M. K. Haas, and R. J. Cava. High critical current density and enhanced irreversibility field in superconducting MgB_2 thin films. *Nature*, 411:558–560, 2001.
- [52] R. Flükiger, H. L. Suo, N. Musolino, C. Beneduce, P. Toulemonde, and P. Lezza. Superconducting properties of MgB_2 tapes and wires. *Physica C*, 385:286–305, 2003.
- [53] J. Vrba. SQUID gradiometers in real environments. In H. Weinstock, editor, *SQUID*

- Sensors: Fundamentals, Fabrication and Applications*, volume 329 of *NATO ASI Series*, pages 117–178. Kluwer Academic Publishers, Netherlands, 1996.
- [54] J. P. Wikswo and J. P. Barach. Possible sources of new information in the magneto-cardiogram. *J. Theor. Biol.*, 95:721–729, 1982.
 - [55] B. J. Roth and J. P. Wikswo. Electrically silent magnetic fields. *Biophys. J.*, 50:739–745, 1986.
 - [56] P. Takala, H. Hänninen, J. Montonen, M. Mäkijärvi, J. Nenonen, L. Oikarinen, K. Simelius, L. Toivonen, and T. Katila. Magnetocardiographic and electrocardiographic exercise mapping in healthy subjects. *Ann. Biomed. Eng.*, 29:501–509, 2001.
 - [57] K. Brockmeier, S. Comani, S. N. Ern , S. Di Luzio, A. Pasquarelli, and G. L. Romani. Magnetocardiography and exercise testing. *J. Electrocardiol.*, 27:137–142, 1994.
 - [58] K. Brockmeier, L. Schmitz, J. de J. B. Chavez, M. Burghoff, H. Koch, R. Zimmermann, and L. Trahms. Magnetocardiography and 32-lead potential mapping. *J. Cardiovasc. Electrophysiol.*, 8:615–626, 1997.
 - [59] Y. Nakaya, M. Nomura, K. Fujino, S. Ishihara, and H. Mori. The T wave abnormality in the magnetocardiogram. *Front. Med. Biol. Eng.*, 1:183–192, 1989.
 - [60] J. Lant, G. Stroink, B. ten Voorde, B. M. Horacek, and T. J. Montague. Complementary nature of electrocardiographic and magnetocardiographic data in patients with ischemic heart disease. *J. Electrocardiol.*, 23:315–322, 1990.
 - [61] R. Gianrossi, R. Detrano, D. Mulvihill, K. Lehmann, P. Dubach, A. Colombo,

- D. McArthur, and V. Froelicher. Exercise-induced ST depression in the diagnosis of coronary artery disease: A meta-analysis. *Circulation*, 80:87–98, 1989.
- [62] P. Cremer, P. Van Leeuwen, B. Hailer, S. Lange, and D. Grönemeyer. Changes in magnetic field maps during repolarization in patients with coronary artery disease. *Med. Biol. Eng. Comput.*, 37:1480–1481, 1999.
- [63] P. Van Leeuwen, B. Hailer, S. Lange, D. Donker, and D. Grönemeyer. Spatial and temporal changes during the QT-interval in the magnetic field of patients with coronary artery disease. *Biomed. Tech. (Berl.)*, 44:139–142, 1999.
- [64] K. Tsukada, T. Miyashita, A. Kandori, T. Mitsui, Y. Terada, M. Sato, J. Shiono, H. Horigome, S. Yamada, and I. Yamaguchi. An iso-integral mapping technique using magnetocardiogram, and its possible use for diagnosis of ischemic heart disease. *Int. J. Cardiac Imaging*, 16:55–66, 2000.
- [65] A. Kandori, H. Kanzaki, K. Miyatake, S. Hashimoto, S. Itoh, N. Tanaka, T. Miyashita, and K. Tsukada. A method for detecting myocardial abnormality by using a total current-vector calculated from ST-segment deviation of a magnetocardiogram signal. *Med. Biol. Eng. Comput.*, 39:21–28, 2001.
- [66] H. Hänninen, P. Takala, P. Korhonen, L. Oikarinen, M. Mäkijärvi, J. Nenonen, T. Katila, and L. Toivonen. Features of ST segment and T-wave in exercise-induced myocardial ischemia evaluated with multichannel magnetocardiography. *Ann. Med.*, 34:120–129, 2002.
- [67] H. Hänninen, P. Takala, M. Mäkijärvi, J. Montonen, P. Korhonen, L. Oikarinen,

- J. Nenonen, T. Katila, and L. Toivonen. Detection of exercise-induced myocardial ischemia by multichannel magnetocardiography in single vessel coronary artery disease. *Ann. Noninvasive Electrocardiol.*, 5:147–157, 2000.
- [68] P. Takala, H. Hänninen, J. Montonen, P. Korhonen, M. Mäkijärvi, J. Nenonen, L. Oikarinen, L. Toivonen, and T. Katila. Heart rate adjustment of magnetic field map rotation in detection of myocardial ischemia in exercise magnetocardiography. *Basic Res. Cardiol.*, 97:88–96, 2002.
- [69] G. F. Fletcher, G. J. Balady, E. A. Amsterdam, B. Chaitman, R. Eckel, J. Fleg, V. F. Froelicher, A. S. Leon, I. L. Pina, R. Rodney, D. A. Simons-Morton, M. A. Williams, and T. Bazzarre. Exercise standards for testing and training: a statement for health-care professionals from the American Heart Association. *Circulation*, 104:1694–1740, 2001.
- [70] A. Staffan. Correction of the QT interval for heart rate: Review of different formulas and the use of Bazett’s formula in myocardial infarction. *Am. Heart J.*, 109:568–574, 1985.
- [71] H. C. Bazett. An analysis of the time-relations of electrocardiograms. *Heart*, 7:353–370, 1920.
- [72] F. E. Smith, P. Langley, L. Trahms, U. Steinhoff, J. P. Bourke, and A. Murray. Errors in repolarization measurement using magnetocardiography. *PACE*, 25:1223–1229, 2002.

- [73] B. Rosner. *Fundamentals of Biostatistics*, chapter 8. PWS-Kent Publishing Co., Boston, third edition, 1990.
- [74] J. F. Jekel, J. G. Elmore, and D. L. Katz. *Epidemiology, Biostatistics, and Preventive Medicine*, chapter 7. W. B. Saunders Company, Philadelphia, 1996.
- [75] G.-L. Ingold and Y. V. Nazarov. Charge tunneling rates in ultrasmall junctions. In H. Grabert and M. H. Devoret, editors, *Single Charge Tunneling*, pages 21–107. Plenum Press, New York, 1992.
- [76] G. Schön. Single-electron tunneling. In T. Dittrich, G.-L. Ingold P. Hänggi, B. Kramer, G. Schön, and W. Zwerger, editors, *Quantum Transport and Dissipation*, pages 149–212. Wiley-VCH, New York, 1998.